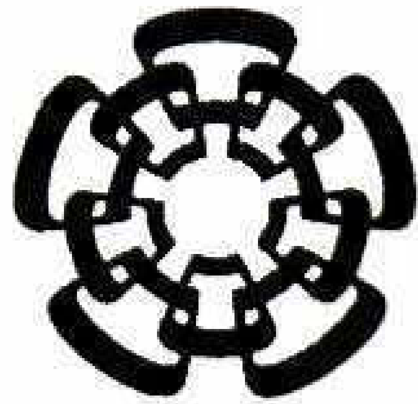

CENTRO DE INVESTIGACIÓN Y DE ESTUDIOS AVANZADOS

DEL INSTITUTO POLITÉCNICO NACIONAL

UNIDAD QUERÉTARO

Thermal stability of the metal/high-k interface for advanced CMOS devices

by

María Isabel Medina Montes

for obtain degree of

Master of Science

CINVESTAV
IPN
ADQUISICION
DE LIBROS

in

CINVESTAV IPN
USB INFORMACION Y DOCUMENTACION
SERVICIO DOCUMENTAL

Materials Science

Thesis Directors:

Dr. Alberto Herrera Gómez

Dr. Francisco Servando Aguirre Tostado

Santiago de Querétaro, Qro. November 2007

CLASIF.: TA404.2 .M43 2007
ADQUIS.: SSI-098
FECHA: 2-VI-2008
PROCED.. DDA-2008
$
I.D. 137884-2001

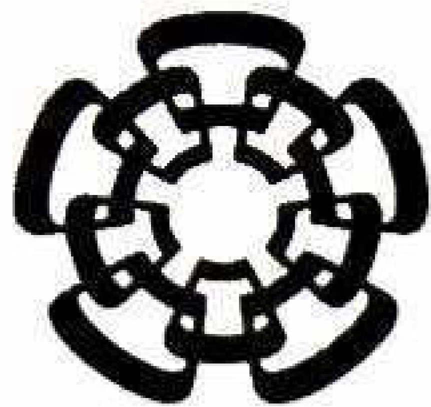

CENTRO DE INVESTIGACIÓN Y DE ESTUDIOS AVANZADOS

DEL INSTITUTO POLITÉCNICO NACIONAL

UNIDAD QUERÉTARO

La estabilidad térmica de interfaces de alta constante dieléctrica para circuitos CMOS avanzados

Tesis que presenta

María Isabel Medina Montes

para obtener el Grado

Maestra en Ciencias

en la especialidad de

Materiales

Directores de tesis:

Dr. Alberto Herrera Gómez

Dr. Francisco Servando Aguirre Tostado

Santiago de Querétaro, Qro. Noviembre 2007

"Hoy estás tan lejos de mí que es inevitable dejar de sentirte tan cerca".

Mi pequeñito, donde quiera que te encuentres, quiero que sepas que te amo, que te ama tu familia y que no hay un solo día que no te pensemos. . .

Dedico este trabajo especialmente a Tí

Chabe

Acknowledgements

Many people contributed in the realization of this project. Their participation was decisive to develop a successful work.

My gratitude to Dr. Robert M. Wallace, because he generously provided me not only the required equipment to develop the thesis project but also considered me as one more of his students. It was an honor to work with him.

Thanks to Dr. Alberto Herrera Gomez. First, of gave me the opportunity to develop my thesis project in collaboration with the University of Texas at Dallas. Second, for his patience throughout the duration of this project, and third, because not only became in my professor, but also in my friend.

Thanks to Servando Aguirre Tostado, because every day he was my technical and scientific support, but mainly thanks to be my friend. He always trusted in my capability to carry out the work and obtain successful results.

My gratitude to CINVESTAV Queretaro to gave me the opportunity to study a posgrade in materials science. For providing distinguished professors who shared some of their knowledge to me, and mainly for accepting the exchange program that established to be all the year corresponding to the thesis development at UTD. Thanks to Dr. Francisco Espinoza Beltrán, Dr. Martin Yáñez Limón and to Dr. Arturo Mendoza Galván for their support and questionable comments concerned to the thesis.

Thank you the entire Materials Science group of The University of Texas at Dallas (UTD), the professors, the students and the clean room staff, of course emphasizing the names of all of those that sharing part of their time and availability to contribute in the development of my project. To Miles Selvidge, to Brian Coss, and to Manuel Quevedo López.

Thanks to CONACyT for its provided support for two years to realize studies of master degree. Also, thanks for the awarded fellowship renewal as an exchange student in the UTD during the last year. It was a great experience!!!

I would like to express my gratitude to Rodolfo Hernandez Guerrero, director of the Center for U.S.-Mexico Studies for his support during my studies in UTD.

And finally, I am grateful to Mari, Dani and Chio for their company and because we built a family in U.S together. I have learned a lot of you.

Table of Contents

List of tables vii
List of figures viii
Resumen xiv
Abstract xv
Chapter 1. Introduction 1
1.1 Metal insulator-semiconductor (MIS) gate stack structures 1
1.2 High-k dielectrics 2
1.2.1 The need of a high-k dielectric 2
1.2.2 Thermodynamic Stability 3
1.2.3 Interface quality 3
1.2.4 Gate electrode compatibility 3
1.2.5 Hafnium based h-*k* dielectrics 4
1.3 Motivation 5
1.4 Objectives 6
1.5 Overview of this Thesis 6
References 7
Chapter 2. X-ray Photoelectron Spectroscopy (XPS) 8
2.1 Basic Principles 8
2.2 Spectrum interpretation 9
2.3 Instrumentation 13
2.3.1 The Sample 13
2.3.2 X-ray Source 13
2.3.3 Detection system 14
2.3.4 Detectors 16
2.4 Quantitative analysis 16
2.4.1 Angle Resolved XPS 17
2.4.2 Ar^+ Sputtering XPS 19
References 19
Chapter 3. Experimental techniques 22
3.1 Wet chemical etching 22
3.2 Thermal treatment (RTA) 25
3.3 ARXPS experiment 27
3.4 Atomic Force Microscopy (AFM) 29
3.4.1 Basic principles 29
3.4.2 AFM experiment 31
3.5 Fourier Transform Infrared Spectroscopy (FTIR) 31
3.5.1 Basic principles 31
3.5.2 FTIR experiment 32
References 33
Chapter 4. Experimental results on the La samples 34
4.1 Samples 34
4.1.1 Samples as received 34

4.1.2 Thermal treatment 34
4.1.3 Sample de-capping 35
4.2 Effect of the chemical etching to MS3 and MS4 samples 37
4.3 XPS data 43
4.3.1 Photoelectron signals detected at different take-off angles 45
4.4 FTIR study 51
References 52
Chapter 5. Analysis and discussion of La_2O_3/HfO_2 structures 53
5.1 Angular dependence of XPS peak areas 53
5.2 Quantitative analysis 54
5.2.1 Parameters employed in the calculations 54
5.2.2 Determination of the thickness of the layers 57
5.2.3 Determination of the stoichiometry of the layers 58
5.3 The lanthanum distribution 59
5.3.1 The La in the RTA sample 59
5.3.2 The La in the unannealed sample 59
5.4 Calculated film structure from the quantitative ARXPS analysis 61
References 62
Chapter 6. XPS on WSix films as metal gate 63
6.1 Samples 63
6.1.1 Samples chemically etched 64
6.1.2 Ar sputtering depth profiling with XPS 65
Chapter 7. Conclusions 69
Future Work 73

List of tables

Table 3.1 Standard Cleaning for Si wafers procedure 23

Table 4.1 Brief description of the growth conditions for samples MS3 and MS4 34

Table 4.2 Recipe for RTA (1000°C/5 sec in N_2) 35

Table 4.3 Gaussian width, Lorentzian width, spin-orbit splitting, branching ratio, binding energy, and background employed in the data fitting with *AAnalyzer* . The parameters shown are those employed for the MS4 sample. 46

Table 5.1 Set of parameters obtained in the characterization of the XPS equipment. A previous carefully characterization of the XPS system was carried out. 55

Table 5.2 The kinetic energies and cross sections of the photoelectrons employed in the calculations were found in the literature. 55

Table 5.3 Effective Attenuation Length values were calculated using the NIST Electron Effective Attenuation Length Database. Lattice constant of the layers and bulk were calculated too. 56

Table 5.4 Core level assimetry parameters employed in the calculation of the effective attenuation lengths with the software provided by NIST. 56

Table 5.5 Layer parameters employed in the calculation of the effective attenuation lengths with the software provided by NIST.[4] 57

List of figures

Figure 1.1 Schematic of a MOSFET device. The MIS gate stack structure is a fundamental constituent for integrating a MOSFET. 1

Figure 1.2 Gate stack for Hf-base MOS devices. The lanthanum layer is added to engineer the work function difference between the metal (TaN) and the semiconductor (Si). 5

Figure 2.1 The radiation of photons (*x*-rays) on the surface of a material causes the photoionization of an atom by the ejection of a core level electron with an kinetic energy E_k. 8

Figure 2.2 Dependence of the intensity detected as a function of the depth. 9

Figure 2.3 Photoelectron spectrum of a TaN/ La-Hf based dielectric/Si stack layer. The peaks represent the electrons that escaped from the material without energy loss and the background belongs to those that suffered energy loss. 10

Figure 2.4 The spectrum of the orbital type s has a band with only one peak (singlet). 11

Figure 2.5 The Hf 4f feature is a doublet composed by two peaks, Hf $4f_{5/2}$ and Hf $4f_{7/2}$. The ratio of intensity is of 3/4 and the splitting of 1.66 eV between them. 11

Figure 2.6 Signal of pure silicon is centered at ≈99.4 eV and silicon oxide at ≈ 103.5 eV. The chemical shift is 4.1 eV. 12

Figure 2.7 Generation of *x*-rays. Electrons are accelerated from a filament towards a target or anode due to the difference of potential between them. The electrons strike on the target generating the emission of x-rays. 14

Figure 2.8 Schematic diagram of an electron detection system. 15

Figure 2.9 Angular dependence of the intensity. The Beer-Lambert equation provides information about the chemical composition as a function of the depth 17

Figure 2.10 The chemical depth profile of the different species in a layer stack on top of a bulk can be modeled employing the ARXPS peaks intensities, the parameters of the layers and the instrument. 18

Figure 2.11 Ar^+ Sputtering XPS as a cyclic process. 19

Figure 3.1 RCA Cleanup hood identifying the principal operating features. 24

Figure 3.2 Jipelec Jetfirst 200 Rapid Thermal Processor used for annealing wafers (RTA). 26

Figure 3.3 Samples deprocessing in the acids hood. 27

Figure 3.4 XPS analytical module from the University of Texas at Dallas. Principal components: analysis chamber, introduction chamber for small samples, hemispheric analyzer, channeltrons and x-ray source showing only the x-ray monochromator 28

Figure 3.5 Small samples are placed on a small sample holder inside the XPS analysis chamber as it shown in the picture. 29

Figure 3.6 Components and subsystems of an AFM system. 30

Figure 3.7 (a) In contact mode AFM the probe directly follows the topography of the surface as it is scanned. (b) In vibrating mode, changes in probes vibrations are monitored to establish the force of the probe onto the surface. 30

Figure 3.8 Instrumental process for obtaining a frequency spectrum with FTIR. 32

Figure 4.1 MS3 and MS4 sample structure as received. 34

Figure 4.2 Annealing profile. The steady state indicates the range time (5 sec) at a constant temperature (1000°C) in N_2 environment. The structured recipe let a high control in the temperature profile during the RTA process. 35

Figure 4.3 Sample structure resulting after the removal etching. 36

Figure 4.4 In the 1μm AFM scans of the MS3 sample it is possible to observe round features that protrudes from a flat surface. The concentration of these features was large enough to become a concern for the ARXPS analysis. The scans were obtained employing 512 lines at 0.488 Hz for the unannealed sample and at 0.458 Hz for the RTA sample. 37

Figure 4.5 The region for the 500nm image was chosen away from the protrusions shown in Figure 6.4. Still, some smaller features stick out from the flat surface. The number of lines employed in the data acquisition was 512 and the rate was 0.392 for the unannealed sample and 0.4209 Hz for the RTA sample. 38

Figure 4.6 The irregular topography revealed by the 200nm images might be the consequence of lower scale protrusions. Lines for the scanned area were 512 and the rates of 0.392 and 0.618 Hz for the unannealed and the annealed samples respectively. The surface morphology shows some roughness even between the protrusions. 39

Figure 4.7 Very high quality and uniformity at the surface of 1μm of size scan for the unannealed and RTA samples were achieved. Some small features stick out from the flat surface can be appreciated (in the order of ≈ 10 nm). Also, is seen clearly the chemical etching affected the same way in both samples. Topography in the unannealed sample is more defined due to the number of lines for scan was of 896 and for the RTA sample was of 512. The rate was of 0.734 and 0.655 Hz for the each one respectively. 40

Figure 4.8 The topography images and therefore, the roughness average are very similar for both samples. Reducing the size scan to 500nm, the uniformity and quality achieved after the etching is conserved. The lines in each scan were the same, 512, and the rate corresponds to 0.734 and 0.655 Hz for the unannealed and annealed samples. 41

Figure 4.9 The smaller AFM scan size done was of 200 nm. The images revealed only few small features stick out from the flat surface, and a very flat surface. The roughness is according with the obtained in the others scans sizes. The lines and the rate for the unannealed sample were of 512 and 0.734, and for the RTA were of 640 and 0.656 Hz respectively. 42

Figure 4.10 XPS survey scans for the MS3 sample with and without RTA. There were not apparent differences in this low resolution mode. 43

Figure 4.11 Survey scans for the MS4 sample with and without RTA. There were not apparent differences in this low resolution mode. 44

Figure 4.12 XPS spectra taken at 45° before and after annealing in-situ (250°C for 15 minutes). a) O 1s signal for MS3 sample; b) C 1s signal for MS3 sample; c) O 1s signal for MS4 sample; d) C 1s signal for MS4 sample. After heating, there was less signal of carbon and a component of oxygen was gone in both cases. 45

Figure 4.13 Fits of the Si 2p and La 4d regions. The binding energies of Si 2p in silicon oxide and La4d photoelectrons overlap. The Si 2p electrons are detected from deeper regions in the film (the peak area increase with the angle is more pronounced). 48

Figure 4.14 La 3d feature of the RTA sample. The spectra were fit according to the literature with four doublets corresponding to on oxidation state (La^{3+}) and another satellites. 48

Figure 4.15 O 1s has two chemical states corresponding to Hf-O-Hf and Si-O-Si bonds. The peak area of oxygen in silicon oxide in the RTA sample is larger than in the unannealed sample. 49

Figure 4.16 Good XPS data is presented for Hf 4f. The fit was done with only one peak centered in the binding energy of hafnium oxide. 49

Figure 4.17 There is evidence of one nitrogen chemical specie only, before and after annealing. 50

Figure 4.18 After the chemical etching of Ta N, a little amount of tantalum remained on the surface in both samples. The tantalum appeared to be oxidized. 50

Figure 4.19 The presence of contamination at the surface of the samples is due to the exposure of samples to air previous to its introduction in the XPS system. 51

Figure 4.20 Fluorine contamination was detected in a very small amount. As discussed below, most of it was located at the surface. 51

Figure 4.21 FTIR spectrum taken for the samples. (a) MS3 and MS4 annealed samples; (b) MS4 annealed and unannealed samples. The Si-O-Si vibration (LO phonon mode) appears at 1220 cm^{-1}. The peak observed close to 900 cm^{-1} is produced by the Si substrate. The feature at 850cm-1 corresponds to O-Hf-O. The treated MS3 sample showed a larger O-Si-O and a lower O-Hf-O signal than the treated MS4 sample. The MS4 sample showed a larger O-Si-O and lower O-Hf-O signal after RTA. 52

Figure 5.1 The signal from La 3d showed a strong dependence on the angle indicating a deep distribution. In contrast, the Ta 4f data showed that this chemical specie was located

at the surface whereas Hf 4f was distributed near of the surface and it was kept there upon RTA. 53

Figure 5.2 The angular dependence of the peak area of anions was closely reproduced (with the exception of O 1s in HfO_2) employing the layered model. The two chemical species of oxygen were attributed to the SiO_2 and the HfO_2 layers. The peak area attributed to SiO_2 showed a larger slope than that in HfO_2. .Also, it can be appreciated in the Figure 7.2, the angular dependence for nitrogen exhibits a similar behavior before and after RTA. The slope lines suggest nitrogen is distributed deep in the film 54

Figure 5.3 Thickness of the films determined by forcing the density of the films to the known bulk values. The comparison between the experimental data and the values obtained from fits employing this structure is shown in Figure 7.1. The question mark in the stoichiometry coefficients of the anions indicates that the amount of oxygen and nitrogen was not employed in the determination of the thickness. 57

Figure 5.4 Resulting stoichiometry for the SiO_2 and HfO_2 layers. The angular dependence of the peak area of anions was closely reproduced forcing the spatial distribution of each oxygen and nitrogen specie to the corresponding layer. The consistency of the compound was preferred over the quality of the fit. However, the experimental data was closely reproduced 58

Figure 5.5 Lanthanum distribution for the RTA MS4 samples. All the lanthanum appeared located at the HfO_2/SiO_2 interface. The error from the ARXPS fits data is around 3% for each take off angle. 59

Figure 5.6 Comparison of Lanthanum distribution between the control sample and the annealed sample. There is a small difference in the slopes. Before RTA almost all the lanthanum was distributed at the HfO_2/SiO_2 interface. After annealing, the rest of La diffused to that interface. 60

Figure 5.7 Lanthanum distribution for the MS4 as received sample. Lanthanum exhibited a deep distribution caused probably by the nitridation process. The most amount of it diffused until the HfO_2/SiO_2 interface and the rest could be located at the surface of the sample or distributed through the HfO_2 layer. The error in the ARXPS data fits was around 3% for each angle. 61

Figure 5.8 Stoichiometry and thickness of the layers in the films. It also shows the amount and distribution of the La and Ta. The growth of the SiO_2 layer, and the decrease of the HfO_2 layer, is consistent with the XPS and IR data. The stoichiometry of each layer was found from the data after correcting for the photoelectron cross section and the attenuation length effects. 61

Figure 6.1 Growth processing of the samples as received from TI (MI20). The chemical reaction between Si and W atoms under annealing treatment origins a WSi_x layer. 63

Figure 6.2 Survey (low resolution) of the detected signals from the MI20 sample at different etching times. The etching was performed with KOH at 80°C for all the samples. 64

Figure 6.3 Regions taken at high resolution (pass energy = 15 eV) for the signals of interest detected from the MI20 sample for different etching times. 65

Figure 6.4 XPS regions of interest for the MI20 sample at different Ar^+ ion sputtering times. The sputtering area was of 4 × $4mm^2$, the sputtering ratio≈ 3Å/min; the beam energy of 5keV with a current of 25 mA; and the range time sputtering from 0sec to 16 min. 66

Figure 6.5 Ar^+ sputtering depth profile showing the most important species detected in the MI20 sample at different Ar^+ ion sputtering XPS times. 67

Resumen

Una función de trabajo apropiada del electrodo metálico es fundamental en el funcionamiento de los dispositivos MOSFET. El Nitruro de tántalo (TaN) y silisuro de tungsteno (WSix) son posibles opciones para ser usados como el metal de compuertas en dispositivos MOS tipo n construidos a base de hafnio. Capas ultra delgadas de lantano son crecidas entre las capas de oxido de hafnio y de TaN con la finalidad de mejorar la alineación de las funciones de trabajo. El primer objetivo de este trabajo fue investigar el perfil estequiométrico de estructuras $TaN/La_2O_3/HfO_2/SiO_2/Si$ (001) crecidas en Texas Instruments que han sufrido procesos de nitridacion (700°C por 10 minutos en NH_3) y Tratamiento Térmico Rápido (RTA, 1000°C por 5 s en N_2). Las muestras fueron caracterizadas con Espectroscopia de Fotoelectrones por Rayos X con Resolución Angular, una técnica extremadamente sensible a la superficie que permite determinar el perfil químico de la superficie. La capa de TaN fue removida químicamente para realizar estudios de XPS, y el efecto del ataque químico fue estudiado con Microscopia de Fuerza Atómica. Los datos de XPS fueron analizados con un método autoconsistente apropiado para modelar el perfil químico de composición. Nuestros resultados mostraron que la mayor parte del lantano estaba colocado en la interfaz HfO_2/SiO_2. El RTA incrementó el espesor en la película de SiO_2 pero el La permaneció distribuido en esa interfaz. Por el contrario, el Ta no se vió afectado por el RTA. La cantidad muy pequeña que no fue removida por el tratamiento químico se mantuvo colocada sobre la superficie de la muestra.

Adicionalmente se estudió el perfil estequiométrico del WSix en muestras de $WSix/HfO_2/Si$. La película de WSix se obtuvo en Texas Instruments depositando una capa de Si sobre otra de W y tratadas térmicamente para obtener WSix. Las muestras fueron caracterizadas con XPS con bombardeo de iones de Ar. Los resultados experimentales mostraron que la gran diferencia de la razón de sputtering entre el Si y el W no permitió la caracterización del perfil estequiométrico con esta técnica.

El trabajo experimental fue realizado en su totalidad en la Erik Jonsson School of Electrical Engineering and Computer Science de The University of Texas at Dallas.

Abstract

The proper effective work function for the metal gate electrode is fundamental to the performance of MOSFET devices. Tantalum nitride (TaN) and Tungsten silicide (WSix) are good candidates as metal gate for hafnium-based gate dielectrics on n-type silicon MOS structures. A lanthanum layers is grown between the hafnium oxide and the TaN to manipulate the effective work function. The first objective of this work was to investigate the chemical depth profile of $TaN/La_2O_3/HfO_2/SiO_2/Si(001)$ stacks, fabricated at Texas Instruments, that had undergone a nitridation process (700°C for 10 min in NH_3) and Rapid Thermal Annealing (RTA, 1000°C for 5 sec in N_2). The samples were characterized with Angled Resolved X-Ray Photoelectron Spectroscopy, an extremely surface sensitive technique for chemical depth profiling. Almost all the TaN metal cap was chemically removed to allow for the ARXPS studies. The effect of the chemical etching was studied with Atomic Force Microscopy. The ARXPS data was analyzed with a self-consistent method suitable for modeling the chemical depth profile. Our results showed that most of the La had diffused through the hafnium layer toward the HfO_2/SiO_2 interface. The RTA increased the SiO_2 layer thickness, but the La remained distributed at that interface. In contrast, Ta was not affected by RTA; a very small amount of Ta that was not removed by the chemical etching appeared on the surface of the sample.

In addition, the chemical composition of WSix through the $WSix/HfO_2/Si$ samples was studied. The WSix was obtained at Texas Instruments by depositing a layer of W on top of a layer of Si on top of the Hf layer. Then the samples were annealed to form the WSix. The samples were analyzed using Ar^+ ion sputtering XPS depth profiling. The data indicated that the large sputtering rate difference between the Si and the W prevented the determination of the depth profile with this technique.

The whole experimental work was performed at the Erik Jonsson School of Electrical Engineering and Computer Science of The University of Texas at Dallas.

Chapter 1. Introduction

Amazing improvements concerning microelectronics technology is leading to reduce the size of the integrated circuits in such way that can be possible to fabricate chips with a high density of components. The transistor as one of these components is scaling to unbelievable dimensions together with improvements in speed and low consumption of power of the devices Also, the necessity to integrate millions of transistors in a same wafer resides on the cost reduction in processing.

1.1 Metal insulator-semiconductor (MIS) gate stack structures

Metal Oxide Semiconductor Field Effect Transistor better known as MOS technology is by far the most common components in integrated circuits (ICs). Its easy fabrication, low cost and scalability result very useful.

The MOSFET device is fabricated using various materials. These materials appear in layers on top of a silicon wafer. The gate dielectric or insulator layer is in directly contact with the wafer surface. The most representative example of insulator film is the silicon oxide (SiO_2). The gate electrode layer has been integrated of polysilicon (PolySi) highly doped on top of the SiO2 film. The integration of these three modules (Metal-Insulator-Semiconductor) in a gate stack structure, constituent an important part of a Field Effect Transistor (see Figure 1.1).

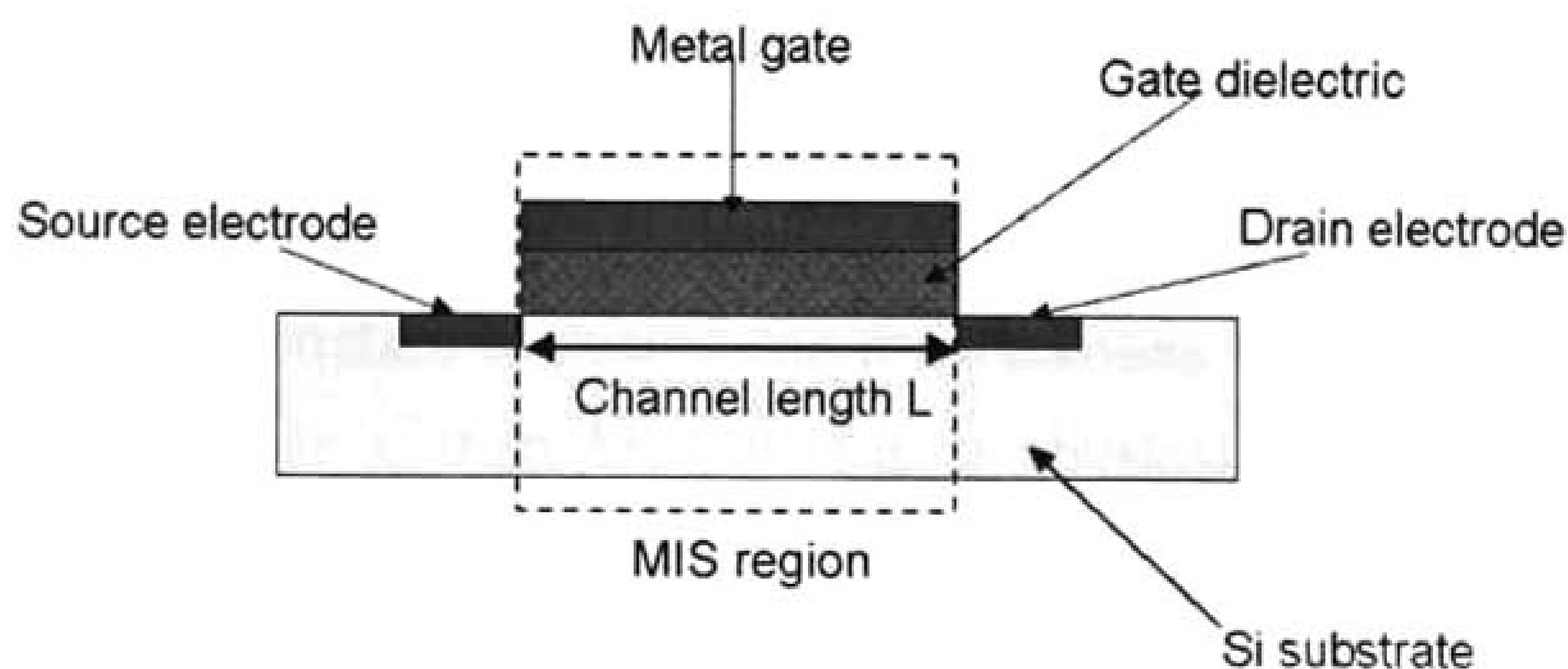

Figure 1.1 Schematic of a MOSFET device. The MIS gate stack structure is a fundamental constituent for integrating a MOSFET.

1.2 High-k dielectrics

1.2.1 The need of a high-k dielectric

Currently, research in high-performance electronic devices goes towards increasing the density of components in integrated circuits by scaling their dimensions. Being the MOSFET the most common component in ICs, its scaling results very important. The scaling of MOSFET devices relies on the reduction of its area (or channel length). Scaling of the channel length in the MOS structures leads to a reduction in the total capacitance unless the thickness of the dielectric is reduced or its dielectric constant is increased (see Figure 1.1).

Silicon oxide has been the exploited dielectric gate during the last four decades. Due to its good electrical properties such as: high resistivity of ~10^{18}Ωcm,[1] a large band gap of ~9 eV and physical properties, high quality $Si/Si0_2$ interface, excellent thermal stability and good interface in contact with silicon substrate.

However, the principal limitation of SiO_2 as a gate dielectric is its low dielectric constant (κ= 3.9).Tunneling currents are the result of thinner gate dielectrics as is the case of SiO_2 film. The best way to understand it is by means of the next analysis:

Consider a parallel plate capacitor, the capacitance is given by

Equation 1.1 $$C = \kappa \frac{\varepsilon_0 A}{d},$$

where κ is the dielectric constant of the material, ε_0 is the permittivity of free space (8 85 X 10^{-12}F/m), A is the area of the capacitor and d the thickness of the dielectric. As was mentioned above, MOSFET size reduction implies the channel length or oxide thickness scaling. In order to the Equation 1.1, a high capacitance is achieved increasing the dielectric constant or decreasing the thickness. There is an advantage to use materials with a higher κ than SiO_2, that is, a physical thickness gate dielectric thicker than SiO_2. The physical thickness of any high-*k* material respect to SiO_2 thickness is described by the expression

Equation 1.2 $$t_{\text{high-k}} = \frac{\kappa_{\text{high-k}}}{\kappa_{SiO_2}} t_{SiO_2}$$

t_{SiO_2} is called equivalent oxide thickness (EOT). So, due to $\kappa_{\text{high-k}}/\kappa_{SiO_2}$ is bigger than 1, the high-*k* physical thickness always will be longer than EOT.

1.2.2 Thermodynamic Stability

For most of the high-k oxides on Si, the formation of an undesirable interfacial SiO_2 is unavoidable. Most of the times this interfacial SiO_2 layer is not-stoichiometric and affects the electrical properties of the MOS device. The thermal stability of the MOS structure is a requirement that any high-k oxide must meet. The thermal processes used to activate dopants in the semiconductor or in the gate electrode (in the case of poly-Si) provoke chemical reactions at the interfaces as well as inter-diffusion from the gate oxide towards Si substrate.

1.2.3 Interface quality

Bulk electronic properties such as channel mobility and leakage current may depend on dielectric/Si interface quality in MOSFET devices. The interface quality is determined by the presence of satisfied chemical bonds. With the SiO_2 layer, the bonds formation between Si-Si and Si-O is successful achieved as consequence of coordination number. Furthermore, is expected that high-*k* with elements having excess or lacking bonds compared to SiO_2, as is the case of metal oxides, promotes the formation of interface defects near of at the channel region. To compensate the non-corresponding in the coordination high- *k*/Si bonds, more than one element might form part of the gate oxide compound. However, the formation of metallic species and silicides phases from the oxide directly in contact with Si results in electrical properties degradation.

1.2.4 Gate electrode compatibility

The choice of a particular gate oxide as one of the principal parts of MOS devices is its compatibility with the gate electrode. Poly-Si highly doped has widely been used as the gate electrode material of choice.

However, further scaling in MOS devices will require new metal gates to deal with some of the following problems. First, as it was mentioned above, scaling will be achieved by thinner gate dielectric films. Second, activation dopant annealing stimulates crystallization or impurities penetration throughout the gate dielectric toward channel

region degrading device performance. Third, depletion effect occurs at the electrode/dielectric interface as result of the dielectric thickness and the doping concentration of Poly-Si.

Currently metal gates are being investigated as replacement for poly-Si gates in CMOS devices for the 45 nm technology node and beyond. The interest in metal gates over poly-Si gates is driven by 1) the ability to scale inversion capacitance down by 0.2 nm to 0.3 nm without affecting gate leakage current by elimination the polysilicon depletion effect, 2) reduction of dopant penetration and device design by relaxing the requirement for gate activation and 3) better compatibility of metal gates with high-*k* dielectrics than poly-Si.[2]

In theory, the transistor threshold voltage is primarily determined by the work function (Wf) of the gate electrode material. The work function values for various metals are known and certain materials are identified with 'band edge' properties, i.e. with Wf close to the valence or the conduction band of silicon.[3] Some materials as Ta, TaN, and TaSiN are possible metal gates candidates for n-MOS devices.[4]

1.2.5 Hafnium based h-*k* dielectrics

Low *k* for SiO_2 led to the search for novel materials to replace it. Silicon oxynitride (SiON) appeared to be an alternative gate dielectric with an increased k (≈ 6) compared to SiO_2, strong resistance to impurity diffusion and compatibility with conventional CMOS processes[1].

Hafnium silicate (HfSiO) reduces the gate leakage while maintaining the device performance with respect to SiON dielectrics. The dielectric constant of $HfSi_xO_y$ is between 8 and 15 depending on the hafnium composition on the film.[5] Also it shows relatively high carrier mobility, however, it tends to trap a high density of electrons. Nitridation is known to suppress the crystallization of hafnium silicates that occurs during thermal treatments.[6] HfSiON is being studied due to its relatively high-k constant and high thermal stability.

Also, the interest of depositing additional ultra thin layers in the hafnium based gate dielectric such as Al-based or La-based inserted between the Hf-based gate dielectric

and the metal gate, are used to control the metal gate work function on Hf-based gate dielectric[2]

In recent reports it was found that for RTA anneals at or above 950 °C, 20 s, in N_2, done in the $Al_2O_3/LaAlO_3$/p-Si(001) stack, is observed La metal diffusion into the Si substrate. Thermal stability of high-k dielectric film in direct contact with the underlying Si substrate is essential because of the out-diffusion of metal impurity atoms into the channel region during processing can cause carrier mobility degradation.[7]

1.3 Motivation

Because for its large work function, TaN is a promising metal for n-MOS devices based on hafnium (see Figure 1.2). However, the alignment of the work function is not completely ideal. Among other players, Texas Instruments was trying to manipulate the work function alignment of the system by adding a layer of lanthanum oxide.

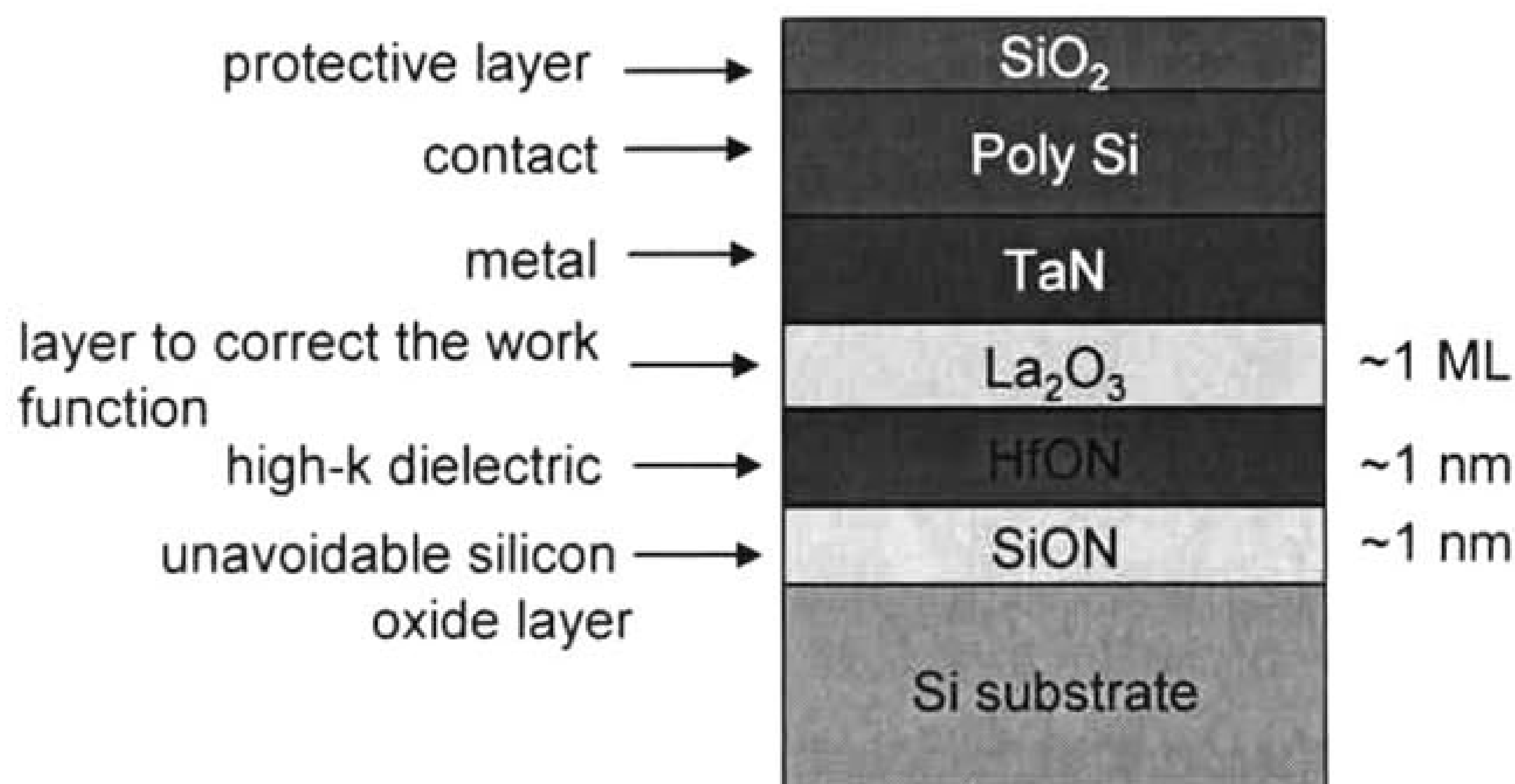

Figure 1.2 Gate stack for Hf-base MOS devices. The lanthanum layer is added to engineer the work function difference between the metal (TaN) and the semiconductor (Si).

The thermal stability of Ta and La atoms in the stack is a concern because their diffusion to the Si interface could affect the channel mobility. In addition, the structure could be disrupted by the thermal treatments that the devices undergo in the production line. The chemical depth profile of this stack was studied with back side SIMS[8] and High Resolution Rutherford Back Scattering.[9] However, none of these studies had the necessary resolution to provide an answer.

The University of Texas at Dallas engaged in a collaboration with TI with the objective to determine the thermal stability of the stacks shown in Figure 1.2. TI provided a series of samples to be characterized at UTD.

1.4 Objectives

The General Objective of this thesis is to determine the chemical depth profile of the TaN/La_2O_3/HfNO/Si stack before and after RTA treatments.

The Specific Objectives were the following:

- To prepare the samples provided by TI for XPS and FTIR characterization. This implied the removal of all the layers on top of La_2O_3 film using wet chemical etching
- To assess the effects of this etching on the surface morphology by AFM studies.
- To assess the structure of the film (thickness and stoichiometry of the layers).
- To determine the distribution of Ta and La throughout the samples and to assess the effect of the thermal treatment on this distribution.

An additional objective was included in this thesis work, consisting on the chemical depth profile of WSi/Hf based devices by Argon Sputtering XPS.

1.5 Overview of this Thesis

The present work was divided in seven chapters. The Chapters 1-3 describe the theory and experimental techniques used in this thesis. Chapter 1 provides an overview concerning the technological applications influenced by this study. Also, it contains a brief explanation of some of the required characteristics and components of the materials under study. The objectives are described in this chapter as well. In Chapter 2 the fundamentals of X-ray Photoelectron Spectroscopy technique are described as well as the topics related to the compositional depth profile determination (ARXPS and Ar^+ ion sputtering XPS). The Chapter 3 is an extension of the Chapter 2, and it is focused on the basic principles of the other experimental techniques employed.

Most of this thesis was focused on the study of the Poly-Si/TaN/La_2O_3/Hf-based dielectrics. They were characterized by ARXPS, AFM and FTIR. These results are

shown in Chapter 4. The Chapter 5 deals with the analysis and discussion of the same samples.

Other samples under study (WSix) are shown in the Chapter 6. Their structure characterization and analysis of results are described in the same chapter.

Finally, the Chapter 7 shows a summary of all the important conclusions in this thesis.

References

[1] M. D. Groner, and S. M. George. High-k dielectrics grown by atomic layer deposition: capacitor and gate applications. Interlayer Dielectrics for Semiconductor Technologies, Chapter 10, pp. 327-348 (2003).

[2] H.N. Alshareef., P. Majhi, S.C Song, M. Quevedo-Lopez, P. Kirsch, , B.H. Lee, , and R. Jammy. Work function Engineering Using Interfacial Layers on Hf-Based Gate Dielectrics. FUTURE FAB International, Issue 21, pp 98-100.

[3] P. Absil, T. Hoffmann, J. Kittl, A. Lawers, A. Veloso, H. Yu, M. Jurczak, and S. Biesemans. Raising the Bar, Trends and Challenges in CMOS FEOL Technology for the 45nm Node and Beyond. Yield Management Solutions, pp. 9-14, (2006).

[4] R. M. Wallace, and G. D. Wilk. High-*k* Dielectric Materials for Microelectronics. Critical Reviews in Solid State and Materials Sciences, Vol 28, pp. 231-285 (2003).

[5] P. Punchaipetch, G. Pant, M. A. Quevedo-Lopez, C. Yao, M. El-Bouanani, M.J. Kim, R.M. Wallace and B.E. Gnade. Low temperature Deposition of Hafnium Silicate Gate Dielectrics. IEEE Journal of Selected Topics in Quantum Electronics, Vol. 10, No. 1, pp. 89-100, (2004).

[6] Influence of Charge Traps within HfSiON Bulk on Positive and Negative Bias Temperature Instability of HfSiON Gate Stacks. Japanese Journal of Applied Physics. 2005.

[7] P. Sivasubramani, M.J. Kim, B.E. Gnade, and R.M. Wallace. Outdiffusion of La and Al from amorphous $LaAlO_3$ in direct contact with Si (001), Applied Physics Letters, Vol 86, No. 201901, pp.1-3 (2005).

[8] IBM VLSI 2006, V. Narayanan et. al.

[9] Data collected at North Carolina State – F. Stevie.

Chapter 2. X-ray Photoelectron Spectroscopy (XPS)

X-ray Photoelectron Spectroscopy is a characterization technique for surfaces widely used in applications such as: semiconductor devices, optical devices, catalysts, polymers and new ceramic materials[1]

XPS as a surface sensitive technique can detect up to few nanometers of depth and not only gives elemental information of the surface but also provides the chemical states of those elements.

2.1 Basic Principles

XPS technique is based in the photoelectron principle in which the surface of a material is excited with photons such as *x*-rays causing the emission of the electrons from a core level (photoelectrons) in the atom. The kinetic energy E_K of the free photoelectrons is related with their binding energy E_B, the energy of the *x*-ray, $h\nu$ and the work function W as follows

Equation 2.1 $E_B = h\nu - E_K - W$

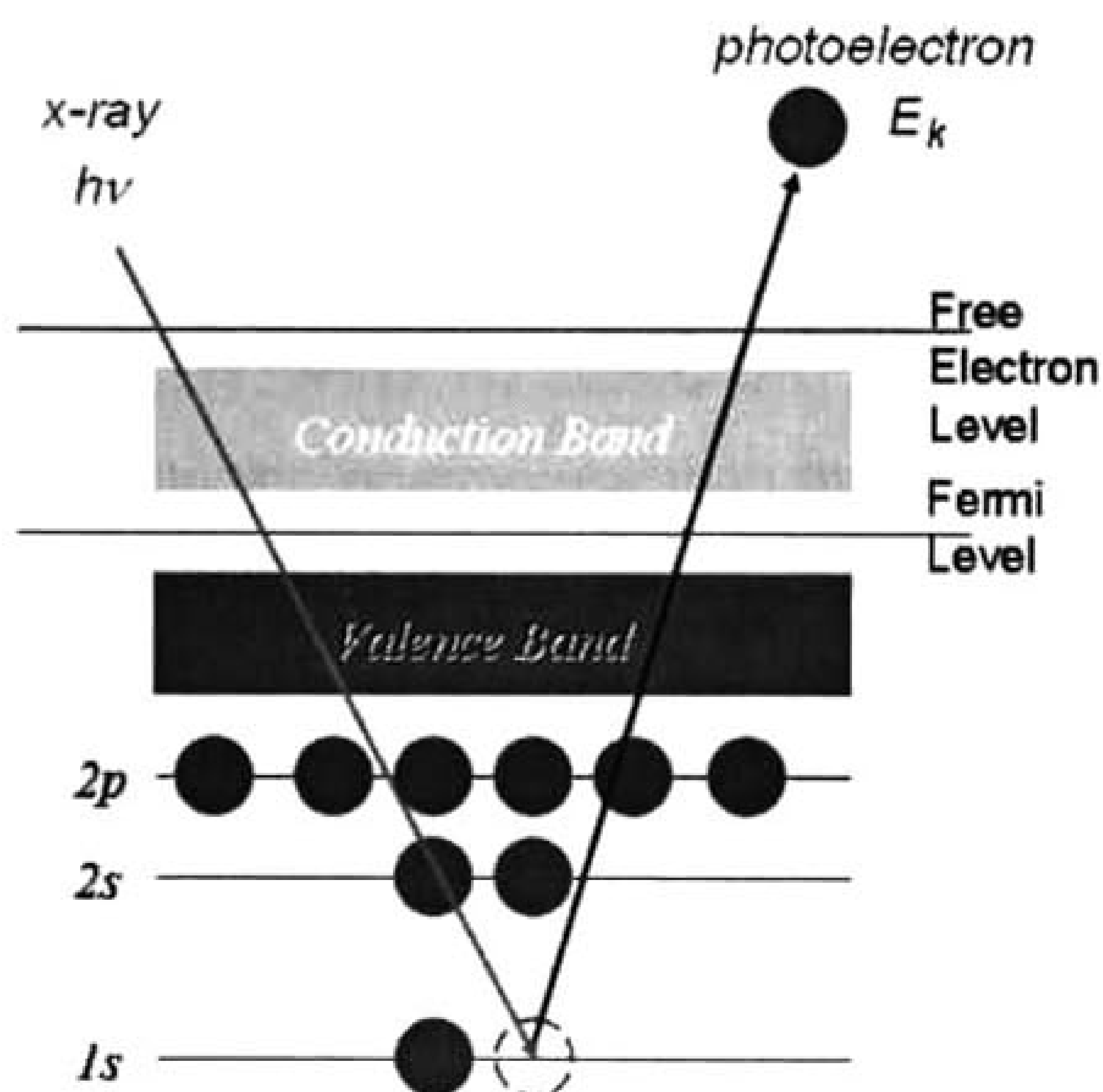

Figure 2.1 The radiation of photons (*x*-rays) on the surface of a material causes the photoionization of an atom by the ejection of a core level electron with an kinetic energy E_K.

A simple way to describe the process is shown in the Figure 2.1. The photon energy of the x-ray is sufficient to extract an electron from inner levels (1s, 2s, 2p) of the atom to the vacuum level.

All of those electrons detected come out from several depths of the target (see Figure 2.2). The intensity of photoelectrons emitted I, depends on the traveling distance of electrons before they reach the surface. The XPS intensity drop is given by the Beer Lambert's relation below in terms of the effective attenuation length λ, layer thickness d and emission angle θ :

Equation 2.2 $I = I_0 \exp(-d/\lambda Cos\theta)$,

where I_0 is the intensity before the signal is attenuated.

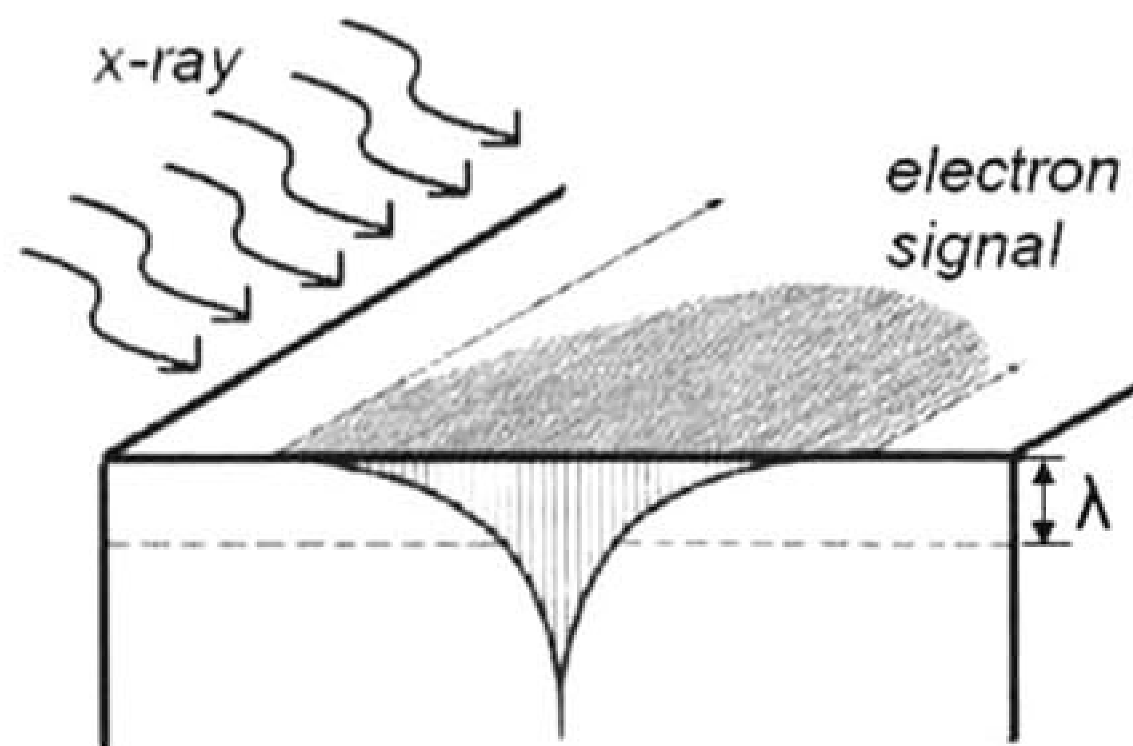

Figure 2.2 Dependence of the intensity detected as a function of the depth.

2.2 Spectrum interpretation

All those electrons with a binding energy less than that of the x-ray could be ejected from different core levels for building the 'signature' of the material better known as the XPS spectrum. The Figure 2.3 shows the spectrum of a TaN/ La-Hf based dielectric/Si stack layer. The peaks represent the electrons that escaped from the material without energy loss during their traveling path, whereas, the background describes the electrons that suffered energy loss.

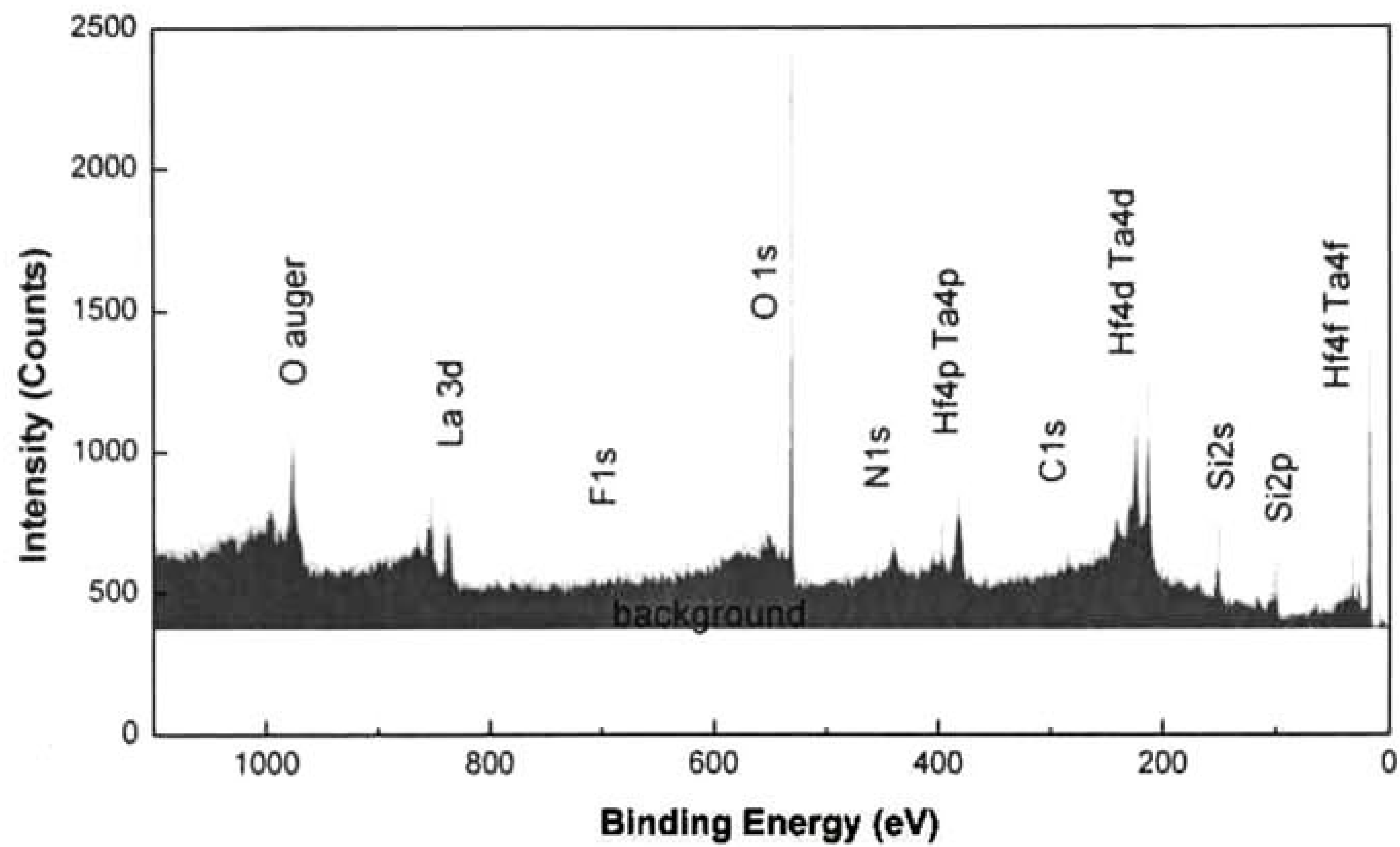

Figure 2.3 Photoelectron spectrum of a TaN/ La-Hf based dielectric/Si stack layer. The peaks represent the electrons that escaped from the material without energy loss and the background belongs to those that suffered energy loss.

The intensity of the peak is a measure of the number of the electrons of a core level in a pure atom or chemically bonded in a molecule. The intensity of the peaks in a same atom depends also, of the type of core level. The intensity for the electrons of the orbital s is lower than the intensity of the orbital p but these are lower than those of the orbital d. The spectrum for the orbitals p, d, and f exhibits a band compounded by two peaks (doublet) whereas the orbital s contains only one peak (singlet). The Figure 2.4 shows a singlet feature of oxygen, O 1s.

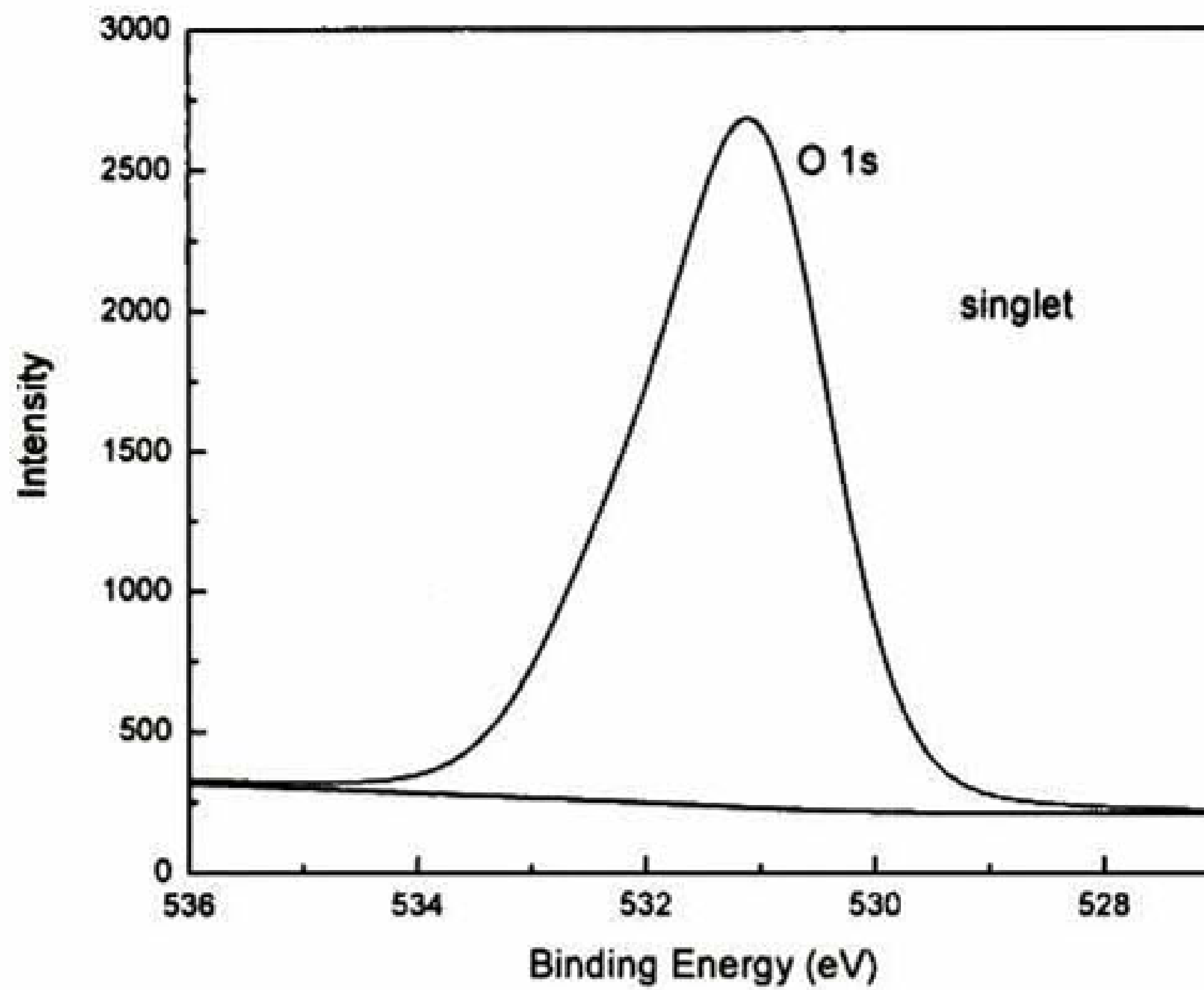

Figure 2.4 The spectrum of the orbital type s has a band with only one peak (singlet).

The Figure 2.5 shows the doublet corresponding to hafnium 4f. It can be appreciated other features that describe completely the spectrum such as the ratio of intensity and the distance (spin-orbit splitting) between the peaks of the doublet

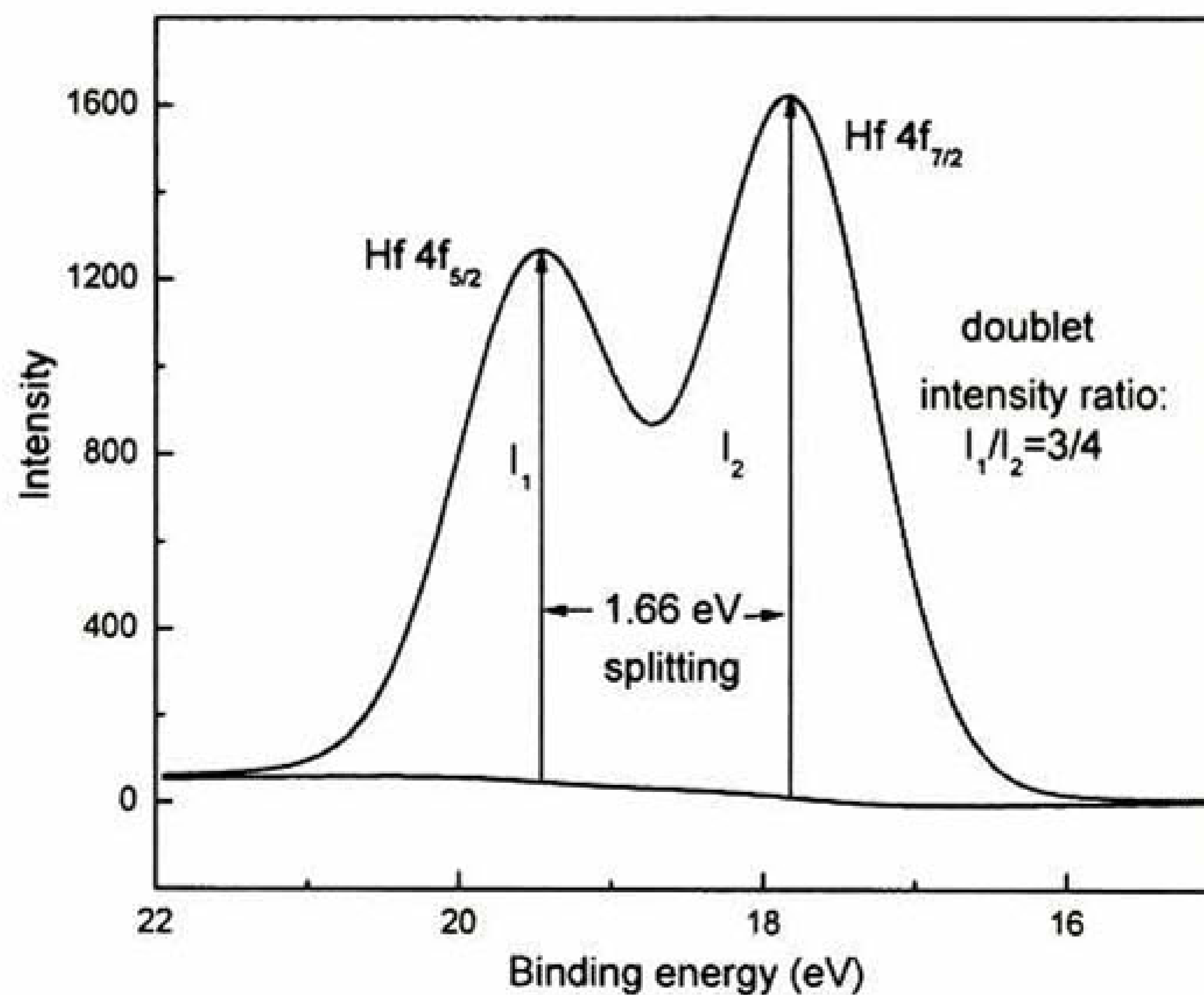

Figure 2.5 The Hf 4f feature is a doublet composed by two peaks, Hf $4f_{5/2}$ and Hf $4f_{7/2}$. The ratio of intensity is of 3/4 and the splitting of 1.66 eV between them.

The ratio of intensities of the peaks of each doublet are 0.5 (p orbitals), 0.666 (d orbitals) and 0.75 (f orbitals). These values arise from the occupancy numbers in the respective orbitals.

Figure 2.4 and Figure 2.5 show the background (red line) as well. The integral background is the most common shape of it that appears in the XPS spectrum. This type of background is increasing towards the higher binding energy as a slope line. This is due to the accumulation of the background generated by the photoelectrons scattered coming from the core levels associated to the peaks.

The binding energy of a particular photoelectron depends of its chemical environment. A pure atom can oxidize or reduce when is bonded with any other atom or atoms different to it. The oxidization phenomenon that occurs in a determined atom is visualized in the XPS spectrum as a shift on the binding energy towards a higher value from the energy in its pure state. The opposite occurs if the photoionized atom is reduced; the binding energy of the peak of intensity is lower than that of the pure atom. Figure 2.6 shows the signals of Si-Si and Si-O-Si bonds and the shift in energy (≈2 eV).

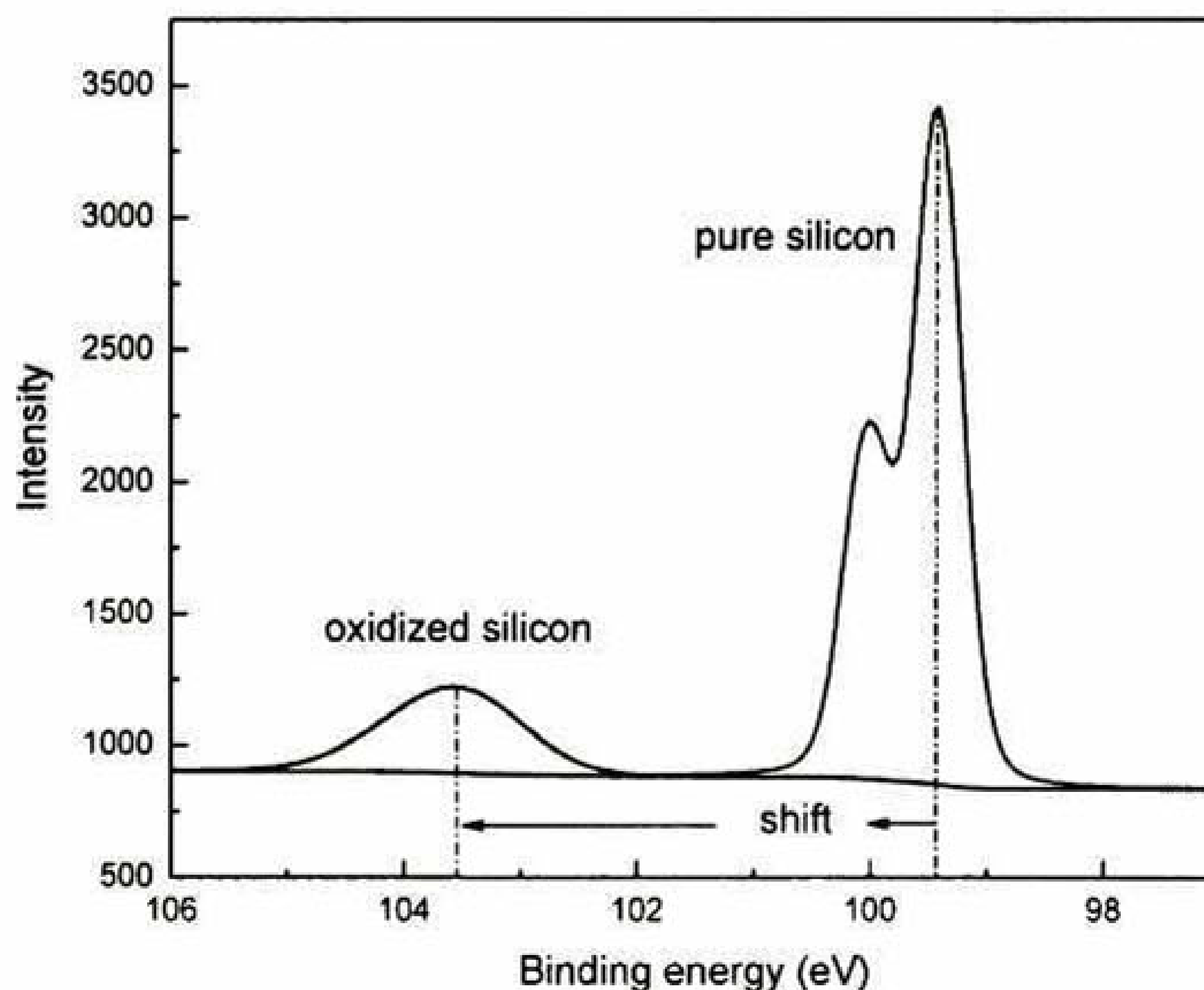

Figure 2.6 Signal of pure silicon is centered at ≈99.4 eV and silicon oxide at ≈ 103.5 eV. The chemical shift is 4.1 eV.

2.3 Instrumentation

A XPS spectrometer is built with three principal modules: a sample, an x-ray source and a photoelectron-detector. Some equipment includes an additional component, a crystal monochromator.

Commercial spectrometers are designed to reach ultrahigh vacuum (UHV) pressures between 10^{-8} to 10^{-10} mBar.[2] UHV is required to avoid sample contamination with any residual molecules of gas kept inside the module of analysis and that can react with the surface of the sample. Also, molecules absorb and scatter photoelectrons causing attenuation of the signal.

2.3.1 The Sample

Solid, liquids and gaseous samples can be measured in a XPS spectrometer. Insulating layers on a conducting or semiconducting sample are studied too. Any sample to be characterized must be stable under UHV conditions.

2.3.2 X-ray Source

The source of *x*-ray is generated from a material or target previously excited with electrons at high energy. The electrons extracted form a thermal source or heated filament are accelerated applying a potential: between the filament (it is connected at ground) and the target (anode) that is at a positive potential commonly in the 10-15 kV range and strike on the target. As a consequence, the x-rays are emitted. The energy of the x-ray generated depends on the type of anode. The *x*-ray flux generated in the anode is proportional to the current produced in the filament and the efficiency of the *x*-ray emission to the energy of the electrons. The anodes more commonly used are of Al (Al K_α: 1486.6 eV) and Mg (Mg K_α: 1253.6 eV). The process is shown in Figure 2.7.

Some commercial spectrometers have included an *x*-ray monochromator with the objective of narrowing the energy width of the *x*-ray, for example, the energywidth of the K_α line is reduced from 0.9 eV to 0.25 eV. The main advantage of using a monochromator is observed in the XPS spectrum, the peaks are narrower than those detected without monochromator. A peak well defined gives better chemical state information.

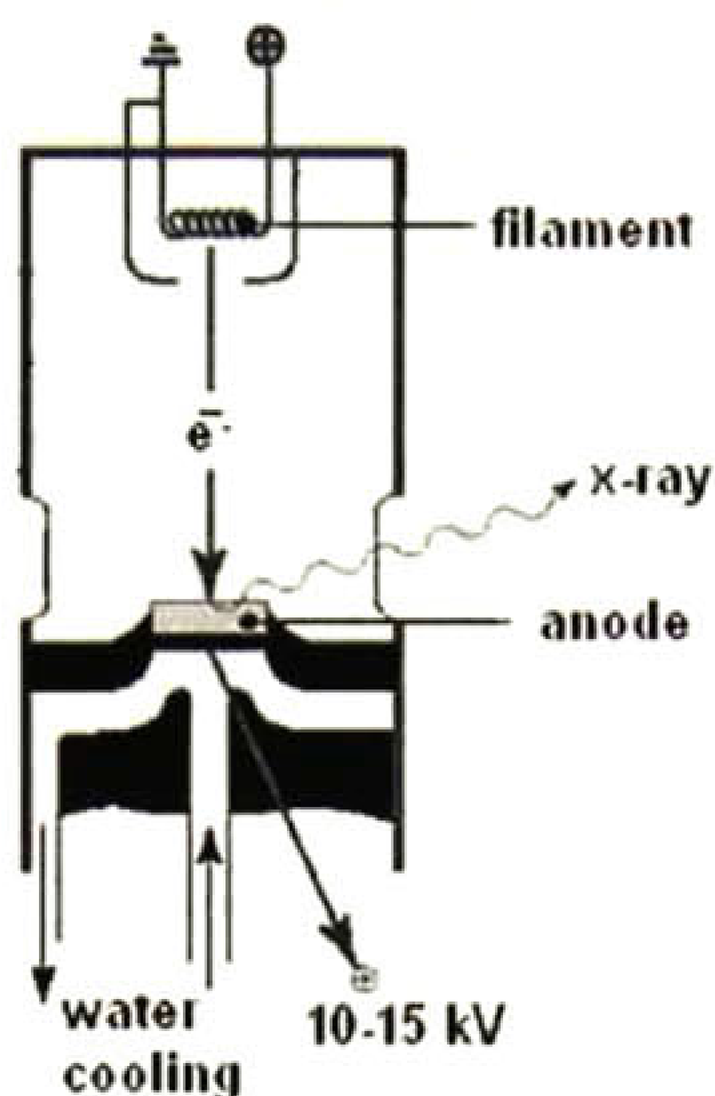

Figure 2.7 Generation of x-rays. Electrons are accelerated from a filament towards a target or anode due to the difference of potential between them. The electrons strike on the target generating the emission of x-rays.

2.3.3 Detection system

The high resolution and transmission required in the XPS spectrum is achieved with an electron detection system as the Hemispheric Sector Analyzer (HSA) formed by: the analyzer, lens and multichannels detector. Figure 2.8 shows the elements of a HSA. The analyzer is formed by the outer and inner concentric hemispheres of radii R_1 and R_2 respectively, in which is applied a potential ΔV in such way that the electrons are deflected and confined inside the region between the hemispheres when they pass across the analyzer with a constant kinetic energy E (pass energy) that depends on the potential and is given by

Equation 2.3 $$E = e\Delta V\left(\frac{R_1 R_2}{R_2^2 - R_1^2}\right),$$

where e is the charge of the electron. Electrons with a slightly higher or lower energy than E will pass throughout the analyzer towards the system of detection where they are collected and setting in channels in order to the energy. Before of the detection, the electrons travel and they hit on the tube walls and generate secondary electrons. A gain of 10^8 can be achieved using an amplification system.[3]

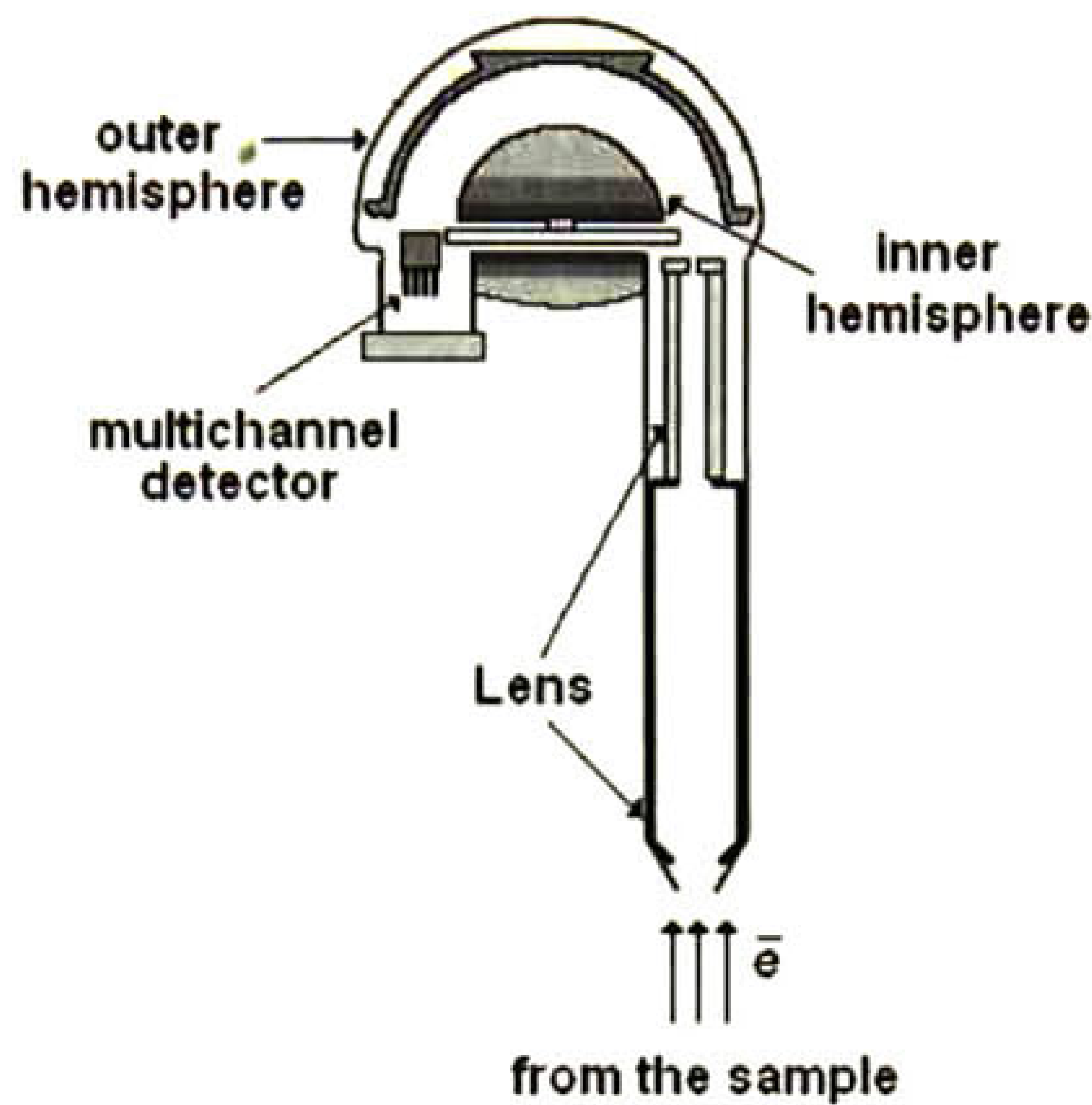

Figure 2.8 Schematic diagram of an electron detection system.

There are two types of operation modes for HSA:

- Constant Analyzer Energy (CAE). It is mainly used for XPS experiments because it can provide high resolution spectra for chemical states of the elements present. The electrons travel in the analyzer at constant energy or pass energy in the range of 1 eV to several hundred of eV. Small pass energy (15 eV) means to obtain a good resolution and sensitivity on the spectra as it was mentioned above, whereas a large one (50 eV) is appropriated to collect a wide scan or survey of the spectrum that contains all of the electron signals ejected from the experimental sample. For the last case, chemical information or quantitative analysis it can not be extracted. The placing of magnetic lens between the sample and the input of the analyzer let to collect electrons from a very wide range of emission angles and furthermore, a high electron transmission

- Constant Retarded Ratio (CRR). This mode is preferable to be used for Auger Electron Spectroscopy when wide range scans are to be taken and the energy resolution needed is poor.

2.3.4 Detectors

In some spectrometers, the electrons arriving to the detector need to be individually counted. The module used to achieve it is the channel electron multiplier or channeltron.

2.4 Quantitative analysis

The quantitative analysis is achieved considering a set of parameters related to the XPS instrument and the sample.

The parameters related to the instrument are:

- The transmission function of the spectrometer, which is the proportion of the electrons transmitted through the spectrometer as a function of their kinetic energy. The transmission function is provided by the manufacturer.
- The efficiency of the detector is the proportion of the electrons striking the detector which are detected.
- The effect of magnetic fields affects the transmission of the electrons at low kinetic energy.

The parameters related to the sample are:

- The attenuation length of the electron emitted, which is the distance that it can travel without losing energy. This factor depends upon of the kinetic energy of the electron and of the nature of the sample.
- The photoelectron cross section, which is related to the probability of that an electron is emitted due to a photon incoming in the sample. The cross section depends upon the element and orbital of which the electron is emitted and the energy of the photon.

There are some techniques able to provide information about the chemical composition as a function of the depth, Ar^+ sputtering XPS, Secondary Ion Mass Spectrometry (SIMS), Rutherford Backscattering Spectroscopy (RBS) amongst others. However, some of them are characterized as destructives techniques.

2.4.1 Angle Resolved XPS

Although XPS provides elemental and chemical information on the surface, the concept can be extended to determine the elemental and chemical composition as a function of the depth. According to the Beer-Lambert equation, (see Section 2.1) the detected intensity can change as a function of the angle of photoemission. As it can be appreciated in the Equation 2.2, the intensity of the peak increases for detection angles close to the surface normal and decreases to grazing angles, the effect is illustrated in the Figure 2.9. The intensity coming from a ultra-thin silicon oxide film on top of a silicon bulk can be detected at any angle and it change slightly, whereas that detected from the bulk is more sensitive to small angles (normal to the surface) , and it decreases at grazing angles.

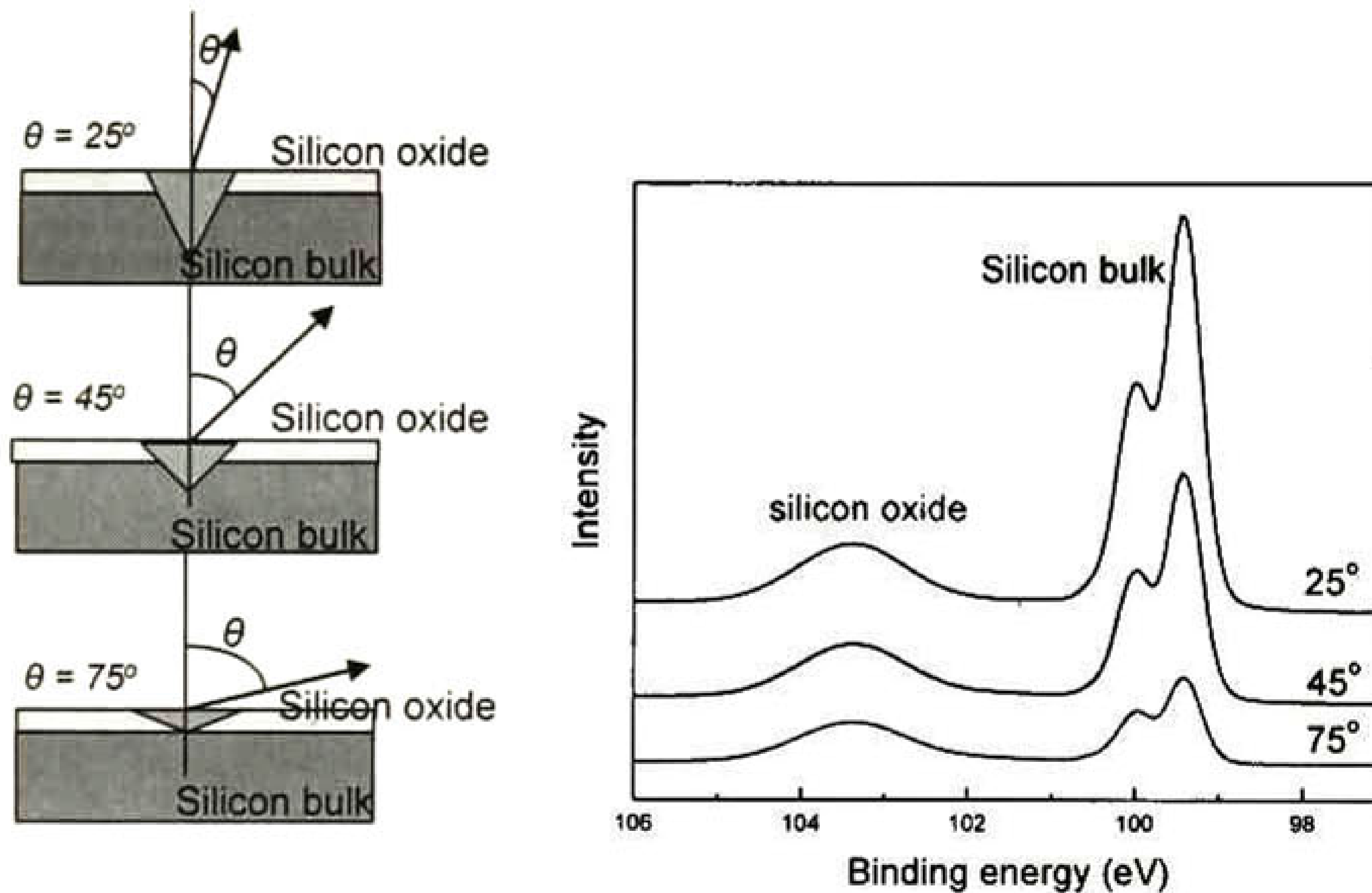

Figure 2.9 Angular dependence of the intensity. The Beer-Lambert equation provides information about the chemical composition as a function of the depth

These are the fundaments for Angle Resolved X-Ray Photoelectron Spectroscopy. Experimentally, one way to do XPS at several angles (ARXPS) is tilting the sample and to keep the source and the detector in a same position.

The Beer-Lambert equation is applied when there is only one layer. But in the case of having more than one layer the physical phenomenon is more complex. It is convenient

to build a physical model which considers each layer as a different 'barrier' through it the electron passes before reaching the surface.

The chemical depth profile can be modeled with layered structure.[4,5] Figure 2.10 is a diagram sketching a layer stack on a substrate.

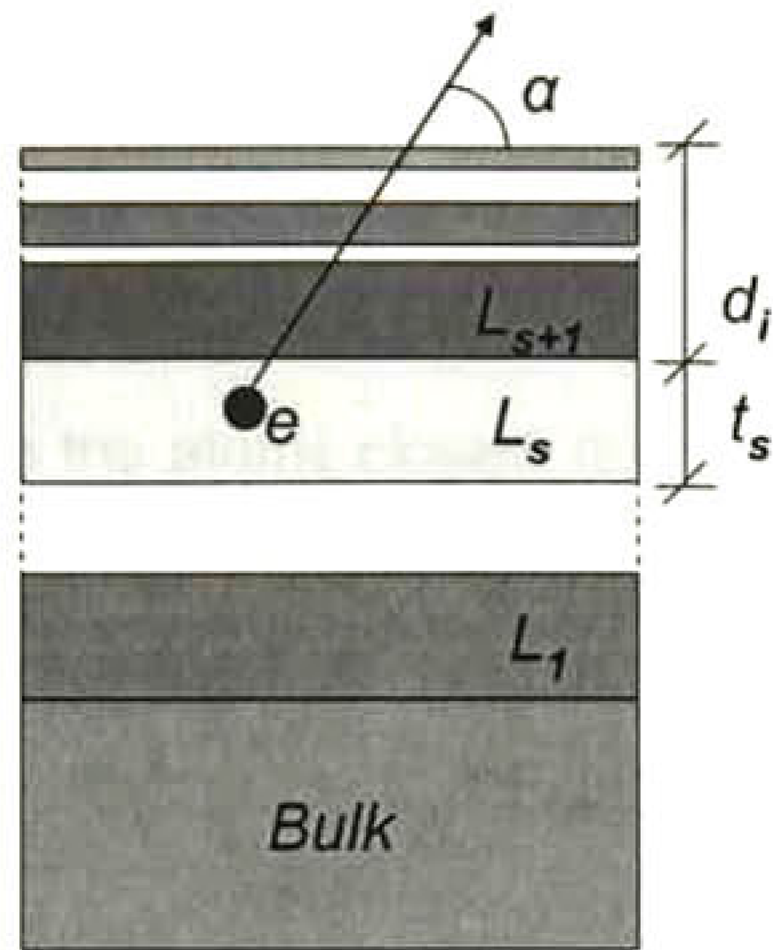

Figure 2.10 The chemical depth profile of the different species in a layer stack on top of a bulk can be modeled employing the ARXPS peaks intensities, the parameters of the layers and the instrument.

The intensity at which the photoelectron of the specie *S* goes out from the sample at an angle α is given by[6]

Equation 2.4
$$I_S(\alpha) = X\ A\ \sigma_S\ N_S \frac{1-\exp\left(-\frac{t_S}{\lambda_S \sin\alpha}\right)}{1-\exp\left(-\frac{a_S}{\lambda_S \sin\alpha}\right)} \prod_{i}^{\text{layers above } S} \exp\left(-\frac{d_i}{\lambda_{S,i} \sin\alpha}\right),$$

where X is the intensity of the x-ray, A is the efficiency of the analyzer, σ_S is the photoelectron cross section, t_S is the thickness of the layer *S*, N_S is the concentration of the specie *S* in the layer *S*, a_S is the atomic spacing of the layer *S*, λ_S is the attenuation length of the photoelectron from the specie *S* as it travels through the layer *S*, $\lambda_{S,i}$ is the attenuation length of the photoelectron from the specie *S* as it travels through the layers *i* above, and d_i is the depth of the layer *S*. This model is applied to conformal and uniform layers.

2.4.2 Ar^+ Sputtering XPS

The observation depth in XPS can be as small as 10-20 Å[3] If is required to know the composition through deeper layers, one way to do that, is removing shallower layers by means of sputtering.

In sputtering technique, the surface is bombarded by heavy ions such as Ar^+ or O^+ with low energy (0.5-20 keV[3]). The atoms from the surface are hit by the ions and the ejected. The number of atoms ejected depends upon the energy of the ions, the target material and the ion species (see Figure 2.11).

With Ar^+ sputtering XPS once the atoms closest to the surface are removed, XPS data of the new surface is collected. This process is carried out several times, is to say, XPS data at different depth can be collected.

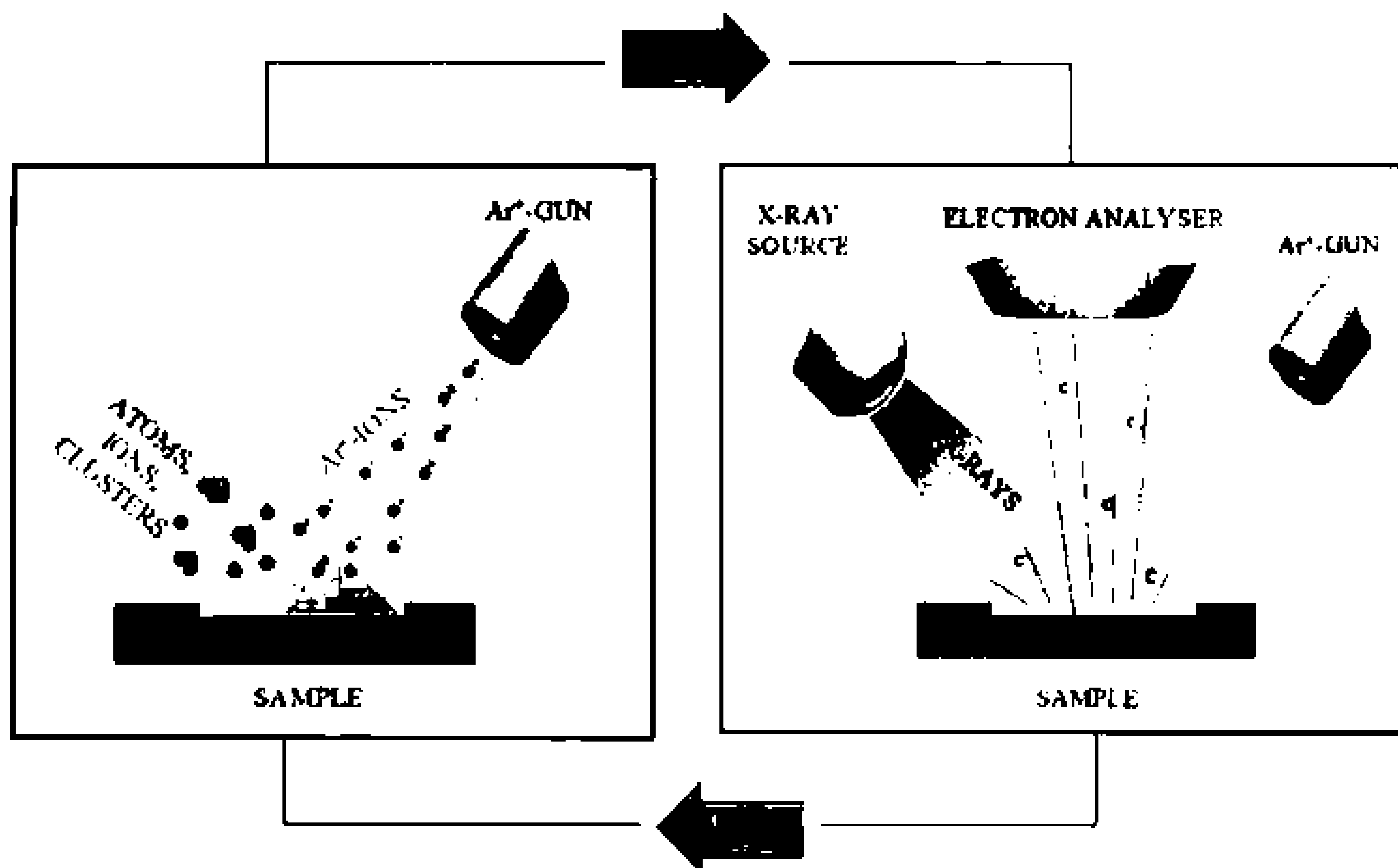

Figure 2.11 Ar^+ Sputtering XPS as a cyclic process.

References

1 Full Automatic X-Ray Photoelectron Spectroscopy XPS-7000. The Rigaku Journal 1987, Vol. 4.

2 J. F Watts, and J. Wolstenholme. An Introduction to Surface Analysis by XPS and ESCA, John Wiley & Sons, 2003.

3 L.C.Feldman, J.W.Mayer. Fundamentals of surfaces and thin film analysis, Elsevier Science Publishers.

[4] A. Herrera-Gomez, F.S. Aguirre-Tostado, Y. Sun, R. Contreras-Guerrero, R.M. Wallace, Y. Hisao, and E. Flint. Rapid Communications, Surface and Interface Analysis. In print.

[5] A. Herrera-Gomez, F.S. Aguirre-Tostado, G.K. Pant, M. A. Quevedo-Lopez, Paul D. Kirsch, J. Wang, M. Kim, B.E. Gnade, and R.M. Wallace. "Thermal stability of nitrogen in nitrided HfSiO2/SiO2/Si(001) ultrathin films." (To be published).

[6] A. Herrera-G6mez, A. Hegedus, P.L. Meissner. "Chemical depth profile of ultrathin nitrided SiO_2 films." Applied Physics Letters 81, p. 1014 (2002), and references there in.

Chapter 3. Experimental techniques

The experimental techniques employed in this thesis are described in this chapter. Atomic Force Microscopy (AFM) was useful to know the uniformity of the chemical etching during the sample preparation. Fourier Transform Infrared Spectroscopy (FTIR) was able to show some bonds arrangement changes. ARXPS gave us the essential information to quantify these and other bonds with the objective of finding them spatially distributed through to the sample giving more detailed information about the composition of the studied films.

3.1 Wet chemical etching

Semiconductor technology requires the cleaning of wafers to avoid impurities contamination capable to affect all the process to carry out during the fabrication of a device. The purpose of cleaning the wafer is to have a suitable surface to deposit films on top of it. There is a broad variety of methods to do that; these are selected in order to the desirable film characteristics for a specific application. Also, several chemical substances (etchants) have been investigated for removing atoms selectively in a film.

The preparation of any sample begins with the wafer cleaning. The sequence of chemical solutions used to clean a wafer depends upon the contaminants present and the requirements for its subsequent application. A procedure commonly used consists of the next steps:

- Organics and metals removal. The First step is to eliminate organics from the surface due to the environment contaminants. Piranha clean (H_2SO_4/H_2O_2) is a solution used for this purpose. This solution is highly oxidizing, left the silicon surface with an oxide layer. Generally, the temperature range for heating this solution is 80-110°C.

- Oxide Silicon removal. Because of the first step and the native oxide easily grown on Silicon after brief exposure to the air, silicon surface needs to be cleaned with Hydrofluoric Acid (HF). Once the oxide is removed, Si is passivated with H (H-terminated) and the surface becomes hydrophobic. This step is done at room temperature.

- Particles and metals removal. Standard Cleaning Procedure better known as RCA has been the primary cleaning method used by the industry in Si MOSFET processing and developed by RCA Corporation. It consists of two kinds of solutions[1]:
  - SC-1: De-Ionized Water (DIW H_2O): Ammonium Hydroxide (NH_4OH): Hydrogen Peroxide (H_2O_2).
  - SC-2: De-Ionized Water (DIW H_2O): Hydrochloric Acid (HCl): Hydrogen Peroxide (H_2O_2).

The temperature range of operation for each clean up is 50-90°C. For both substances, the concentration of the reactants varies. SC-1 attacks organic impurities and is used because the oxide removal step tends to add particles to the wafer surface. It oxidizes the film surface or passivates it to avoid further organic and particle contamination; SC-2 removes alkali cations and heavy metal impurities. RCA cleaning left an oxidized surface. SC1 is used for most of the metals. In a test done[2] on all the candidate high-k/metals, NH_4OH was found to be highly selective for all of them. Rinse with DIW is required to eliminate contamination or impurities left between each chemical etching. Rinse times are on the order of 2-10 minutes each for these rinses. The RCA clean up procedure used for the Si wafers of this work is shown in the Table 3.1:

Table 3.1 Standard Cleaning for Si wafers procedure

Step	Solution (%vol)	Solution temperature (°C)	Time (min)
1	H_2SO_4:H_2O_2 (6:1)	85	10
2	DIW rinse of Si	Room Temperature (RT)	1
3	DIW:HF:H_2O_2(4:1:1)	RT	1
4	DIW rinse of Si	RT	1
5	DIW:NH_4OH:H_2O_2(5:1:1)	80	5
6	DIW rinse of Si	RT	1
7	DIW:HCl:H_2O_2(6:1:1)	85	10
8	DIW rinse of Si	RT	1
9	HF + DIW (1:50)	RT	1

The last step is optional and is recommended to carry out before using the wafer for processing. The Figure 3.1 shows a RCA clean up hood (in the clean room of UTD) picture where the wafers were cleaned.[3]

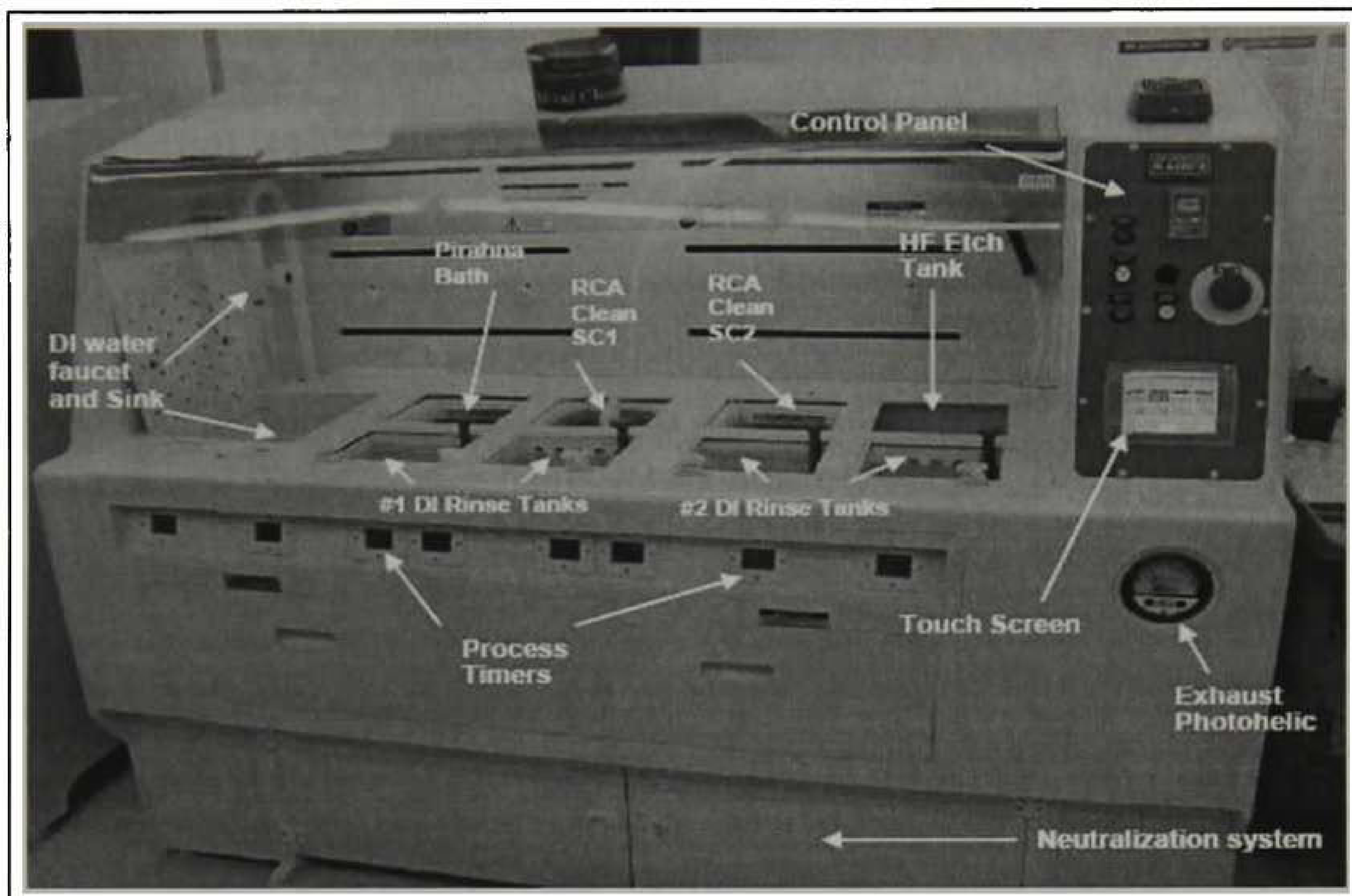

Figure 3.1 RCA Cleanup hood identifying the principal operating features.

Another Important etchants to review are:

- Potassium hydroxide (KOH) solution at 80°C is a wet etchant for orientation dependent Si (ODE). The planes with high bond density are attacked more slowly than the others planes. KOH stops etching on very heavily doped p-type Si.[4] The KOH commercial solution is about 29% KOH by weight, the rest is water. When the solution is used, is recommended to agitate it to obtain a uniformity etch rate throughout the solution because KOH tends to stratify.
- Acetone, methanol, isopropanol or isopropyl alcohol (IPA), are used to remove organics such as photoresist.

- As it was mentioned above, DIW is widely used as diluent, chemical cleaning and rinsing agent in many wafer cleaning process steps.

It is recommended for best results that the wet etching is done with fresh solutions, agitating occasionally. Due to the vapors created by the solutions, all the wet etching must be done under fume hoods.

3.2 Thermal treatment (RTA)

The processing of devices after depositing the high-k material requires the dopant activation of Si wafers that typically involves annealing to high temperatures of ≈ 1000°C. RTA is an alternative annealing process with the advantage of heating wafers in short times (for a few seconds), typically a temperature above 1000°C and a precise control of the temperature ramp (temperature versus time).

The main advantage of using RTA over conventional furnace annealing techniques is the short time duration at difference to furnace techniques where is required longer times (around of minutes). The use of longer annealing times facilitates dopants diffusion which is not desirable for semiconductor applications. However, performance of high temperature annealing can lead to a number of problems. Many high-k crystallize at these high temperatures and crystallization tends to affect some electrical properties.

The annealing profile is based in a recipe compounded by several steps strung together between them. The resulting profile consists of three principal parts: the delay, the ramp and the steady. Each one is created by set parameters that control the desirable temperature.

The delay part is present at the beginning of the annealing process when the chamber door is open and at the end when it is closet.

The ramp occurs at the range time when the temperature is raising or falling. The ramp period is between the delay and the steady behaviors. In the steady step, the sample is kept at constant temperature in a specified period of time. The RTA used for this purpose was the Jipelec Jetfirst 200 Rapid Thermal Processor (see Figure 3.2) with the next characteristics:

Performance:

- Temperature range: ambient to 1300 °C
- Ramp rate: 1°C/s to 300 °C/s
- Pyrometer control: 150 °C to 1300 °C
- Features:
- Cold wall chamber technology
- Pyrometer and thermocouple temperature control
- Atmospheric and vacuum process capability
- One purge gas line
- Vacuum valve and vacuum gauge
- PC control

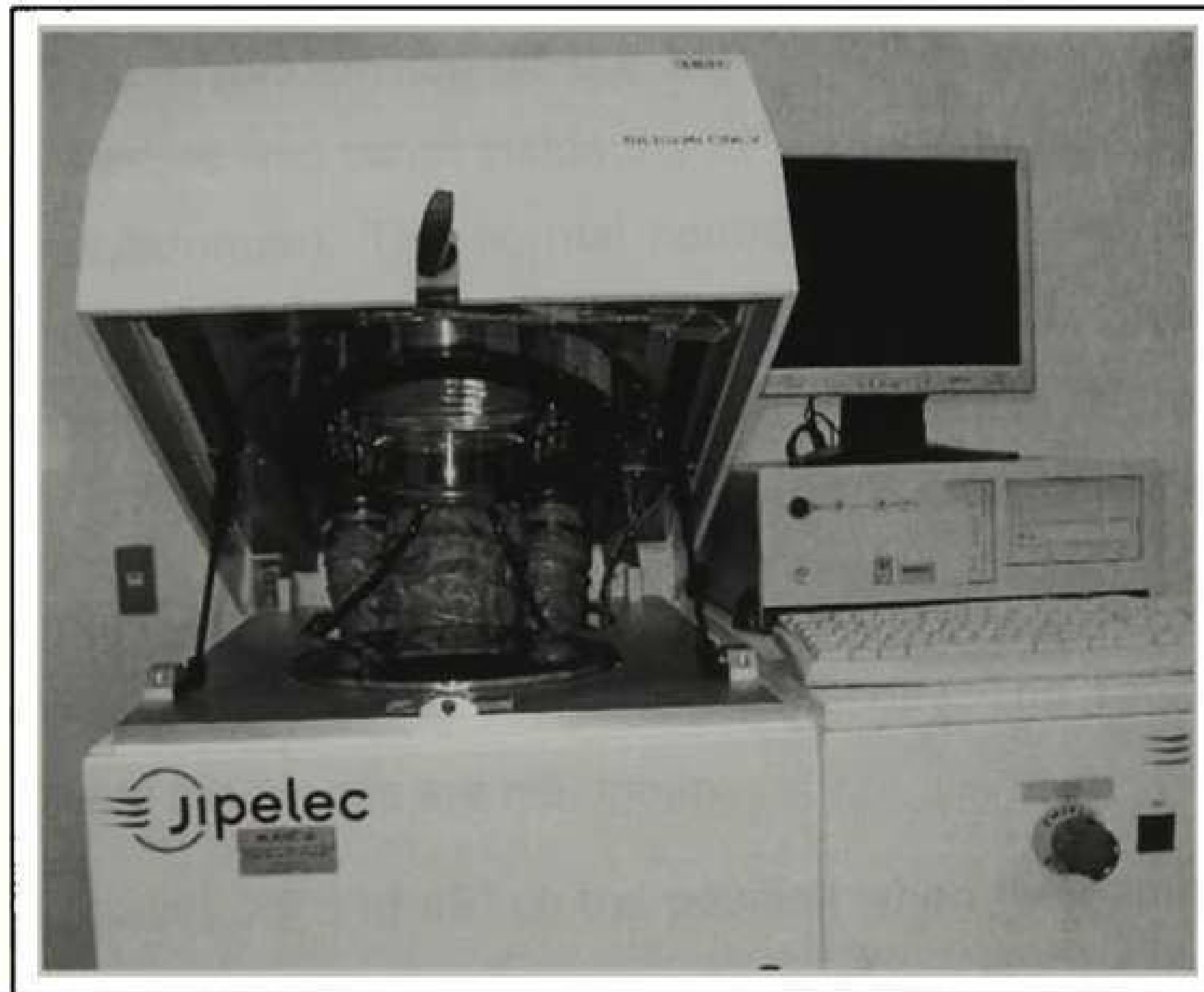

Figure 3.2 Jipelec Jetfirst 200 Rapid Thermal Processor used for annealing wafers (RTA).

All the deccaping process must be done in an acids fume hood as is shown in Figure 3.3.

Figure 3.3 Samples deprocessing in the acids hood.

3.3 ARXPS experiment

De-processing of the layers on top of the high-k is necessary to perform the XPS measurements. A sample was taken inside the XPS chamber (see Figure 3.4) in a small sample holder (molybdenum). The normal conditions inside the chamber to do XPS measurements are: ultrahigh vacuum and room temperature. Sample was irradiated with Al Kα monochromatic x-rays (1486.7 eV). The parameters of the X-ray source were 300 mA and 15 kV. The process carried out for the XPS experiment was:

- System alignment in "y" direction (counts maximization): X-ray source, electron analyzer, surface of the sample and optic microscopy. The sample was fixed in the "y" direction where the counts are maximum.
- A fast scan or survey XPS at 45° (is the position when the sample is 45° respect to the analyzer) was done with the purpose of identifying the different signals detected in XPS.
- Heating of the sample in situ in a radiative mode at 250°C for 15 min (Figure 3.5).
- Cooling of the sample down to room temperature to perform the XPS measurements.

- Sample alignment for ARXPS measurements. Counts maximization at $X_{average}$: is the average of X_{25}° (the sample is 25° respect to the analyzer) and X_{75}° where the counts are maximum in the x direction. This step consists in the alignment of the sample for ARXPS measurements.
- Sample was positioned in $X_{average}$. In this step the sample had a fixed position in x, y and z (manipulator direction).
- A software (Cascade®) developed for ARXPS experiment was used for the data acquisition: XPS at 25°, 35°, 45°, 55°, 65°, and 75°. With this algorithm, the XPS control system was able to move the motor 8000 steps equivalent to 10° between each XPS measurement.

The XPS analytical module from UTD can be seen in the next picture:

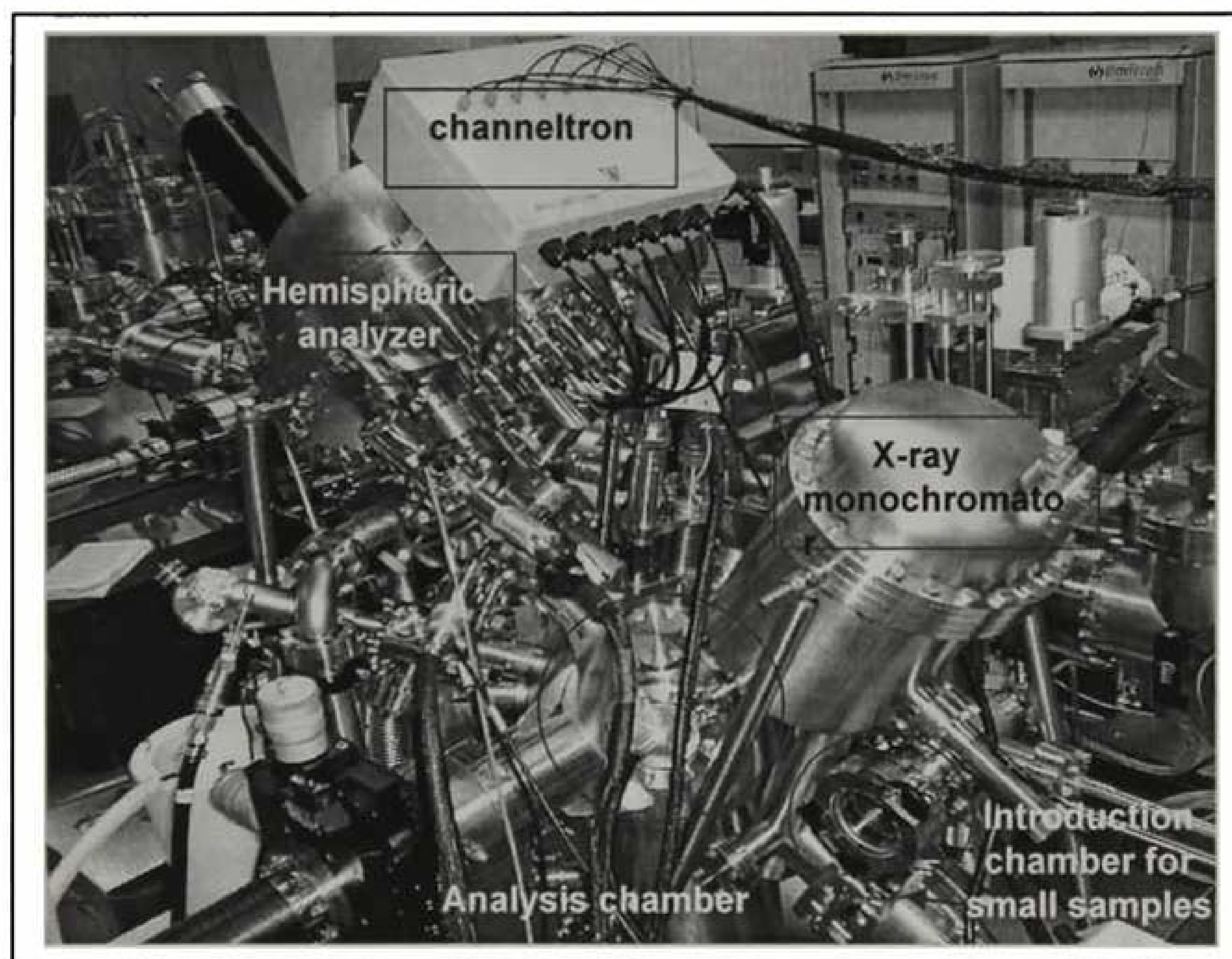

Figure 3.4 XPS analytical module from the University of Texas at Dallas. Principal components: analysis chamber, introduction chamber for small samples, hemispheric analyzer, channeltrons and x-ray source showing only the x-ray monochromator

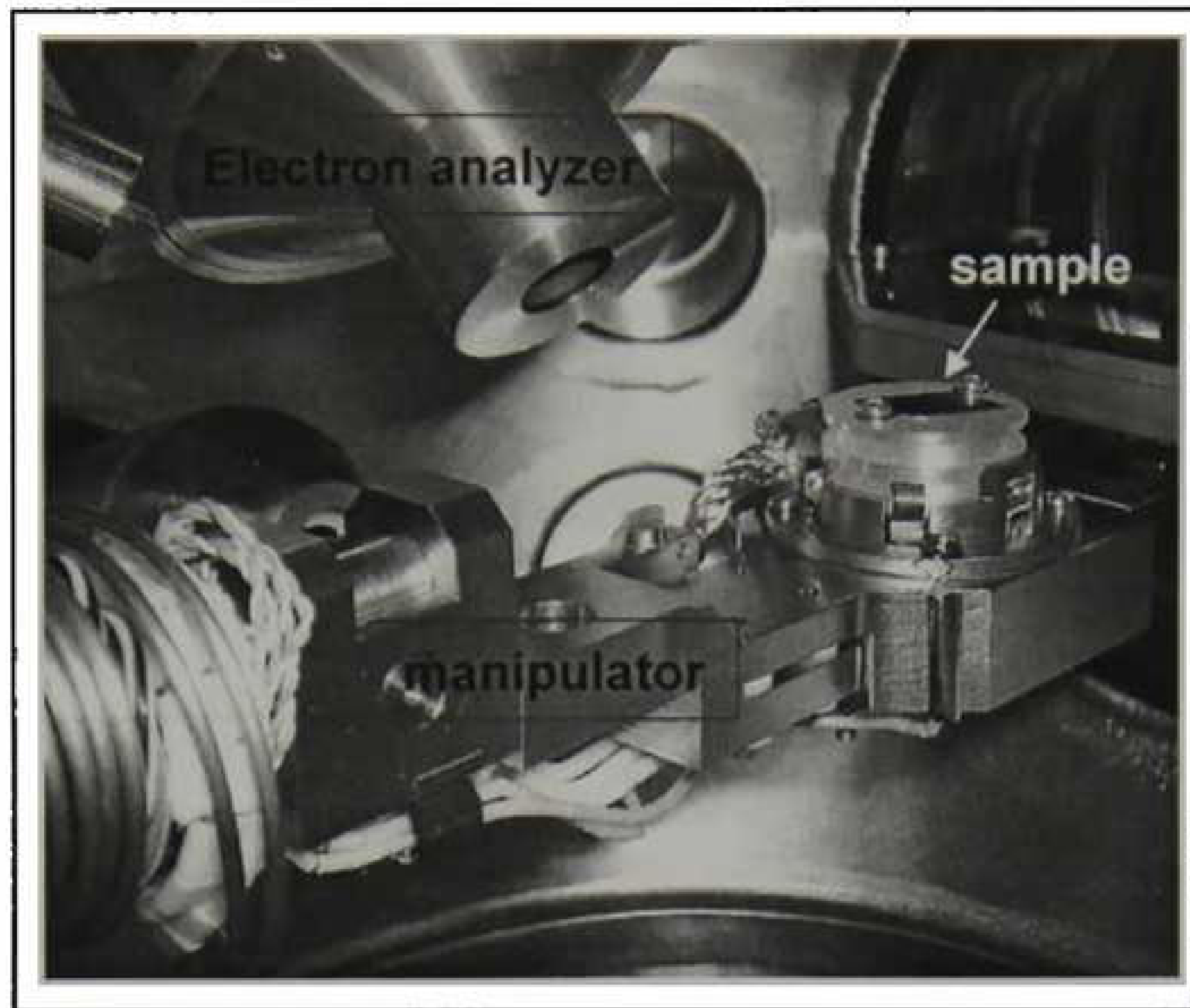

Figure 3.5 Small samples are placed on a small sample holder inside the XPS analysis chamber as it shown in the picture.

3.4 Atomic Force Microscopy (AFM)

3.4.1 Basic principles

Atomic Force Microscopy is nowadays a tool used for scanning the surface topography. Its principal use is to measure surface features that are very small (in the order to 2.5 Å as diameter[5]), which it is not possible to do with conventional microscopes.

In AFM an image is achieved by the raster scanning across the surface of the sample using a probe or 'tip'. During that, a constant force is maintained between the probe and the sample. A source of laser is emitted and reflected on top of the cantilever that contains the probe in its downside towards a system of photodiodes that detect the light lever which is directly proportional to the deflection of the cantilever. A feedback control system (FCU), force sensors (FS), and an electromechanical transducer are the components necessary for AFM measurements. The Figure 3.6 describes the components:

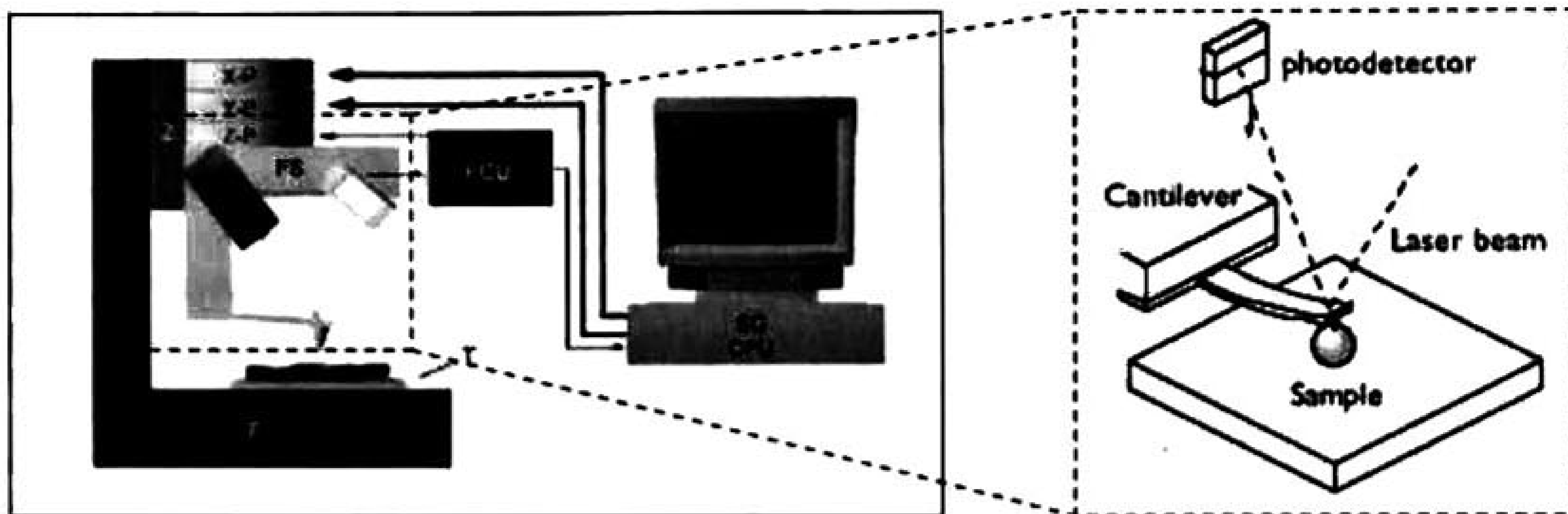

Figure 3.6 Components and subsystems of an AFM system.

There are two methods to measure the force probe in AFM:

Deflection or contact mode. The force of the probe is kept constant during the measurement and the deflection of the cantilever is directly measured (Figure 3.7(a)).

Vibrating or non-contact mode. The cantilever vibrates and the changes in the amplitude of vibration and phase are measured (Figure 3.7(b)).

Figure 3.7 (a) In contact mode AFM the probe directly follows the topography of the surface as it is scanned. (b) In vibrating mode, changes in probes vibrations are monitored to establish the force of the probe onto the surface.

In AFM, measurements of resolution are done in the plane of the measurement and perpendicular to it. Resolution in the plane depends upon the geometry of the probe; a sharper probe gives the best contour of the features on the surface, so, higher resolution. The vertical resolution is determined by vibrations such as acoustic noise, floor vibrations, and thermal vibrations.[5]

3.4.2 AFM experiment

Smooth film surfaces are desirables after any chemical etching. For this reason, topography measurements on the sample surface were done by AFM. The equipment used was the Multimode Scanning Probe Microscope from Veeco Instruments.

The experiment consisted of the next steps:

- Place the probe in the microscope and align the light lever sensing system.
- Focus the surface of the sample in the microscopy and place the probe to the captured field.
- Moving down probe (manually) carefully to avoid a possible breaking of it with the sample. Be sure to position the cantilever a sufficient distance from the surface of the sample and keep it.
- Let the software approximates itself the probe to the surface (engage in the z direction).
- As the last step, look for the adequate parameters until find an image with good resolution.

Four samples of 0.5 x 0.5 cm^2 with previous de-processing were measured. The samples were MS3 and MS4 annealed and unannealed. A longer time was required when looking for the optimum parameters in order to achieve an image with a good quality. The parameters manipulated were: scan size, scan rate, samples/line; proportional and integral gain. Several scan size were used for each sample: 1 µm x 1 µm, 500 nm x 500 nm and 200 nm x 200 nm.

3.5 Fourier Transform Infrared Spectroscopy (FTIR)

3.5.1 Basic principles

It is possible to identify the presence of different molecules in the sample with FTIR. This technique is very useful for obtaining the vibration of specific functional groups in the sample. The amount of each material present can be related to the peaks intensity of its respective bands.

FTIR is a method that gives a sample spectrum frequency in a short time (order of few seconds). The technique consists of using an infrared source, an interferometer which its function is providing an infrared spectra range of 'encoded' frequencies in a unique signal. The infrared light passes through a sample of interest where is transmitted and reflected. Depending on the features of the sample, some frequencies are absorbed (vibrations frequencies of the sample). Finally, the beam of light goes out towards a detector to be measured (interferogram signal). All these last are the components of a spectrometer. This measured signal (acquisition time about 1 second) is 'decoded' with computational software which has implemented a mathematical Fourier Transformation. The result is a spectrum where individual infrared frequencies are obtained.

The instrumental process is presented in the Figure 3.8.[6]

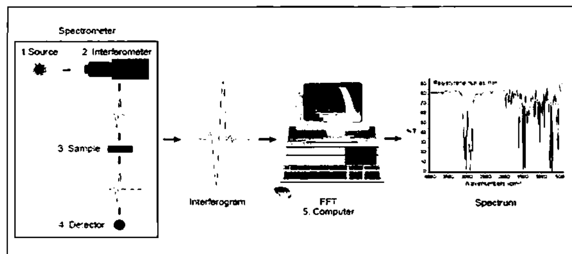

Figure 3.8 Instrumental process for obtaining a frequency spectrum with FTIR.

3.5.2 FTIR experiment

Three new samples of ≈ 3 cm x 3 cm were the target for this experiment, a MS3 and MS4 subject to RTA (1000°C/5 sec in N_2) and another MS4 not annealed as a reference. In the same way as before, these samples were de-processed previous to the FTIR measurements.

A Si wafer used as reference for FTIR measurements was cleaned with the RCA clean up procedure shown in the Figure 3.1. It is important to make the cleaning of the wafer

immediately before to carry out the experiment to remove the native oxide from the surface.

The equipment used was the Nicolet 6700 Spectrometer. The procedure to get the spectrum for each sample was fast. The most important realized steps were:

- Select the experiment: here the parameters are defined (number of scans collected, resolution, y-units and mode of the experiment).
- Collect the background spectrum (on the RCA clean Si wafer).
- Collect the sample spectrum.

References

1 W. Kern. Handbook of Semiconductor Wafer Cleaning Technology, Part I, William Andrew Publishing, 1993

2 M. M. Hussain, N. Moumen, Z. Zhang and B. F. Womack. Metal Wet Etch Issues and Effects in Dual Metal Gate Stack Integration, Journal of The Electrochemical Society, Vol. 153, No. 5, pp. G389-G393 (2006).

3 R. Robbins and A. Duenes. RCA Cleanup Hood Operations. The University of Texas at Dallas, Erik Jonsson School of Engineering, pp. 32 (2006).

4 K. R. Williams. Etch Rates for Micromachining Processing. Journal of Microelectromechanical Systems, Vol. 5, No. 4, pp. 256-269 (1996).

5 Atomic Force Microscopy: General Tutorial. Pacific Nanotechnology in Advancing nanotechnology.

6 Introduction to Fourier Transform Infrared Spectrometry, ThermoNicolet Corporation, 2001.

Chapter 4. Experimental results on the La samples

4.1 Samples

4.1.1 Samples as received

The samples were fabricated at Sematech and at the University of North Caroline. Their structure as received is schematically described in the Figure 4.1 and in the Table 4.1.

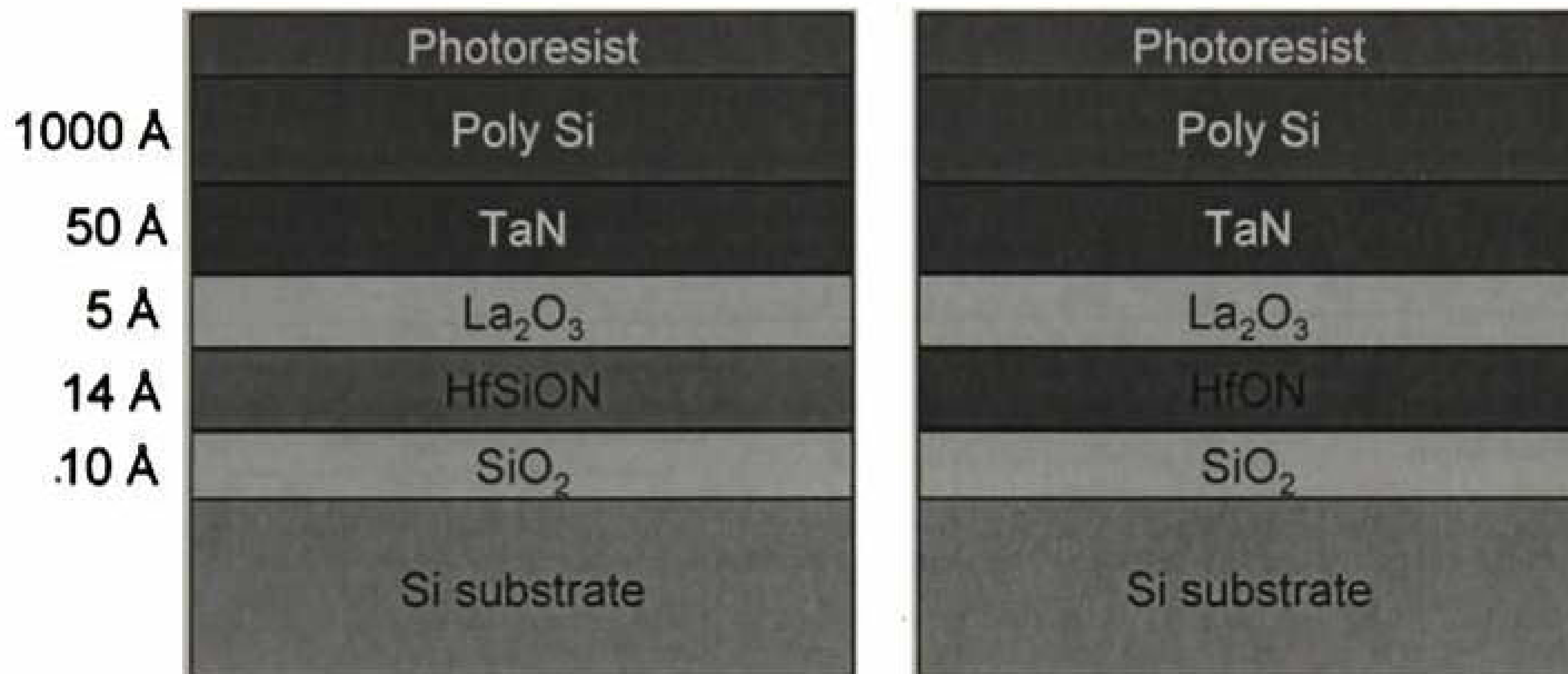

Figure 4.1 MS3 and MS4 sample structure as received.

Table 4.1 Brief description of the growth conditions for samples MS3 and MS4

	Conditions							
Sample	SiO_2	High-k	Metal capping	Nitrogen	Post deposit anneal	Metal electrode	Poly-Si	Cap
MS3	(10 Å)	$Hf_{0.9}Si_{0.1}O_2$ (14 Å)	La2O3 (5 Å)	16%	NH3 (700°C)	TaN(50 Å)	1000 Å	400 Å PE TEOS*
MS4	(10 Å)	HfO_2 (14 Å)	La2O3 (5 Å)	16%	NH3 (700°C)	TaN(50 Å)	1000 Å	400 Å PE TEOS*

The Tetraethylorthosilicate (TEOS*) is used as a hard mask to avoid the Poly-silicon oxidation duet to the atmosphere.

4.1.2 Thermal treatment

Pieces of the two samples (MS3 and MS4) of 1cm×2cm were cut from the wafers. After the removal of the photoresist (acetone at room temperature for 2 minutes) one of each was exposed to RTA (1000°C for 5sec in N_2, see Section3.2). The rest of them were

kept as control samples. The parameters used in the RTA are shown in the Table 4.2 and the temperature ramp in Figure 4.2.

Table 4.2 Recipe for RTA (1000°C/5 sec in N_2)

	Step										
Parameters	1	2	3	4	5	6	7	8	9	10	11
Temperature(°C) (setpoint)	25	25	25	25	25	1100	1100	1010	1010	25	25
Time (sec)	10	120	120	120	120	11	6	2	5	20	30
N2 (sccm) (setpoint)	0	0	1500	0	1500	1500	1500	1500	1500	1500	1500
Close primary valve	YES	NO	YES	NO	YES	YES	YES	YES	YES	YES	YES
Open purge valve	NO	NO	NO	NO	NO	NO	NO	NO	NO	YES	YES

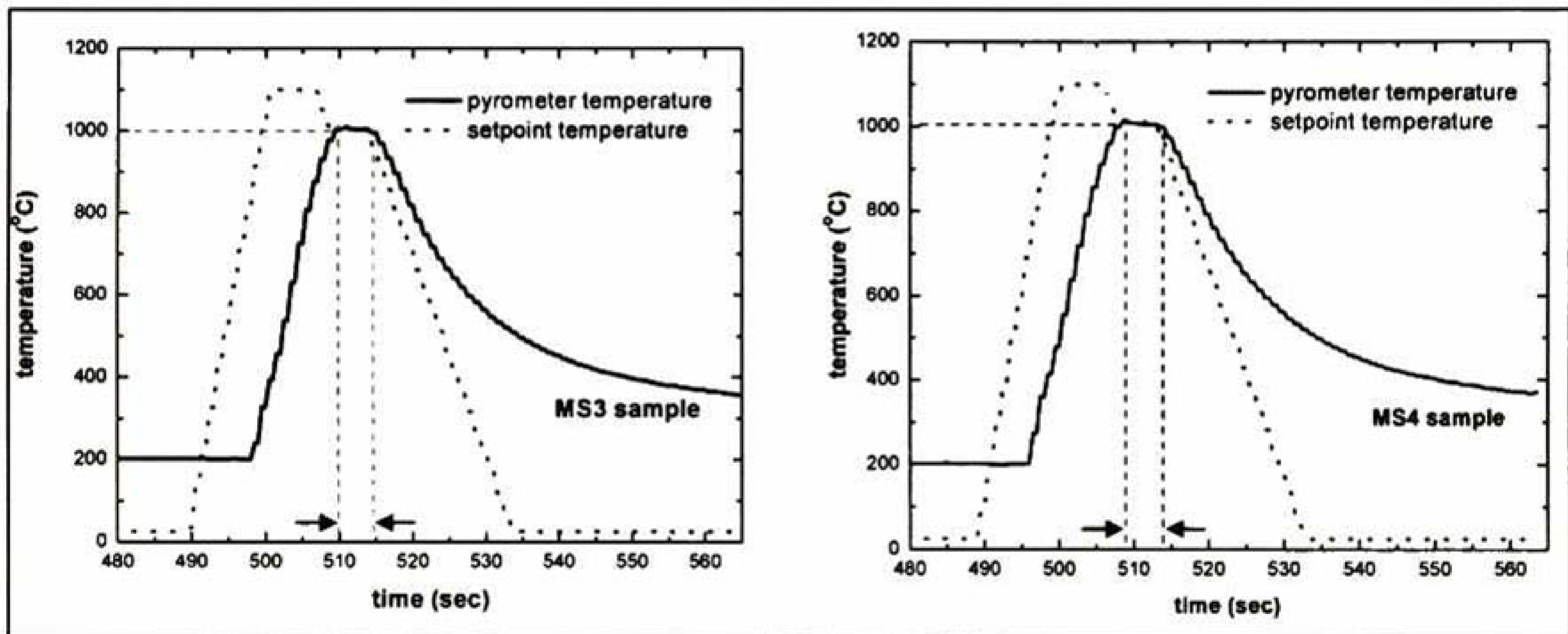

Figure 4.2 Annealing profile. The steady state indicates the range time (5 sec) at a constant temperature (1000°C) in N_2 environment. The structured recipe let a high control in the temperature profile during the RTA process

4.1.3 Sample de-capping

The wet chemical procedure to remove the series of layers on top of the delectric shown in Figure 4.1 was previously developed at UTD. It was necessary to remove these layers prior to the dielectric characterization. The materials and procedure used were:

Chemicals: 2ml of HF(50%), 15 ml of KOH (45%w), 10ml NH_4OH (29%w), 10 ml H_2O_2(30%w), DI water (17MΩ)

Material: glass beakers, Teflon bucket, test tube and thermometer.

Equipment: hot plate.

The chemicals employed and, the solutions are extremely dangerous, so, it is very important to wear the necessary personal protective equipment.

The steps carried out for de-processing were the next:

- The sample was immersed in the solution of HF1% in vol. at room temperature for 2 min. This solution is used to remove the silicon oxide.
- The remaining acid covering the sample was removed with DI water for a short time (≈ 20 sec).
- The sample was then exposed in a solution of KOH (15%vol) at 80°C for 2 min to remove the poly-Si.
- The remaining KOH solution covering the sample was removed with DI water one more time.
- The last solution used was SC1 (DI H_2O:NH_4OH:H_2O_2) to remove the TaN layer with 10:1:1 %vol at 80°C for 5 min. The solution is not efficient if the NH_4OH is added to the DI water in a time below 80°C, is important to mix them together exactly at 80°C, which it is not the case for H_2O_2. Hydrogen peroxide could be added at any time before the mixing of ammonium hydroxide.
- The remaining SC1 solution covering the sample was removed with DI water as a the end.
- The sample was then dried with N_2.
- As a finally step, the chemical waste was neutralized and disposed properly. The sample structure expected after the etching is shown in the Figure 4.3 and it is ready for its characterization in XPS.

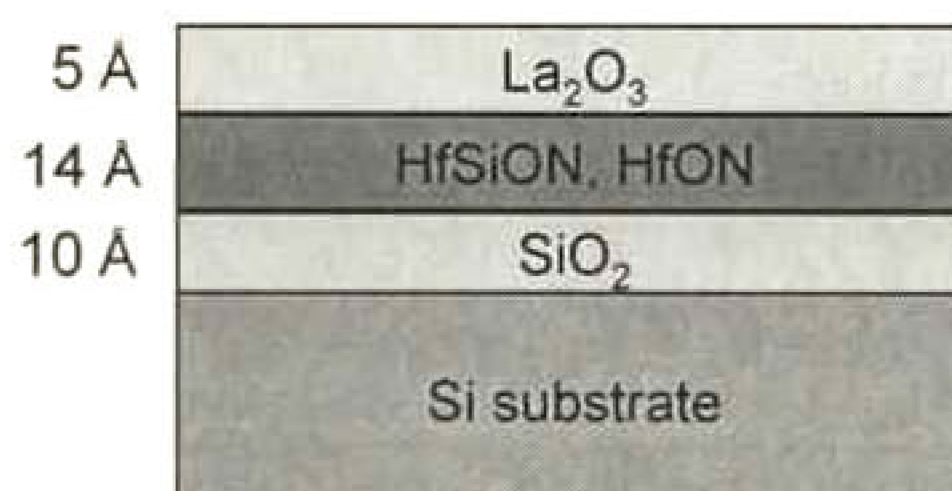

Figure 4.3 Sample structure resulting after the removal etching.

4.2 Effect of the chemical etching to MS3 and MS4 samples

After the chemical etching procedure described in the Section 4.1.3, several areas were scanned in tapping mode to obtain AFM images for the MS3 and MS4 samples. The topography of the surface and the images in 3D and the roughness average (R_a) obtained in each case are shown in the next figures:

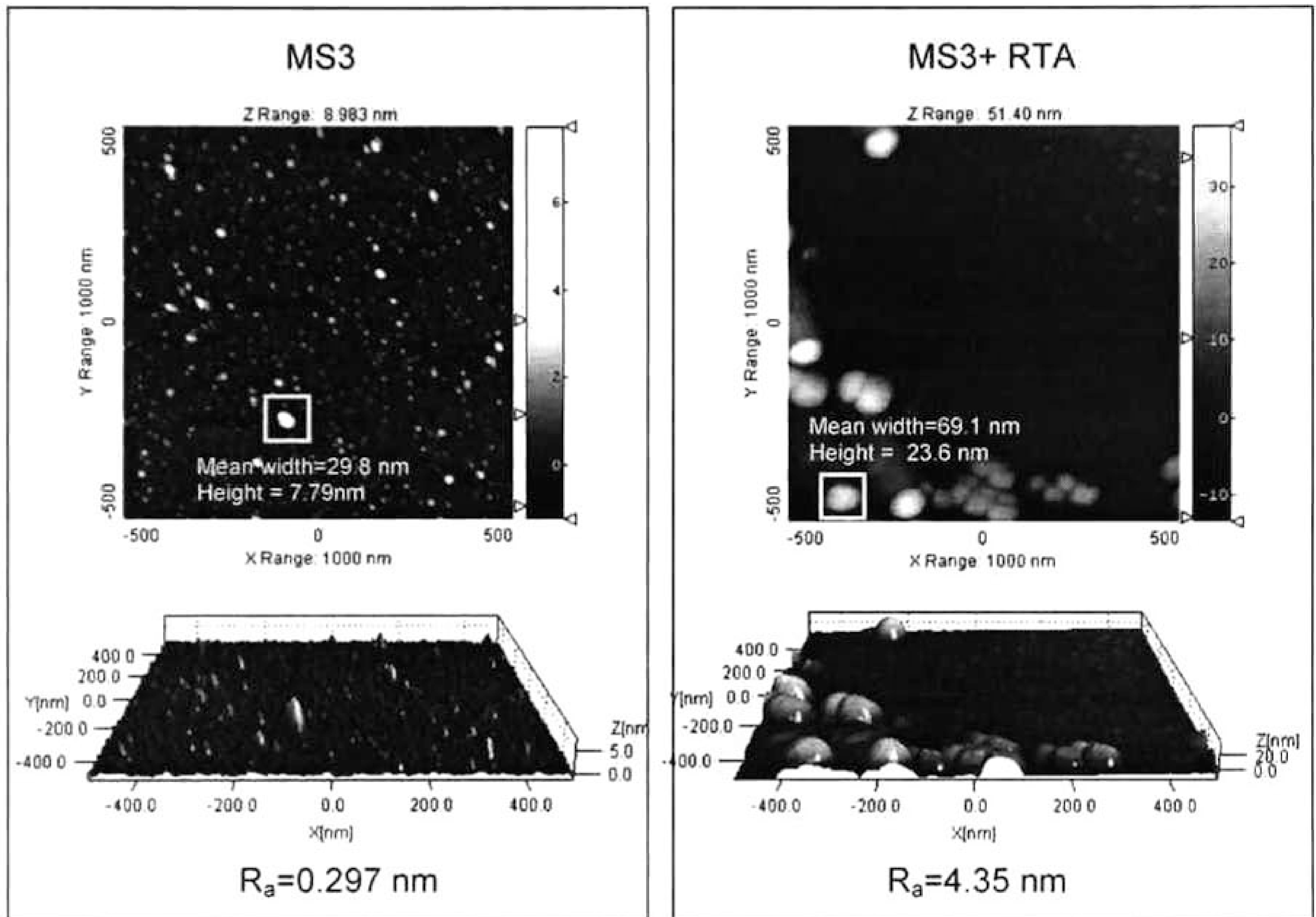

Figure 4.4 In the 1μm AFM scans of the MS3 sample it is possible to observe round features that protrudes from a flat surface. The concentration of these features was large enough to become a concern for the ARXPS analysis. The scans were obtained employing 512 lines at 0.488 Hz for the unannealed sample and at 0.458 Hz for the RTA sample.

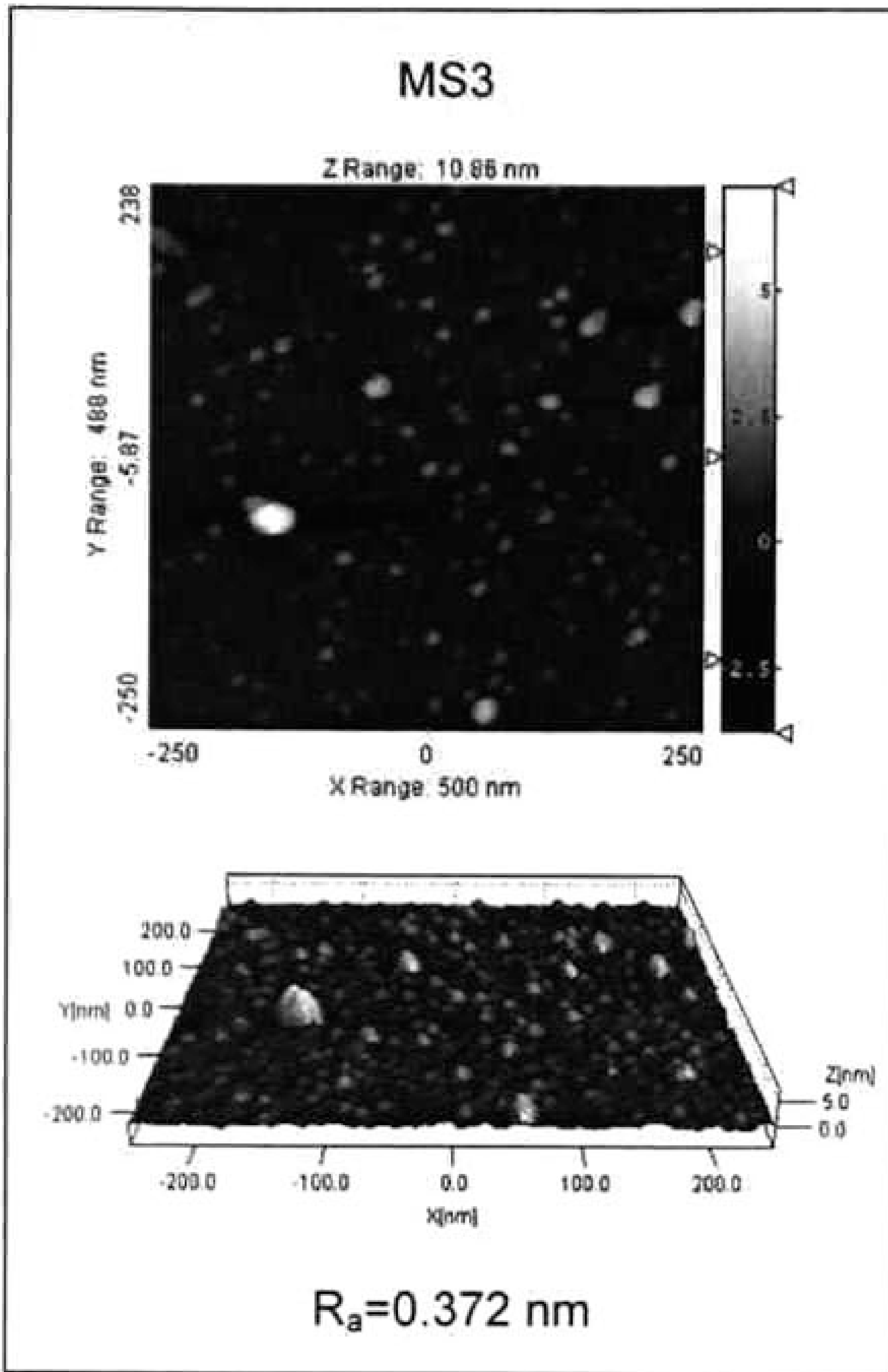

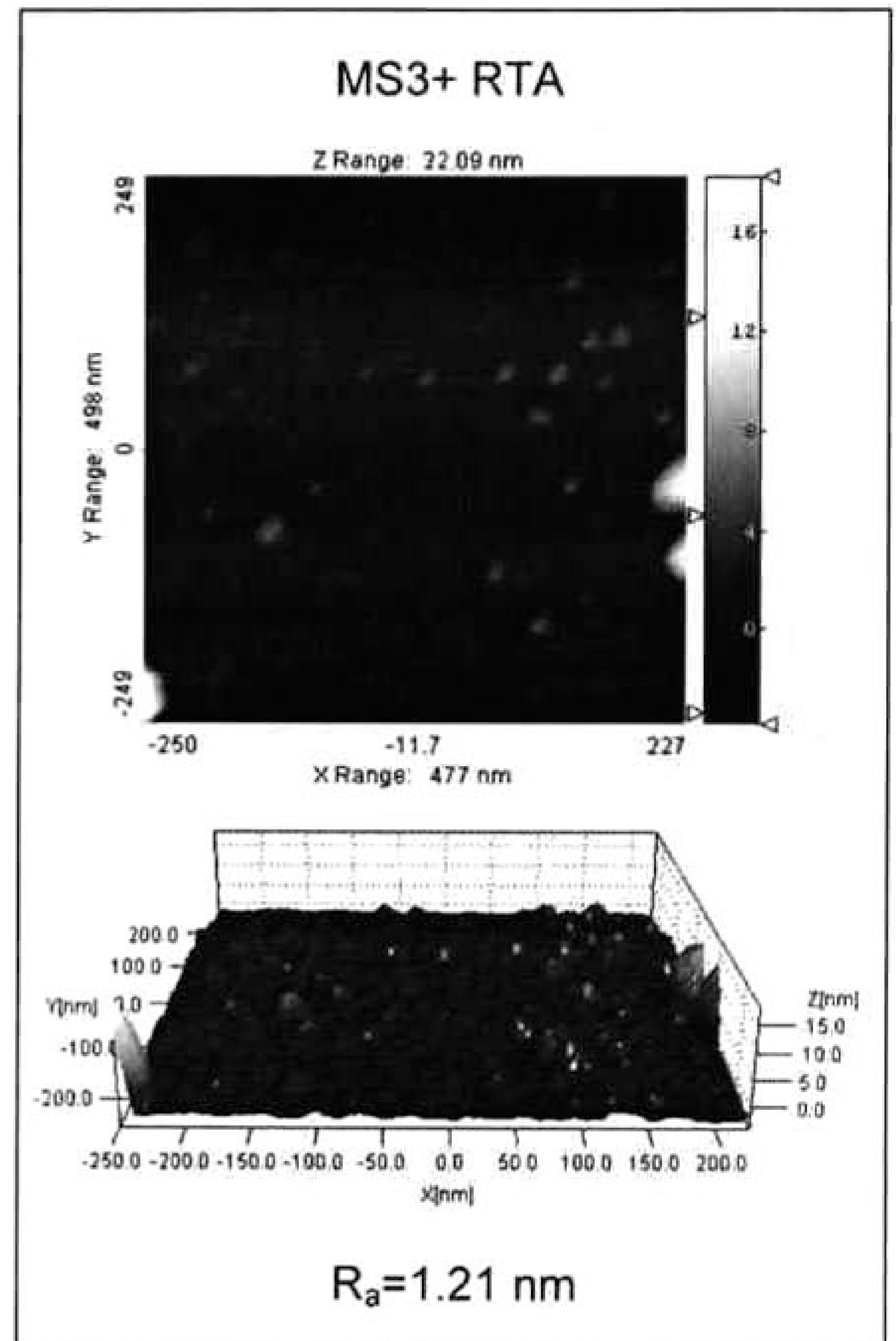

Figure 4.5 The region for the 500nm image was chosen away from the protrusions shown in Figure 4.4. Still, some smaller features stick out from the flat surface. The number of lines employed in the data acquisition was 512 and the rate was 0.392 for the unannealed sample and 0.4209 Hz for the RTA sample.

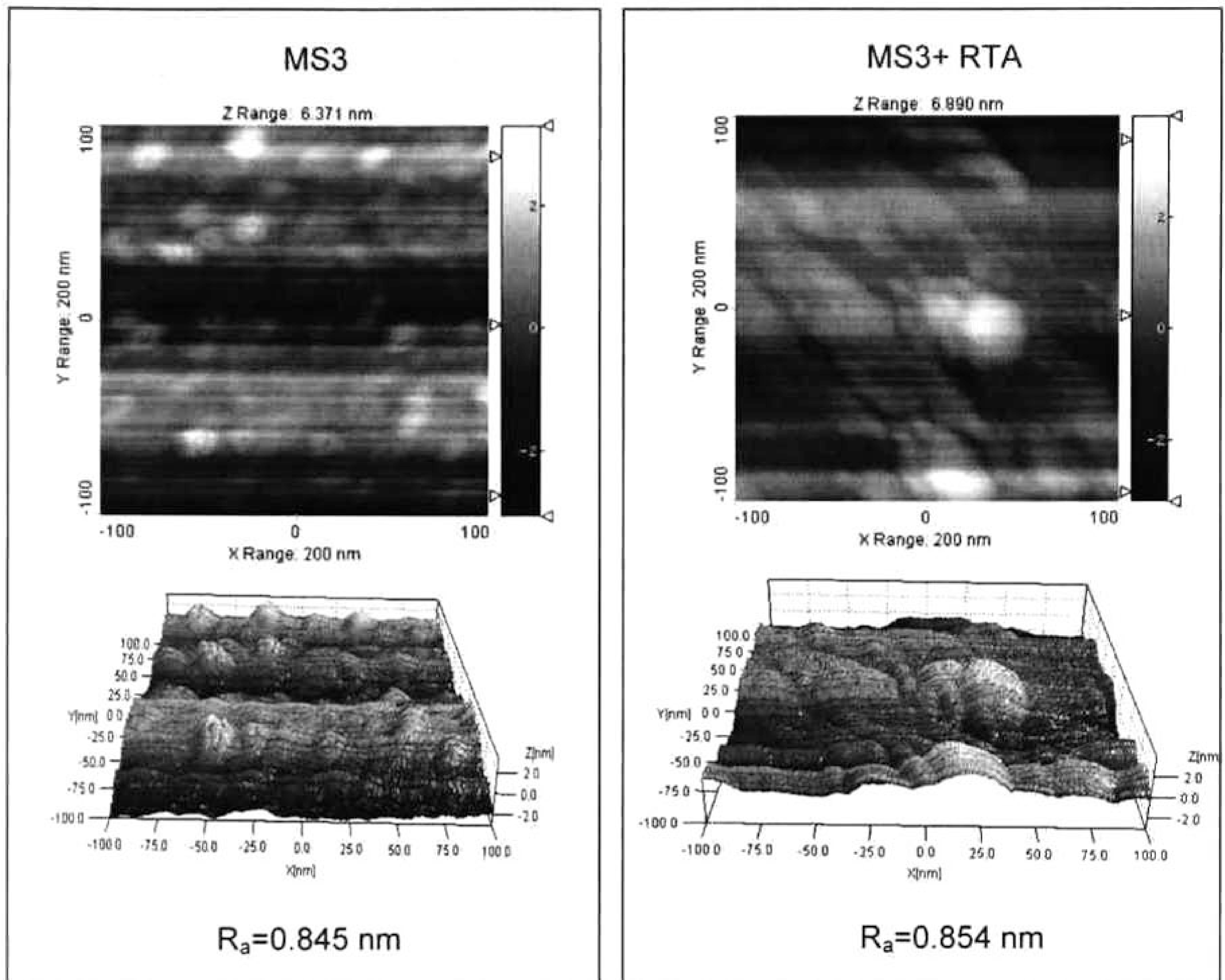

Figure 4.6 The irregular topography revealed by the 200nm images might be the consequence of lower scale protrusions. Lines for the scanned area were 512 and the rates of 0.392 and 0.618 Hz for the unannealed and the annealed samples respectively. The surface morphology shows some roughness even between the protrusions.

The MS4 samples were scanned in the same conditions but the images showed a better quality at the surface as it shown in the next figures:

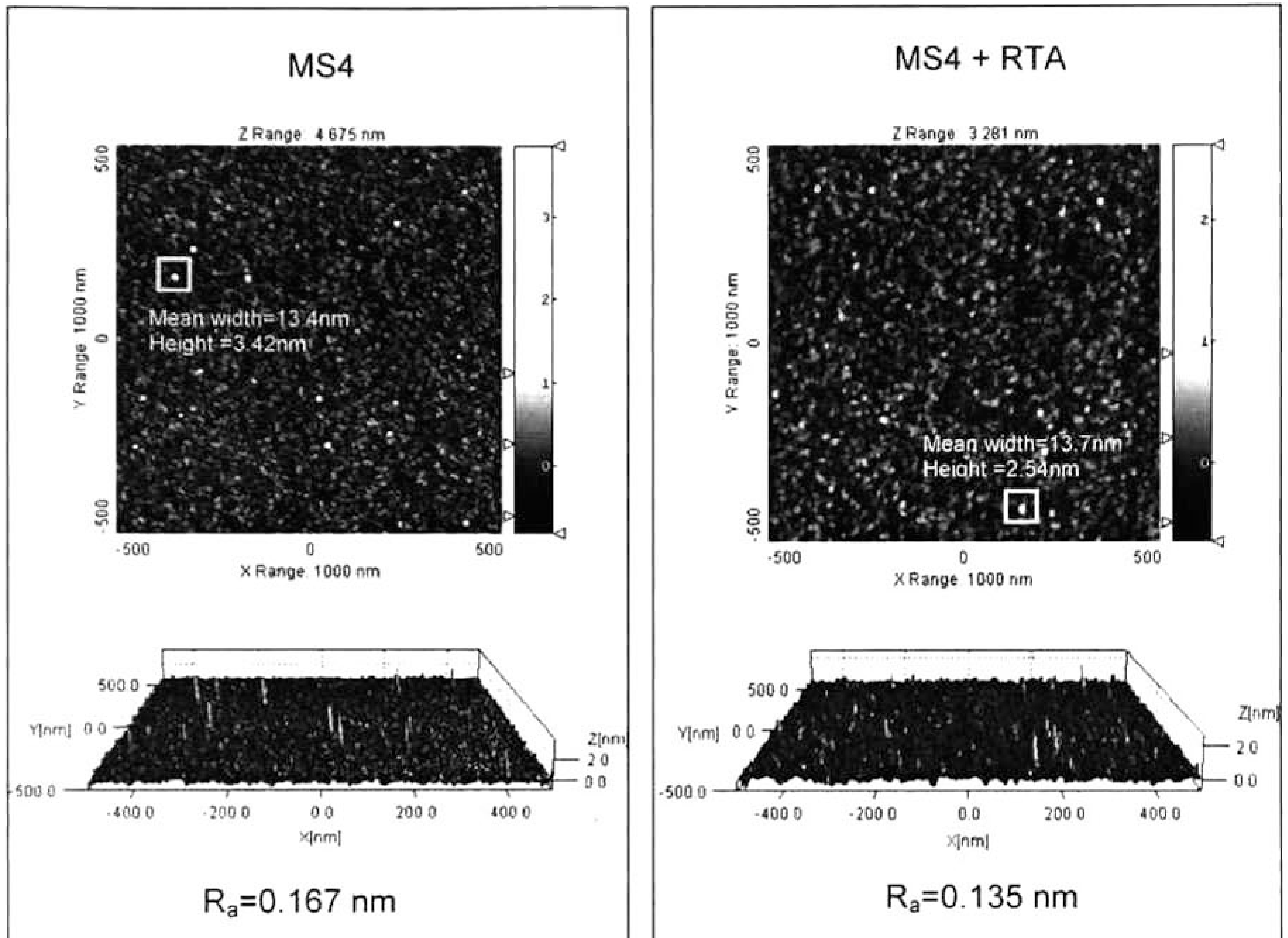

Figure 4.7 Very high quality and uniformity at the surface of 1μm of size scan for the unannealed and RTA samples were achieved. Some small features stick out from the flat surface can be appreciated (in the order of ≈ 10 nm). Also, is seen clearly the chemical etching affected the same way in both samples. Topography in the unannealed sample is more defined due to the number of lines for scan was of 896 and for the RTA sample was of 512. The rate was of 0.734 and 0.655 Hz for the each one respectively.

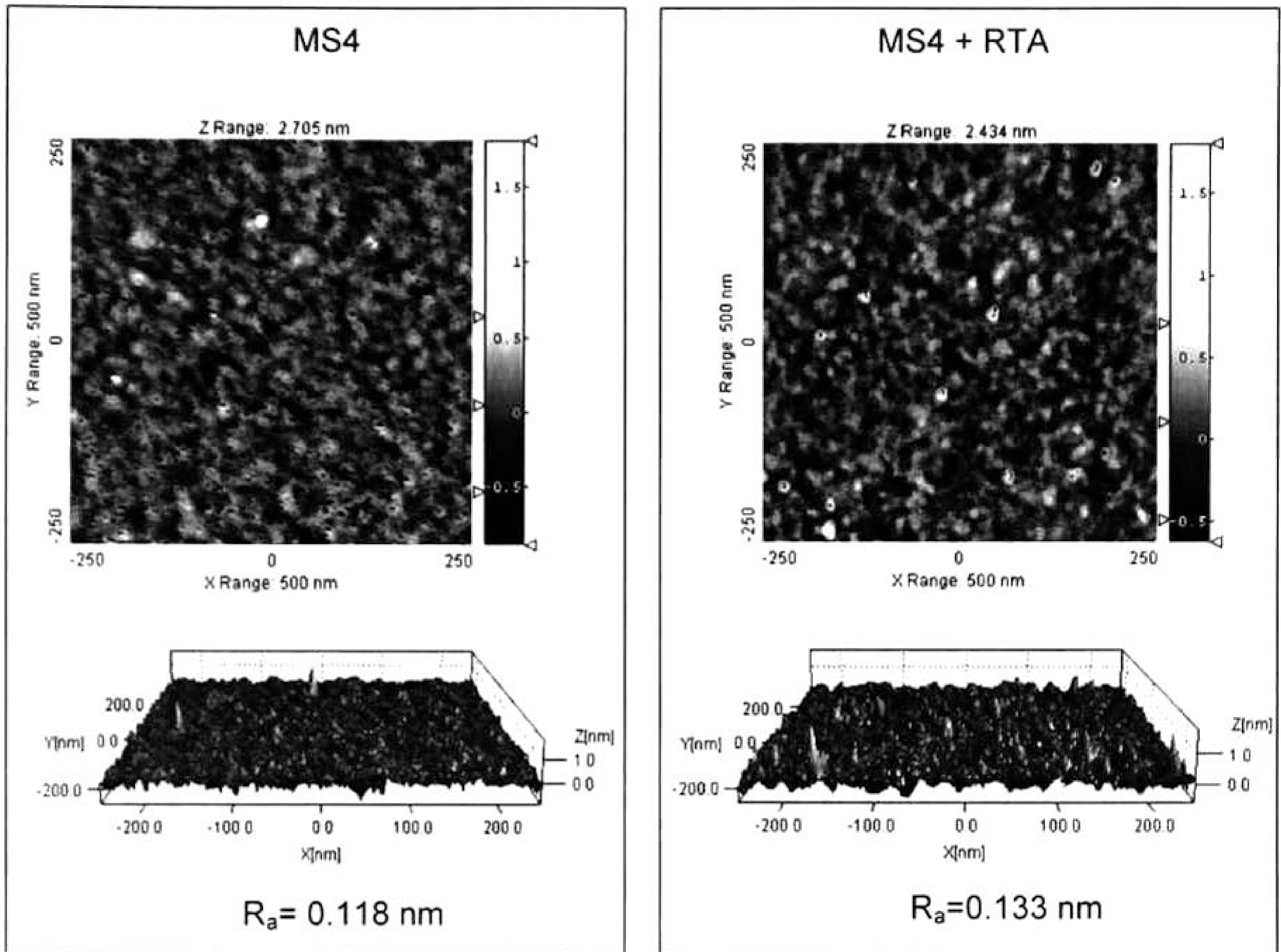

Figure 4.8 The topography images and therefore, the roughness average are very similar for both samples. Reducing the size scan to 500nm, the uniformity and quality achieved after the etching is conserved. The lines in each scan were the same, 512, and the rate corresponds to 0.734 and 0.655 Hz for the unannealed and annealed samples.

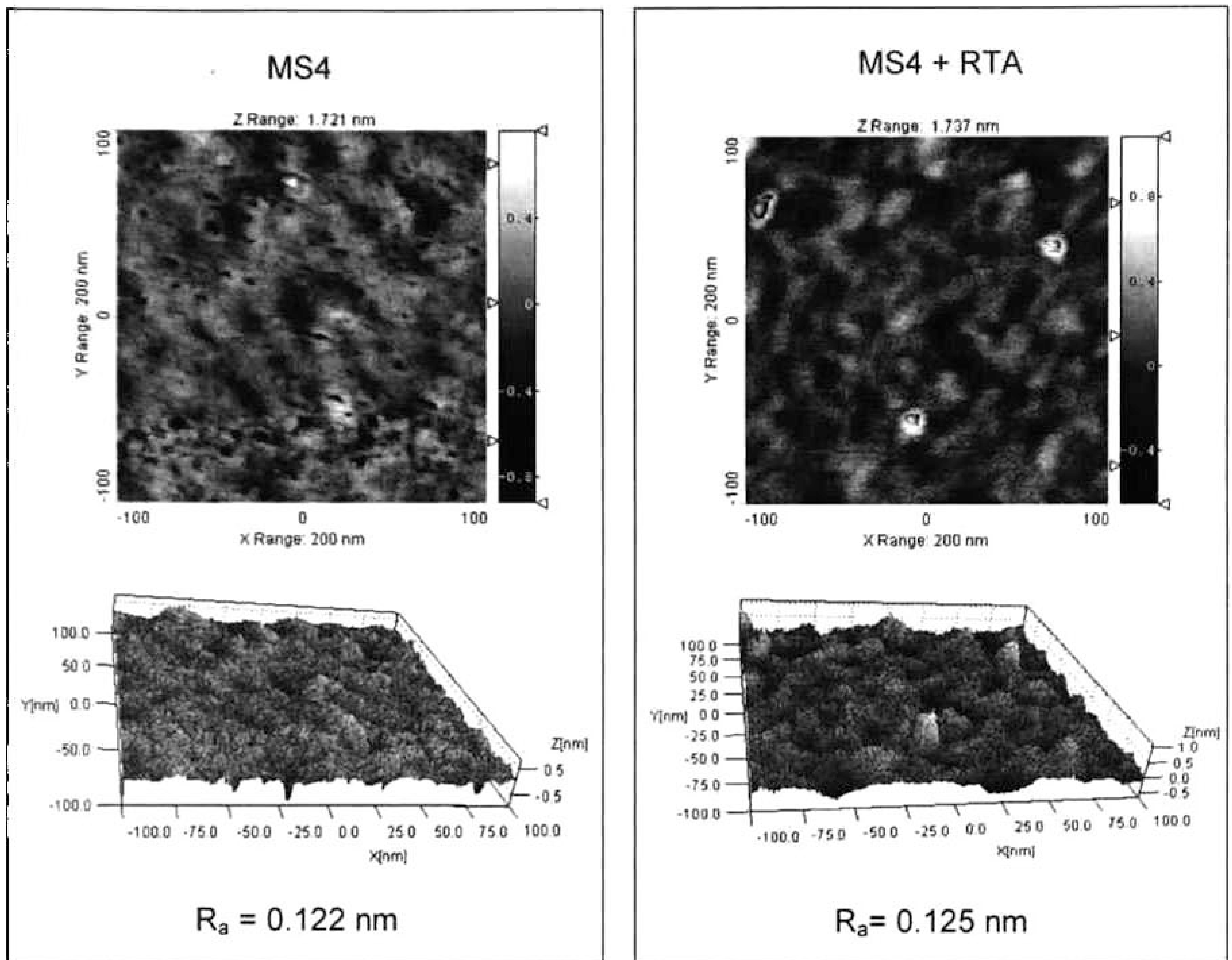

Figure 4.9 The smaller AFM scan size done was of 200 nm. The images revealed only few small features stick out from the flat surface, and a very flat surface. The roughness is according with the obtained in the others scans sizes. The lines and the rate for the unannealed sample were of 512 and 0.734, and for the RTA were of 640 and 0.656 Hz respectively.

Comparing the MS3 and MS4 images, is observed clearly, the chemical etching efficiency for the MS4 was better. The size of some clusters on the MS3 samples did not allowed getting good images. It is believed that these feature are particles due to their size and because they are not uniformly distributed on the surface.

In the other hand, annealed and unannealed MS4 surfaces are very flat and uniform. This is demonstrated by the roughness average (R_a) that was fund in the order of 1-2 Å. The quality in the chemical etching process control was sufficient for getting good data in ARXPS experiment.

4.3 XPS data

The Figure 4.10 and Figure 4.11 shows the XPS survey scans (pass energy of 50 eV) for the MS3 and MS4 samples respectively taken at 45° after heating in-situ (UHV) at 250°C for 15min. An *in-situ* anneal was performed on each sample previous to the XPS measurements to desorb the carbon contamination at the surface of the sample as well as hydroxides from the air exposure.

The survey scans did not show any appreciable difference. This is due to the low resolution mode (pass energy). With XPS at high resolution (pass energy of 15 eV) and more scans, regions for O 1s and C 1s are better identified. In the spectra of the Figure 4.12 are appreciated the differences between the samples before and after annealing *in-situ*.

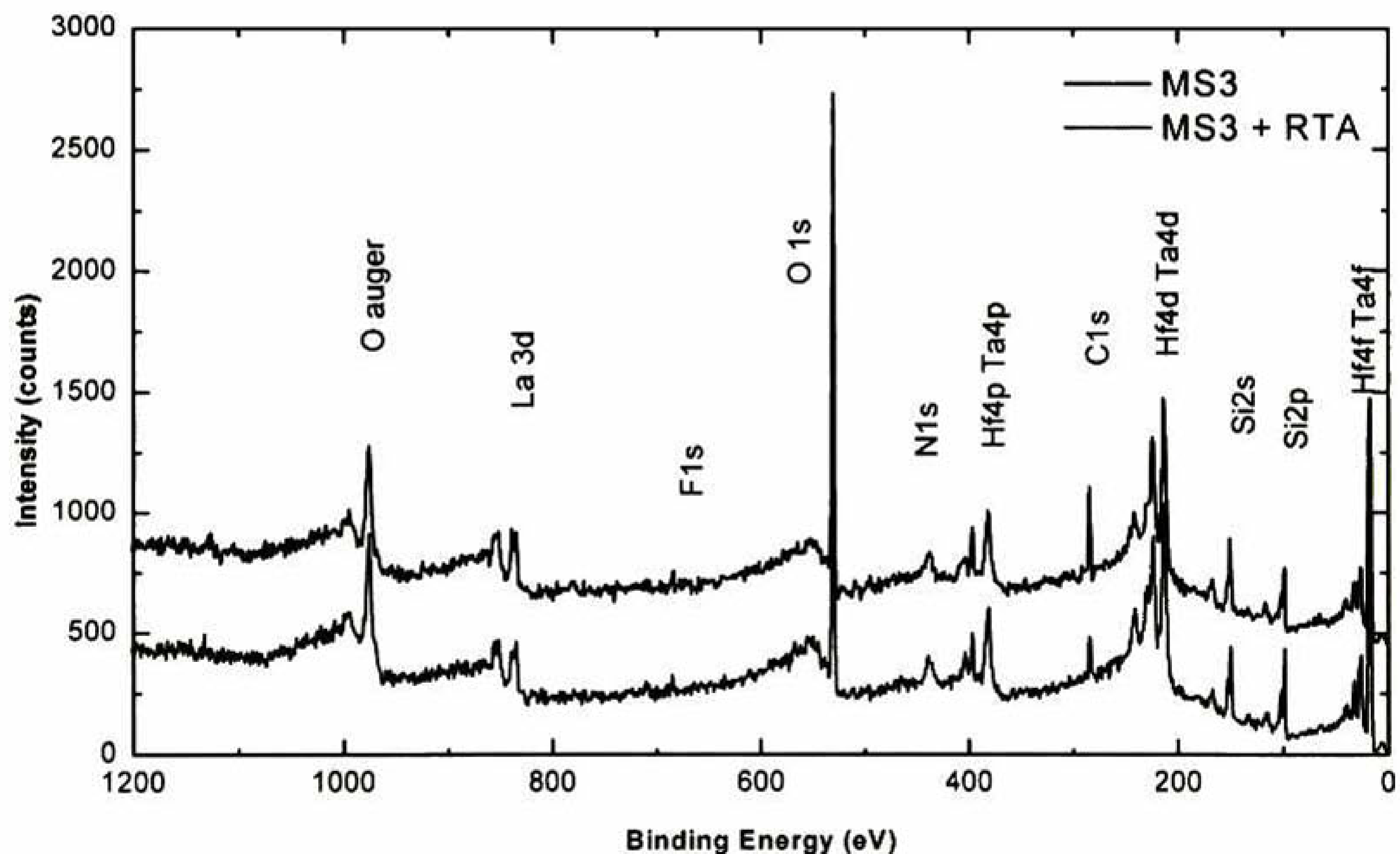

Figure 4.10 XPS survey scans for the MS3 sample with and without RTA. There were not apparent differences in this low resolution mode.

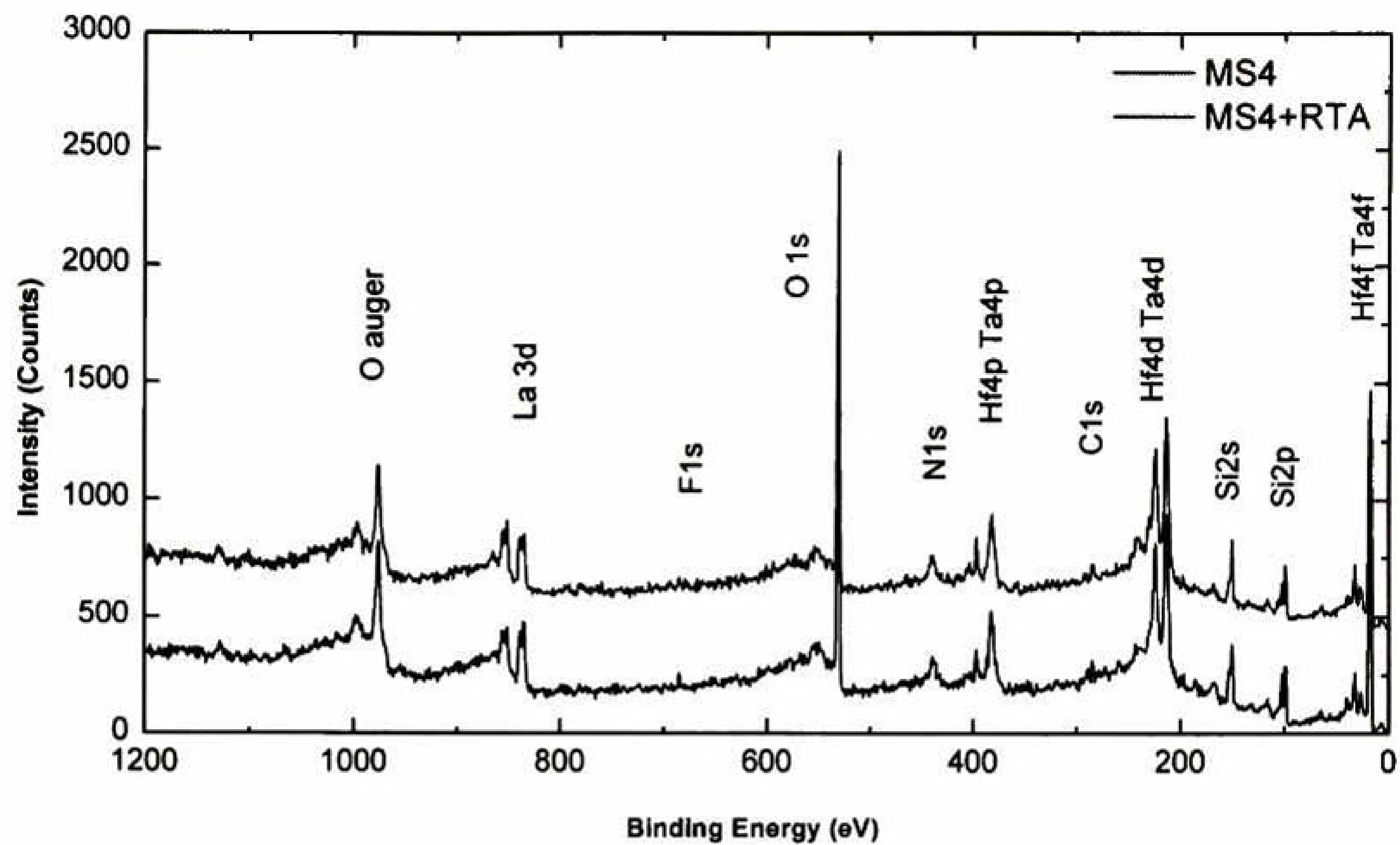

Figure 4.11 Survey scans for the MS4 sample with and without RTA. There were not apparent differences in this low resolution mode.

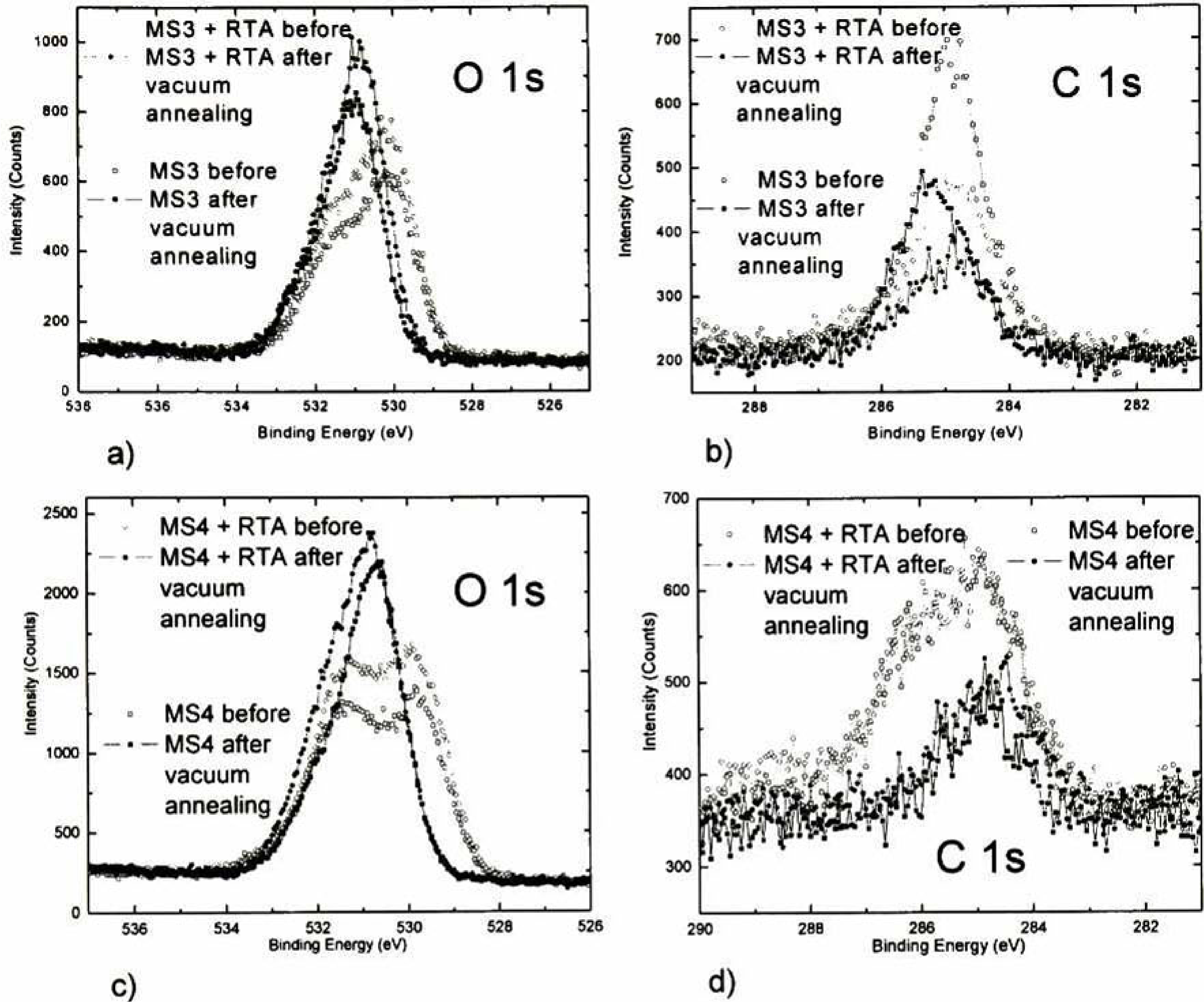

Figure 4.12 XPS spectra taken at 45° before and after annealing in-situ (250°C for 15 minutes). a) O 1s signal for MS3 sample; b) C 1s signal for MS3 sample; c) O 1s signal for MS4 sample; d) C 1s signal for MS4 sample. After heating, there was less signal of carbon and a component of oxygen was gone in both cases.

4.3.1 Photoelectron signals detected at different take-off angles

Only the MS4 sample was considered in this section because it showed better morphology. XPS at several take-off angles (ARXPS) was sensitive to detect a wide range of core level photoelectron signals. Those most intense and furthermore, outstanding were analyzed. The fit of the XPS peaks for all the angles was done simultaneously with the *AAnalyzer* software.[1] It is based in the de-convolution of each peak in two components: lorentizan and Gaussian functions. The parameters used for the fits are shown in the Table 4.3.

Table 4.3 Gaussian width, Lorentzian width, spin-orbit splitting, branching ratio, binding energy, and background employed in the data fitting with *AAnalyzer* The parameters shown are those employed for the MS4 sample.

	Si 2p bulk no RTA		Si 2p bulk RTA		Si 2p oxide no RTA	Si 2p oxide RTA
Splitting	-0.6095		-0.6095		-0.6095	-0.6095
Branching ratio	0.5		0.5		0.5	0.5
Gaussian width	0.467		0.492		1.803	1.584
Lorentzian width	0.085		0.085		0.085	0.085
Binding energy	99.7	99.389	99.83	99.399	102.33	102.57
Background	Integral					

	Hf 4f no RTA	Hf 4f RTA	Ta 4f no RTA	Ta 4f RTA
Splitting	-1.66		-1.92	
Branching ratio	0.75		0.75	
Gaussian width	1.189	1.202	1.226	1.217
Lorentzian width	0.1		0.1	
Binding energy	17.659	17.809	26.75	26.88
Background	Integral			

	La 3d no RTA	La 3d RTA	Plasmon no RTA	Plasmon RTA
Splitting	-16.865		1	
Branching ratio	0.666		1	
Gaussian width	1.928	1.879	5,818	5.483
Lorentzian width	0.1		0.1	
Binding energy	835.229	835.348	849.947	849.942
Background	Integral slope			

	Quasi-particle no RTA	Quasi-particle RTA	Quasi-particle no RTA	Quasi-particle RTA
Splitting	-16.865		-16.865	
Branching ratio	0.666		0.666	
Gaussian width	1.928	1.879	2.313	2.435
Lorentzian width	0.1		0.1	
Binding energy	837.234	837.2	839.491	839.545
Background	Integral slope			

	La 4d no RTA	La 4d RTA	La 4d no RTA	La 4d RTA
Splitting	-2.93 [a]		-2.93 [a]	
Branching ratio	0.666		0.666	
Gaussian width	2.048	2.275	2.048	2.275
Lorentzian width	0.05		0.05	
Binding energy	103.26	103.28	107.518	107.538
Background	Integral			

(a) Found it in reference 2.

	O 1s in SiO_2 no RTA	O 1s in SiO_2 RTA	O 1s in HfO_2 no RTA	O 1s in HfO_2 RTA
Splitting	1		1	
Branching ratio	1		1	
Gaussian width	1.494	1.568	1.287	1.331
Lorentzian width	0.25		0.25	
Binding energy	532.113	532.081	530.916	530.984
Background	Integral slope			

	N 1s no RTA	N 1s RTA	F 1s no RTA	F 1s RTA
Splitting	1		1	
Branching ratio	1		1	
Gaussian width	1.947	1.875	1.956	2.185
Lorentzian width	0.05		0.1	
Binding energy	397.17	397.54	685.239	685.357
Background	First order			

	C 1s no RTA	C 1s RTA	C 1s no RTA	C 1s RTA
Splitting	1		1	
Branching ratio	1		1	
Gaussian width	1.244	1.247	1.244	1.247
Lorentzian width	0.35		0.35	
Binding energy	285.05	284.98	286.26	286.15
Background	Integral			

The branching ratio employed were the theoretical values (1/2 for p orbitals, 2/3 for d orbitals, and 3/4 for the f orbitals). The rest of the values (the mayority) were fit from the program

Figure 4.13 shows the Si 2p region which is formed of bulk and silicon oxide components. The bulk peak intensity increases with the angle more pronounced than the oxide peak intensity. This means that Si 2p electrons from bulk come from deeper regions of the film than the signal from silicon oxide. Binding energy for the La4d is close to that of Si 2p in silicon oxide as it shown in the Figure 4.13 where only is presented the fit for the sample unannealed (MS4). The annealed sample was fitted with the same number and type of peaks.

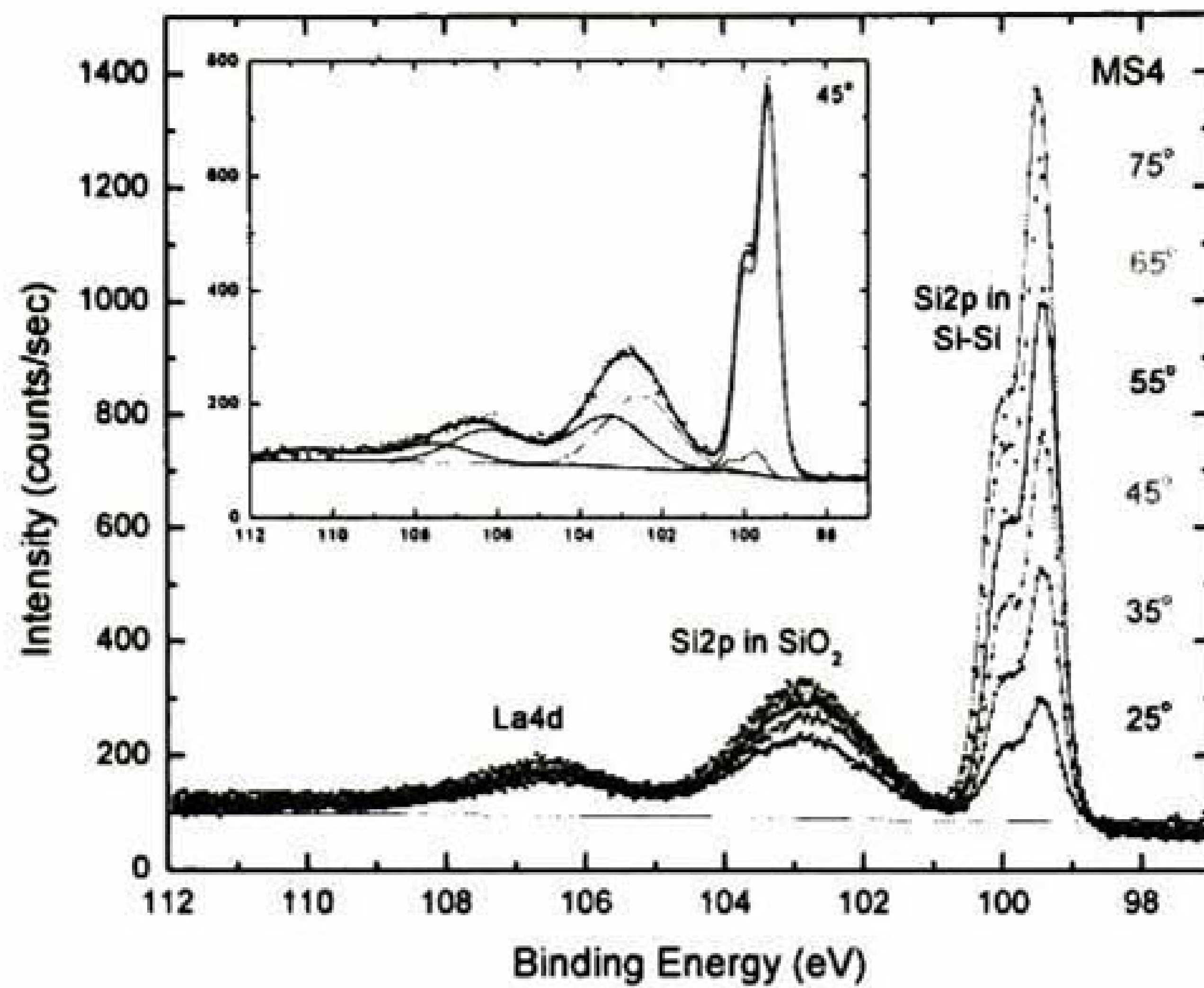

Figure 4.13 Fits of the Si 2p and La 4d regions. The binding energies of Si 2p in silicon oxide and La4d photoelectrons overlap. The Si 2p electrons are detected from deeper regions in the film (the peak area increase with the angle is more pronounced).

The La 3d feature is composed by one chemical states (La^{3+}) and other satellites (plasmon and quasi-particle states).[2] These features are shown in Figure 4.14. The peak areas have a clear dependence with the angle.

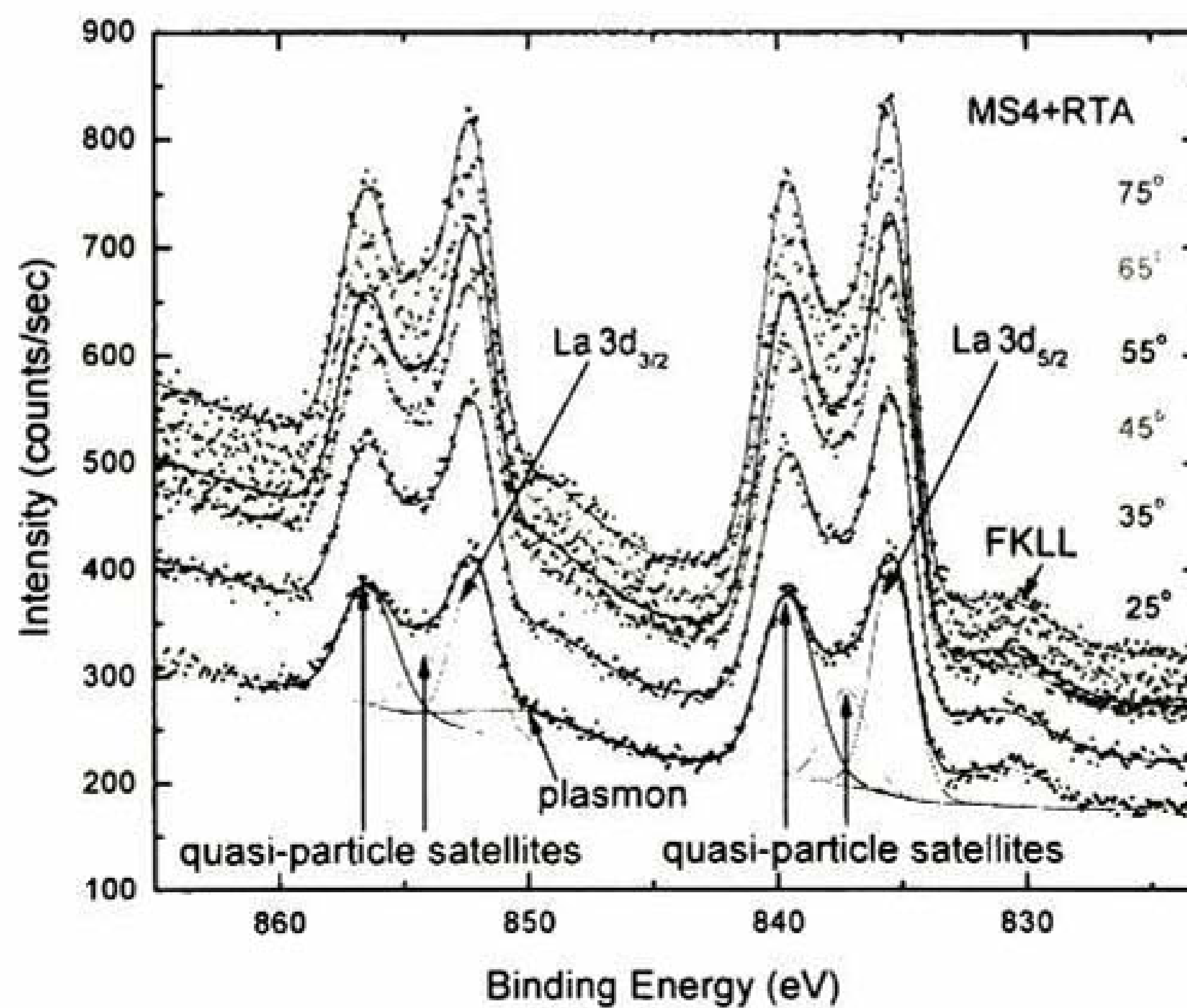

Figure 4.14 La 3d feature of the RTA sample. The spectra were fit according to the literature with four doublets corresponding to on oxidation state (La^{3+}) and another satellites.

Figure 4.15 shows two chemical states well defined for the O 1s for both samples corresponding to Hf-O-Hf bond and Si-O-Si bond. Also, it can be seen the peak area of oxygen in silicon oxide in the sample exposed to RTA is larger than in the unannealed sample. The increasing of oxygen with the angle indicates that the oxygen is distributed through the film until deeper regions.

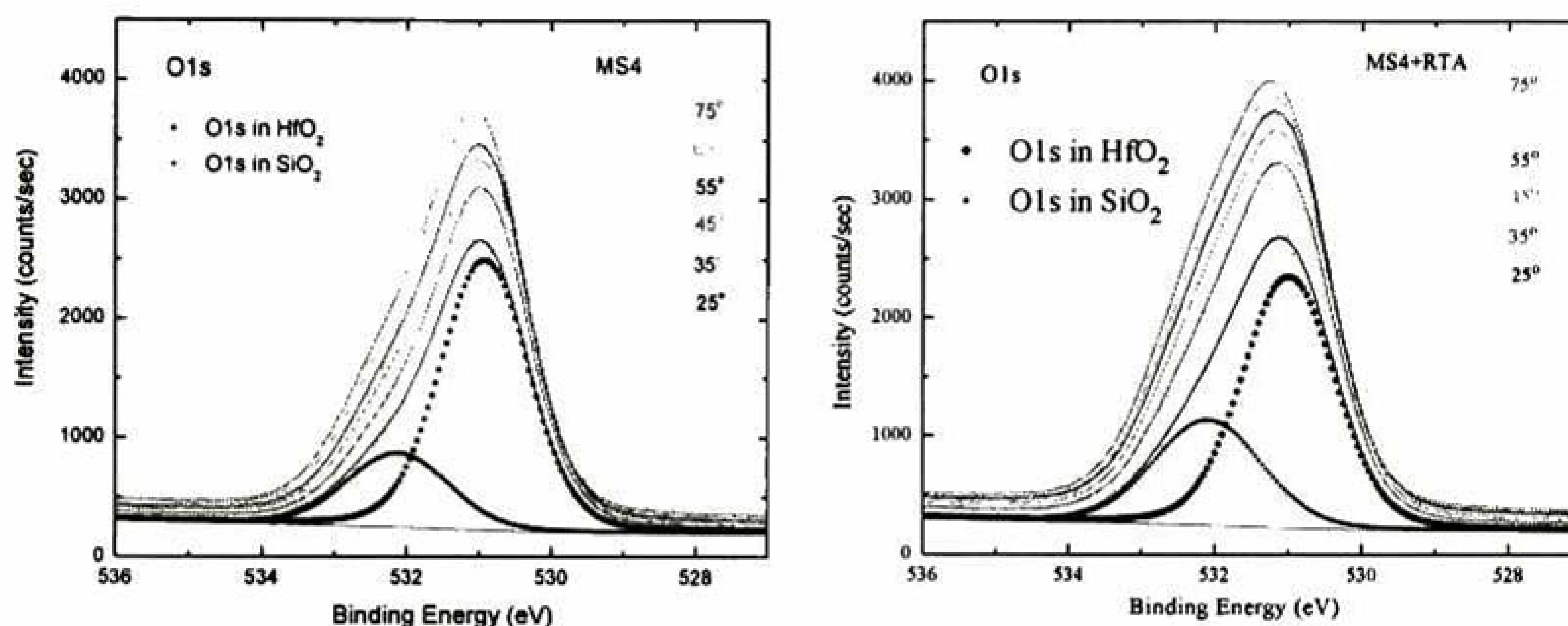

Figure 4.15 O 1s has two chemical states corresponding to Hf-O-Hf and Si-O-Si bonds. The peak area of oxygen in silicon oxide in the RTA sample is larger than in the unannealed sample.

XPS data for Hf 4f is shown in Figure 4.16. The peak areas from 35° to 75° similar, while at 25° it decreases. The fit shows only one chemical state attributed to hafnium oxide (17.7 eV).[3]

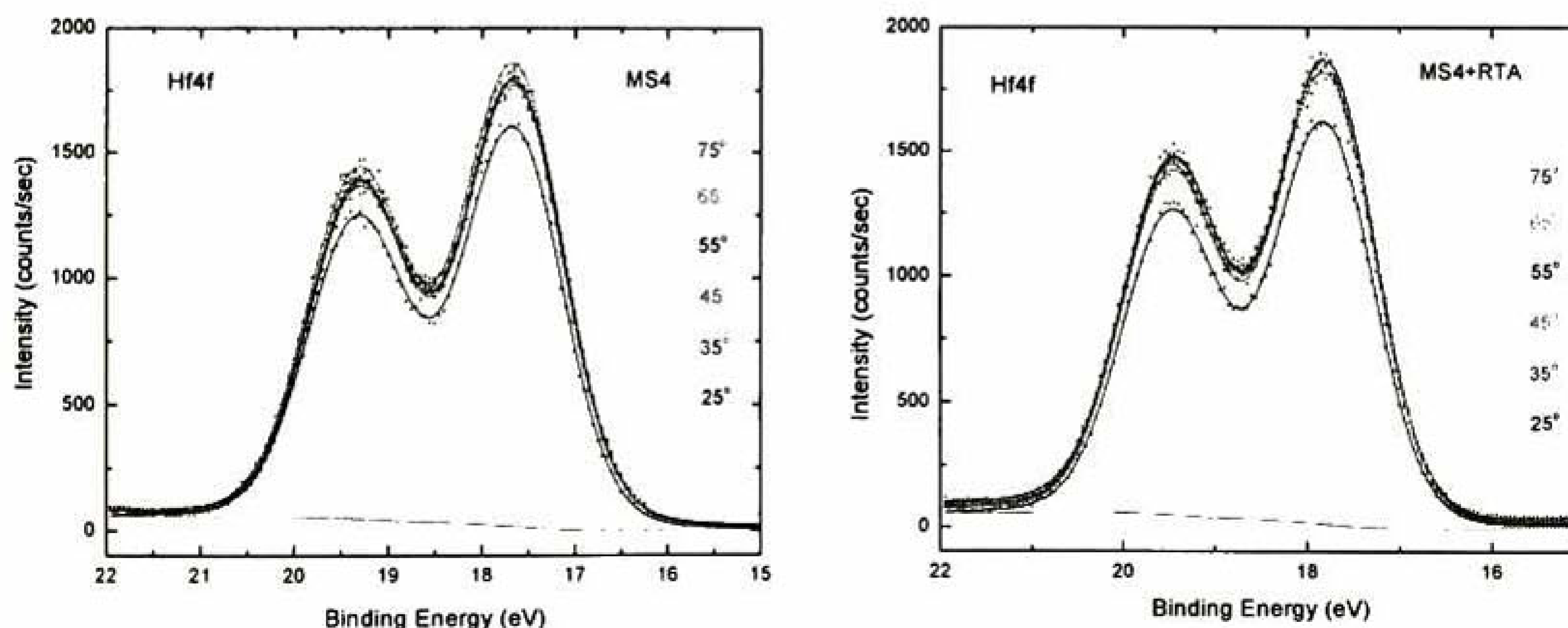

Figure 4.16 Good XPS data is presented for Hf 4f. The fit was done with only one peak centered in the binding energy of hafnium oxide.

The XPS region in Figure 4.17 shows two peaks very close, Ta $4p_{3/2}$ and N 1s. Only the area of N 1s was taken into account for the ARXPS analysis. Nitrogen could be fit with only one peak in both cases.

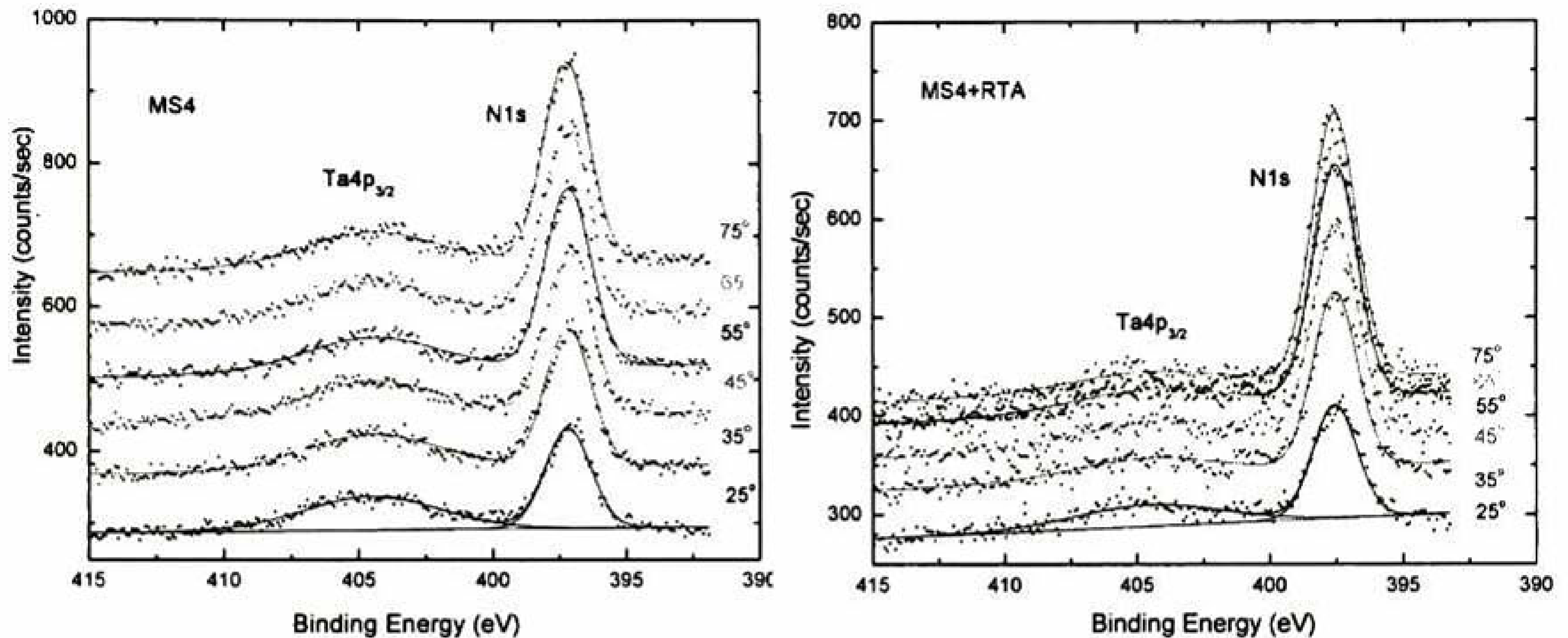

Figure 4.17 There is evidence of one nitrogen chemical specie only, before and after annealing.

After the chemical etching of Ta N, a little amount of tantalum remained on the surface in both samples. Ta 4f is shown in Figure 4.18. There is no dependence of the area with the angle (tantalum is present at or near of the surface of the sample); the amount of tantalum is the same for each angle in both samples. All the tantalum appears to be oxidized (binding energy of 26.8 eV)[3].

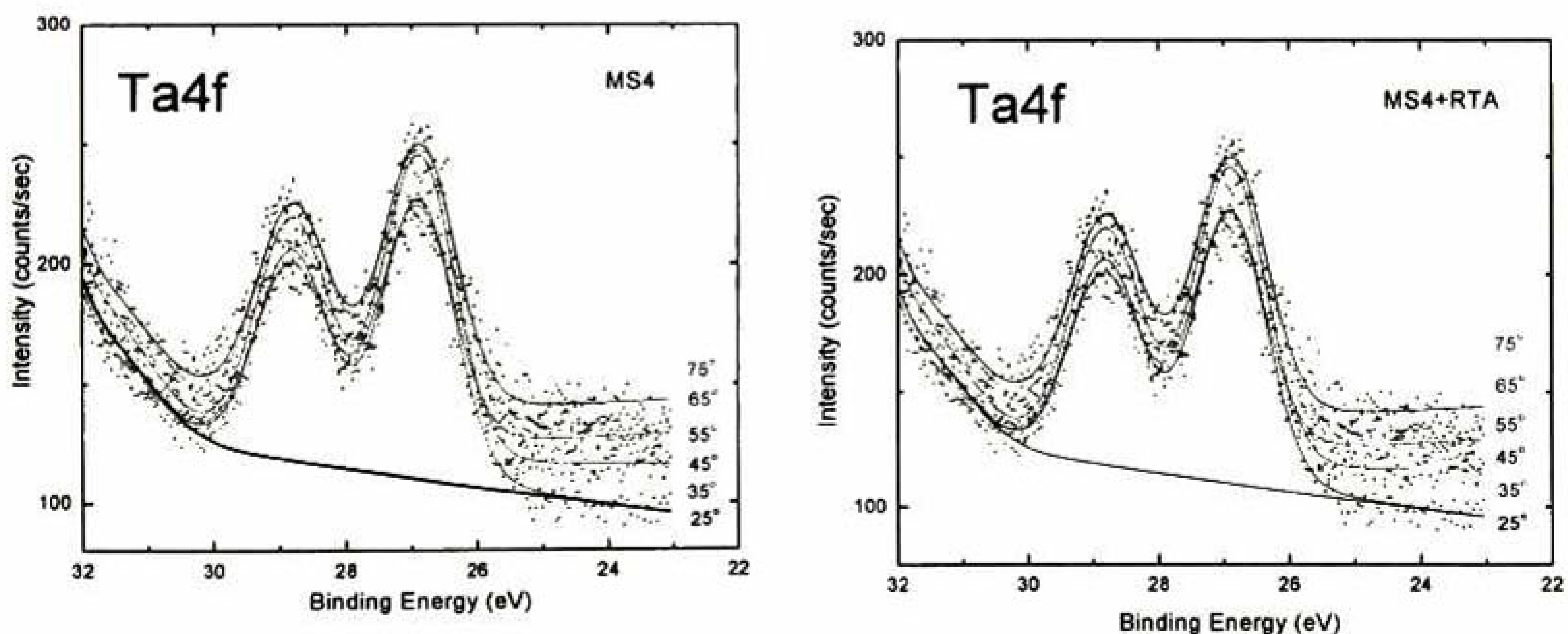

Figure 4.18 After the chemical etching of Ta N, a little amount of tantalum remained on the surface in both samples. The tantalum appeared to be oxidized.

Carbon contamination from the environment was detected. C-C and C-H bonds were found once the fit was done as shown in Figure 4.19.

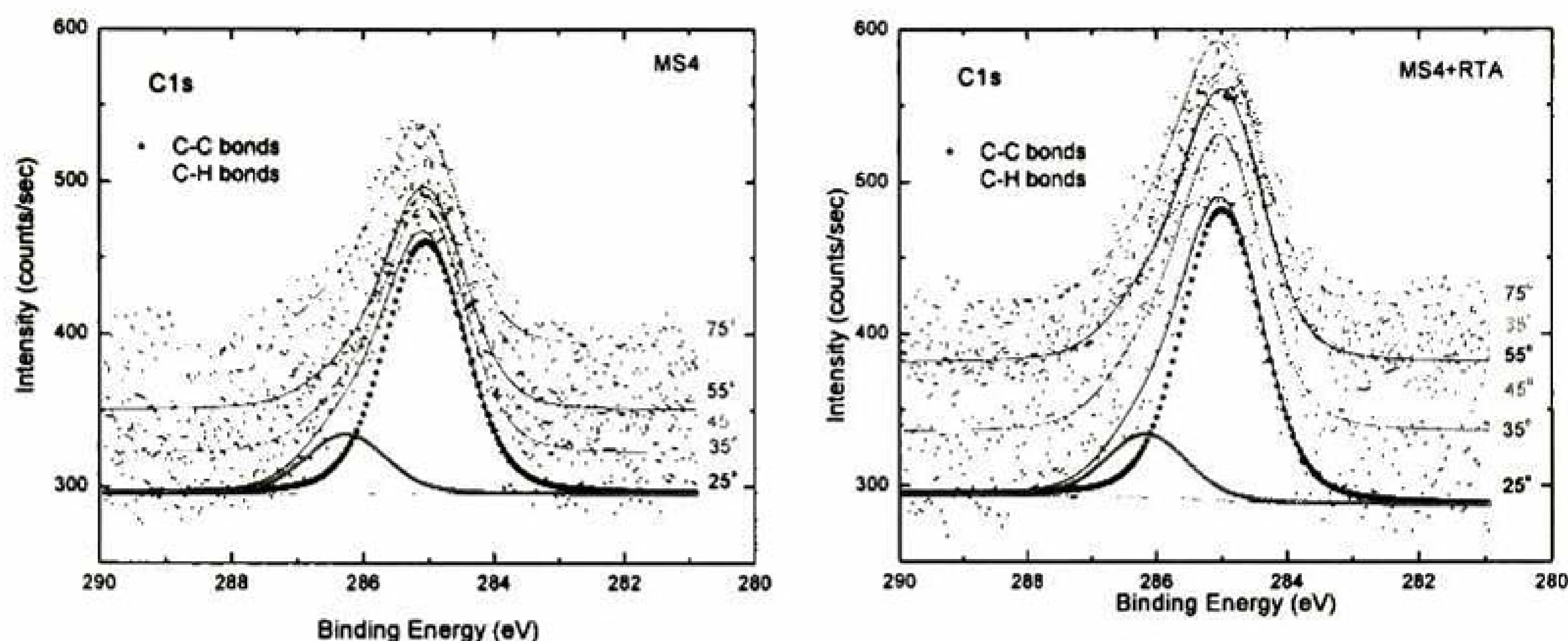

Figure 4.19 The presence of contamination at the surface of the samples is due to the exposure of samples to air previous to its introduction in the XPS system.

Also, the samples were contaminated (very small amount) with fluorine from the chemical etching process which was detected in XPS (see Figure 4.20).

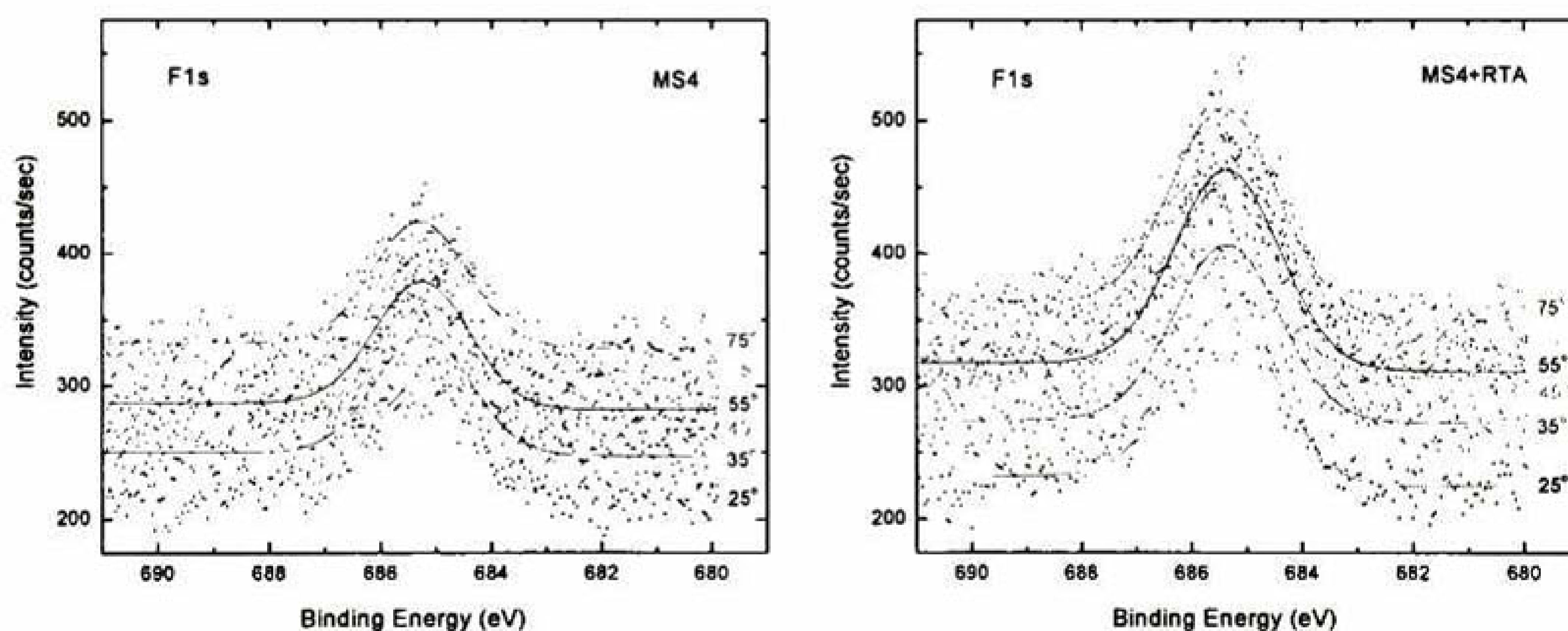

Figure 4.20 Fluorine contamination was detected in a very small amount. As discussed below, most of it was located at the surface.

4.4 FTIR study

The following figure (Figure 4.21) shows the spectra taken for the samples MS3+RTA, MS4, and MS4+RTA. FTIR experiments were done in the Attenuated Total Reflection (ATR) mode. The number of scans were 32 with a resolution of 4 cm^{-1}.

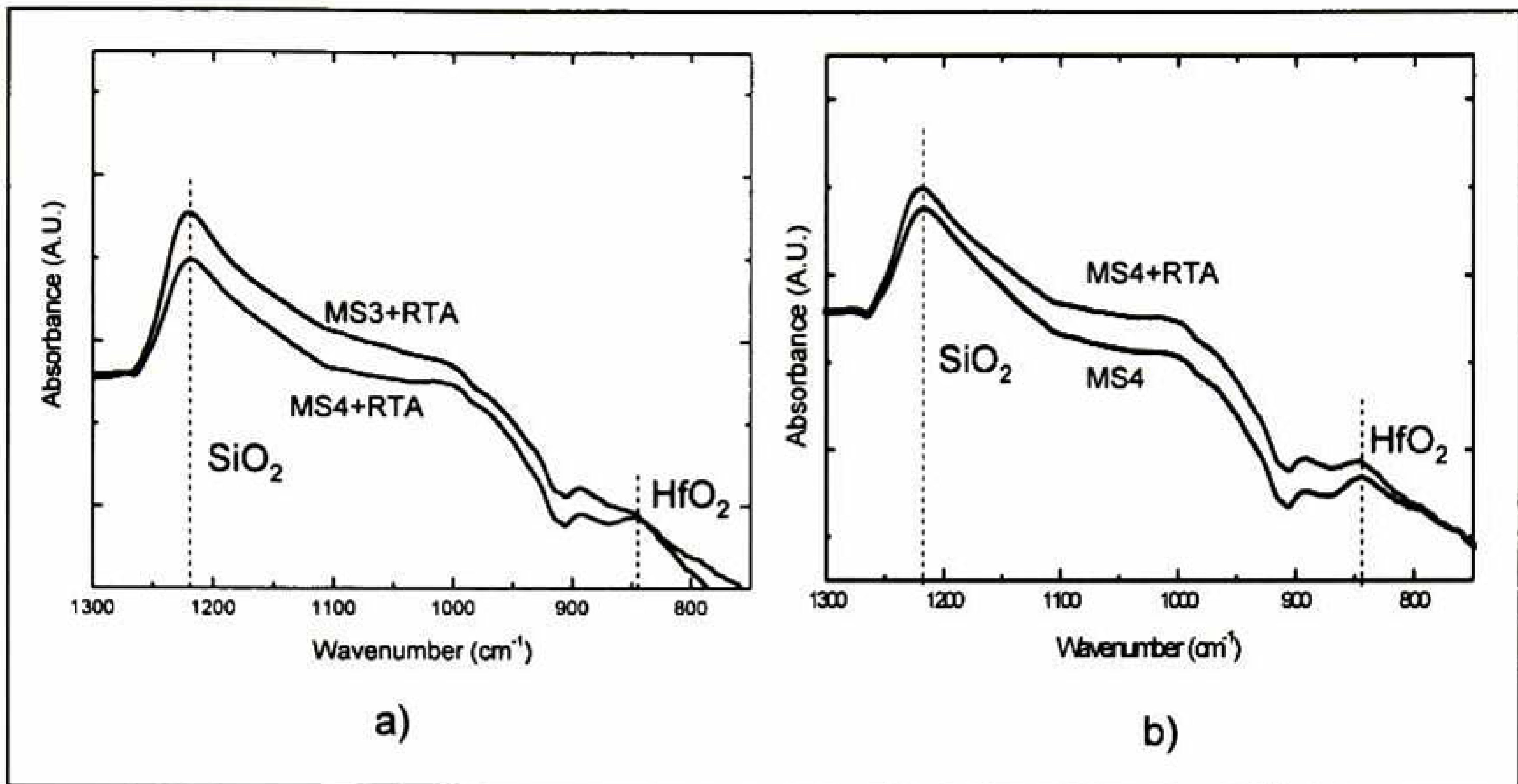

Figure 4.21 FTIR spectrum taken for the samples. (a) MS3 and MS4 annealed samples; (b) MS4 annealed and unannealed samples. The Si-O-Si vibration (LO phonon mode) appears at 1220 cm^{-1} The peak observed close to 900 cm^{-1} is produced by the Si substrate. The feature at 850cm-1 corresponds to O-Hf-O. The treated MS3 sample showed a larger O-Si-O and a lower O-Hf-O signal than the treated MS4 sample. The MS4 sample showed a larger O-Si-O and lower O-Hf-O signal after RTA.

Figure 4.21 shows the O-Si-O bonds at 1220cm^{-1}, which it is reported in the literature[4] at 1240 cm^{-1}. The O-Hf-O mode is visible, while the Si-O-Hf is not.

References

[1] Alberto Herrera-Gómez. "AAnalyzer: Un Programa de Análisis para Espectros de Infrarrojo y de Fotoemisión" Reporte Interno, Julio de 1998 LIM-CINVESTAV (Registro S.E.P. Número 03-1999-051710412300, diciembre de 1999, México).

[2] D.F. Mullica, H.O. Perkins, C.K.C. Look, and V. Young. The X-ray photoemission spectra of La $(OH)_3$. Journal of Electron Spectroscopy and Related Phenomena. Vol 61, pp. 337-355, (1993).

[3] B. V. Crist. Fundamental XPS Data from Pure Elements, Pure Oxides, and Chemical Compounds. XPS International LLC, (2007)

[4] M.A. Quevedo-Lopez, J.J. Chambers, M.R. Visokay, A. Shanware, and L. Colombo. Thermal stability of hafnium-silicate and plasma-nitrided hafnium silicate films studied by Fourier transform infrared spectroscopy. Applied Physics Letters, Vol. 87, No. 012902, pp.1-3, (2005).

Chapter 5. Analysis and discussion of La_2O_3/HfO_2 structures

5.1 Angular dependence of XPS peak areas

The Figure 5.1 and Figure 5.2 show the angular dependence of the area of the photoelectron peaks in the sample MS4 for the cations and anions, respectively. The overall behavior of all the peak areas was similar before and after RTA, suggesting that the structure was stable. The large slope for the La 3d peak area indicates that La is distributed deep in the film and not at the surface, as it was originally grown. In contrast, the flat behavior for Ta 4f suggests that it remained at the surface. As expected, the bulk Si 2p peak showed a larger slope than the Si 2p from silicon oxide.

In the case of the anions, the photoelectron peak of O 1s showed two chemical species well identified (see Figure 4.15). The peaks area attributed to SiO_2 showed a larger slope than that in HfO_2. .Also, it can be appreciated in the Figure 5.2, the angular dependence for nitrogen exhibits a similar behavior before and after RTA. The slope of the lines in both scenarios suggests that nitrogen was distributed deep in the film, and that carbon contamination was present at the surface.

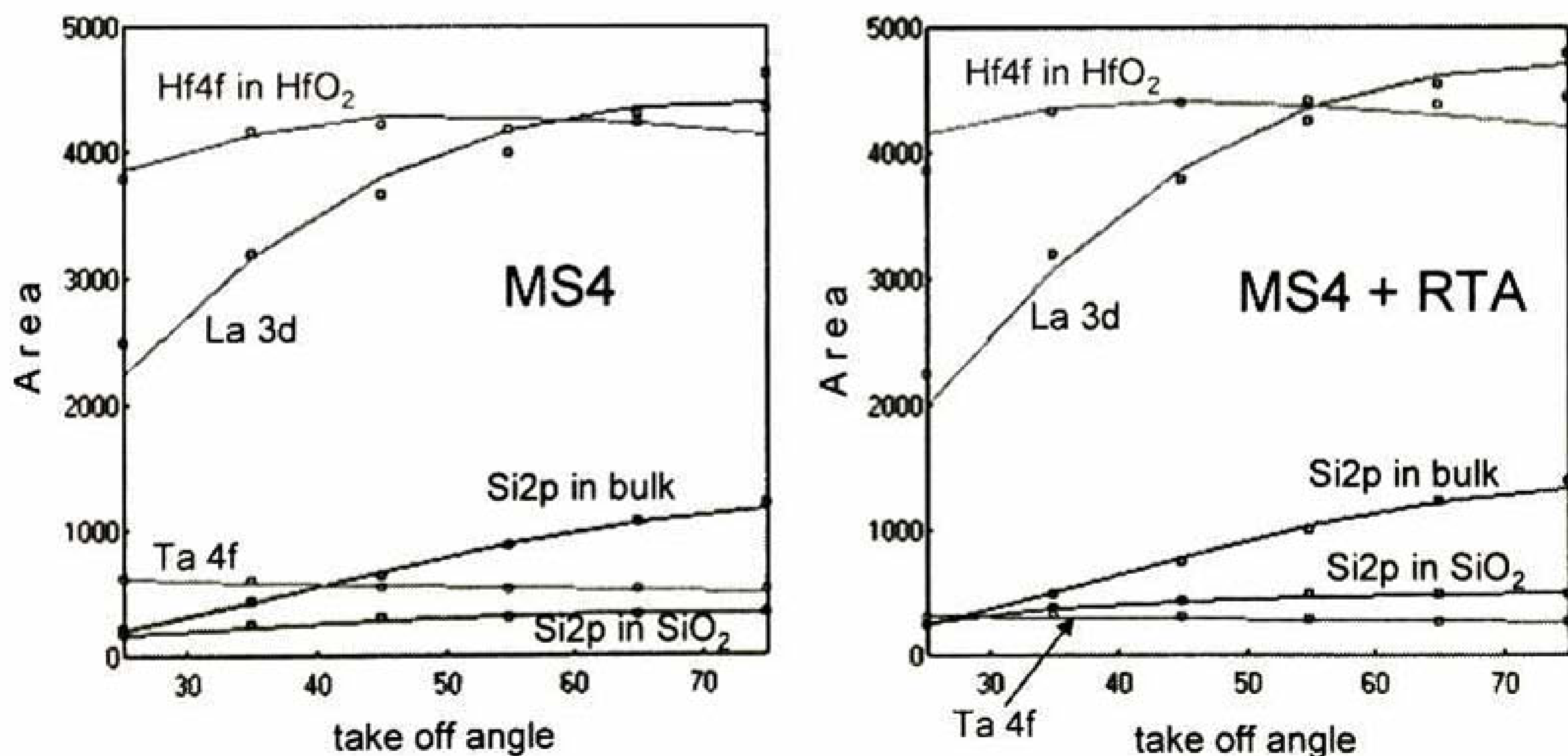

Figure 5.1 The signal from La 3d showed a strong dependence on the angle indicating a deep distribution. In contrast, the Ta 4f data showed that this chemical specie was located at the surface whereas Hf 4f was distributed near of the surface and it was kept there upon RTA.

It can be seen that the Lanthanum exhibits a deep distribution.

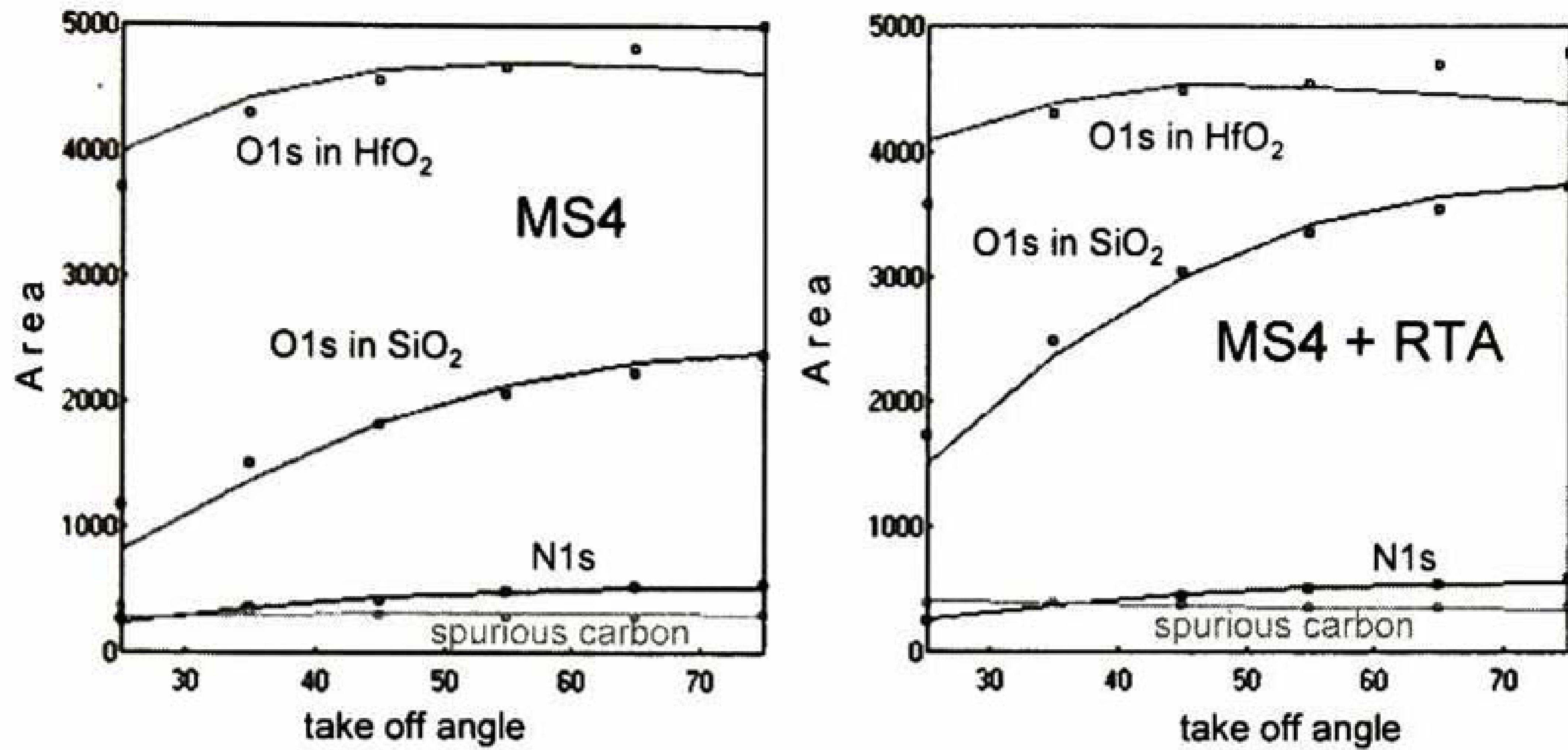

Figure 5.2 The angular dependence of the peak area of anions was closely reproduced (with the exception of O 1s in HfO_2) employing the layered model. The two chemical species of oxygen were attributed to the SiO_2 and the HfO_2 layers. The peak area attributed to SiO_2 showed a larger slope than that in HfO_2. .Also, it can be appreciated in the Figure 5.2, the angular dependence for nitrogen exhibits a similar behavior before and after RTA. The slope lines suggest nitrogen is distributed deep in the film

5.2 Quantitative analysis

The angular dependence of the peak area presented in the last section was theoretically reproduced.[1] It was necessary to propose a model that was based on previous knowledge. TEM studies on similar systems show the presence of well defined and conformal layers. The model proposed consisted on a layer of hafnium oxide on top of a layer of silicon oxide on top of the substrate Si (001).

5.2.1 Parameters employed in the calculations

The theoretical prediction of the angular dependence implied the previous knowledge of the geometrical parameters of the XPS tool. The parameters of the XPS tool employed in this study are shown in Table 5.1. The calculations also required the previous knowledge of:

- the photoemission cross section for each core level employed (see Table 5.2), parameters that were obtained from the literature, and

- the effective attenuation length of photoelectrons for the different materials (see Table 5.3) constituting the film.

Table 5.1 Set of parameters obtained in the characterization of the XPS equipment. A previous carefully characterization of the XPS system was carried out.

manipulator parameters		electron analyzer parameters		beam parameters	
z0	0	coneAngle	9	coneAngle	9
yRot	0	acceptance	16	gauss ver	0.438837
zRot	0	gauss ver	0.434738	gauss hor	1.95336
sample height	0	gauss hor	0.380462	shoulder dist	0.952281
X-edge	-3.15302	second magnification		gauss ver 2nd	1.59321
Y-edge	-18.1195	acceptance	8	gauss Hor 2nd	1.95336
MY-edge	-0.055725	gauss ver	2.15574	intensity	0.620269
		gauss hor	1.95336		
		deviation in Z	-0.617531		
		deviation in X	-0.207184		

Table 5.2 The kinetic energies[2] and cross sections[3] of the photoelectrons employed in the calculations were found in the literature.

element	kinetic energy	PE cross section
Si2p	1387	0.011
Si2p	1387	0.011
La3d	651	0.6559
La4d	1384	0.089
Hf4f	1469	0.1108
Hf4p	1106	0.099
Ta4f	1460	0.1274
N1s	1090	0.024
C1s	1201	0.013
F1s	801	0.06
O1s	955	0.04

Table 5.3 Effective Attenuation Length values were calculated using the NIST Electron Effective Attenuation Length Database. Lattice constant of the layers and bulk were calculated too

parameters and plots | parameters for the chemical species | more parameters for the chemical species | layers 0 1 & 2 | layers 3 4 & 5 | data in block | stoichimetry | editor | miscelaneous |

	layer 0		layer 1		layer 2	
vertical lattice const	3.4		3.3		2.2	
horizontal lattice const	3.4		3.3		2.2	
Chemical Component	escape depth value	correlation	escape depth value	correlation	escape depth value	correlation
Si2p	36	none	17.95	LED00*LED15	33.37	LED00*LED25
O1s	26	15.282*LED05	12.78	0.623*LED05	24.38	LED01*LED05
N1s	29.11	none	14.2	LED02*LED15	27.16	LED02*LED25
Hf4f	37.81	none	18.4	LED03*LED15	34.97	LED03*LED25
C1s	31.62	none	15.37	LED04*LED15	29.51	LED04*LED26
F1s	22.4	none	11.15	LED0	21.09	0.58532
La3d	19.93	none	9.68	none	17.89	none
La4d	18.89	none	9.68	none	17.89	none
Ta4f	37.61	none	18.31	none	34.9	none
Ta4p	37.61	none	18.31	none	34.9	none
Hf4p	37.81	none	18.4	none	34.97	none
Au3d	26	none	26	none	26	none
Gd4d	26	none	26	none	26	none
Au4d	26	none	26	none	26	none
none	26	none	26	none	26	none
none	26	none	26	none	26	none
none	26	none	26	none	26	none
none	26	none	26	none	26	none
use values for	SiO2		HfO2		C	
Shallow End	8.415	LDE1	0.99	LDE2	0	LDE2
Deep End	23.715	LSE0+LLC0*4.5	8.415	LSE1+LLC1*2.2	0.98	LSE2+LLC2*0.4

Get Layers | Save Layers

some bulk parameters
bulk vertical lattice const 1.357
bulk horizontal lattice const 3.84
bulk PE efficiency (y) 0.905

saveLayersNewWayButton | getLayersNewWayButton

The Effective Attenuation Length of Table 5.3 was obtained from the NIST Electron Effective Attenuation Length Database employing the assymetry parameters shown in Table 5.4 and Table 5.5. These two set of parameters were also obtained from the same NIST database.

Table 5.4 Core level assimetry parameters employed in the calculation of the effective attenuation lengths with the software provided by NIST.[4]

Peak	Assimetry parameter (β)
Si 2p	1.03
O 1s	2
N1s	2
Hf 4f	1.06
C 1s	2
F 1s	2
La 3d	1.1
Ta 4f	1.06

Table 5.5 Layer parameters employed in the calculation of the effective attenuation lengths with the software provided by NIST.[4]

Material	Gap (eV)	Valence electrons	Density (g/cm3)
Si	1.1	4	2.3
SiO_2	9	16	2.2
HfO_2	6	16	9.8

5.2.2 Determination of the thickness of the layers

The lines in the Figure 5.1 represent the theoretical prediction of the angular dependence of the cations constituting the film. As expected, the data was consistent with oxidized silicon below the hafnium layer. The thicknesses of the layers were forced to reproduce the density of the bulk silicon oxide and hafnium oxide, respectively. The consistency to the density was preferred due to the improvement of the fit. As it can be observed in Figure 5.1, the fit for Hf could have been improved by considering a thicker Hf layer. However, a thicker film would not be consistent with the known density of hafnium oxide. The C 1s ARXPS fits shows that carbon is spatially distributed at the surface of the sample (See Fig. 5.2). Less than one monolayer was determined for carbon (0.5ML). The resulting thicknesses, considering only the fits for the ARXPS data for cations, are shown in Figure 5.3.

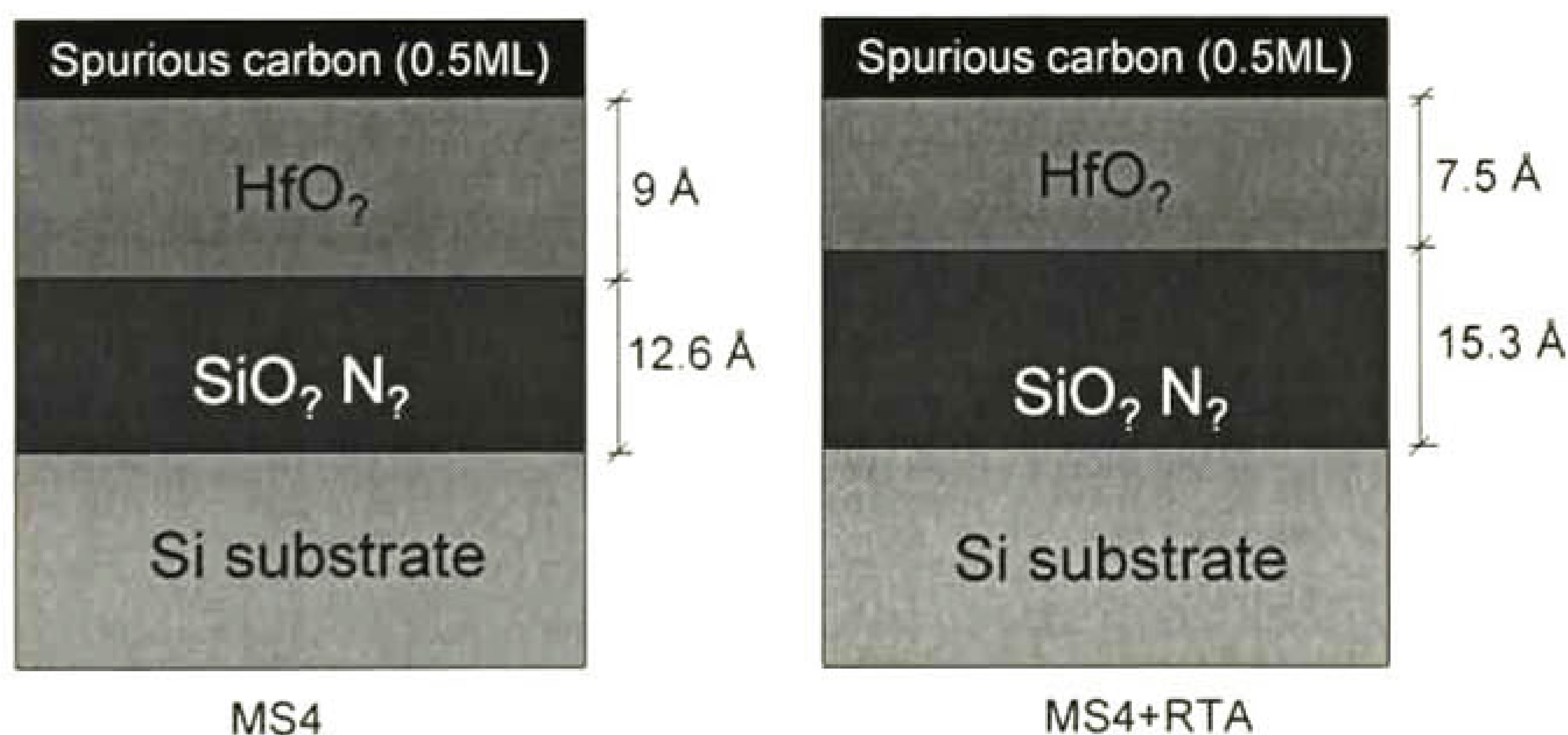

Figure 5.3 Thickness of the films determined by forcing the density of the films to the known bulk values. The comparison between the experimental data and the values obtained from fits employing this structure is shown in Figure 5.1. The question mark in the stoichiometry coefficients of the anions indicates that the amount of oxygen and nitrogen was not employed in the determination of the thickness.

It was possible to assess the density of each layer from the photoemission data because the signal from the silicon bulk peak could be related to the density of the

substrate, which is known. For this reason, it is paramount to count with the photoemission signal from the substrate.

5.2.3 Determination of the stoichiometry of the layers

The physical location (obtained from its angular dependence) of the oxygen peak labeled "O 1s in HfO_2" in Figure 5.2b, approximately coincided with that for the hafnium peak shown in Figure 5.1b (so the label), suggesting the formation of a hafnium oxide. In addition, the binding energy of that peak (531 eV) is consistent with oxygen in hafnium oxide. Then, the physical location of oxygen was consistent with its chemical shift in HfO_2. The amount of that oxygen specie was calculated by considering that its spatial distribution was the same as that for Hf. The stoichiometry of that layer could then be calculated, obtaining $HfO_{1.9}$. Similar results for the rest of the layers for the unannealed and RTA sample are shown in Figure 5.4.

It was very fortunately that the angular dependence of the peak area of anions was closely reproduced forcing the spatial distribution of each oxygen and nitrogen specie to the corresponding layer. Likewise, the fits could have been improved by changing the anion spacing, but the distribution would not exactly coincide with the distribution of the cation. The consistency of the compound was preferred over the quality of the fit. However, the experimental data was closely reproduced.

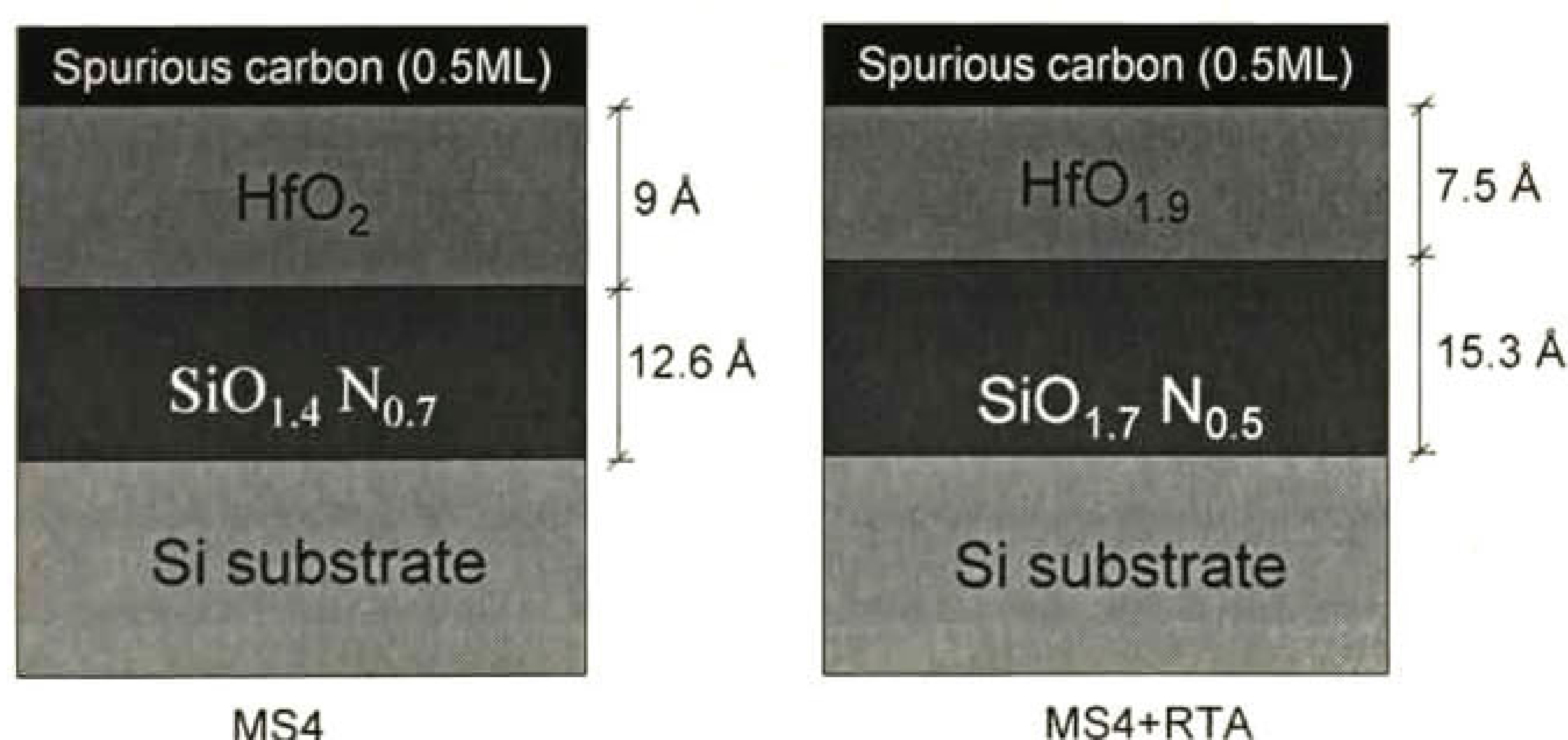

Figure 5.4 Resulting stoichiometry for the SiO_2 and HfO_2 layers. The angular dependence of the peak area of anions was closely reproduced forcing the spatial distribution of each oxygen and nitrogen specie to the corresponding layer. The consistency of the compound was preferred over the quality of the fit. However, the experimental data was closely reproduced

5.3 The lanthanum distribution

Once the location of the films and the physical distribution of the compound were known, the Lanthanum distribution can be determined.

5.3.1 The La in the RTA sample

Figure 5.5 shows various scenarios proposed for the distribution of La in the RTA sample. It is very clear that only one of the scenarios considered was consistent with the data. The error bars from the ARXPS data fits was around of 3% for each take off angle. The important conclusion is that the La is located at the SiO_2/HfO_2 interface for the RTA sample.

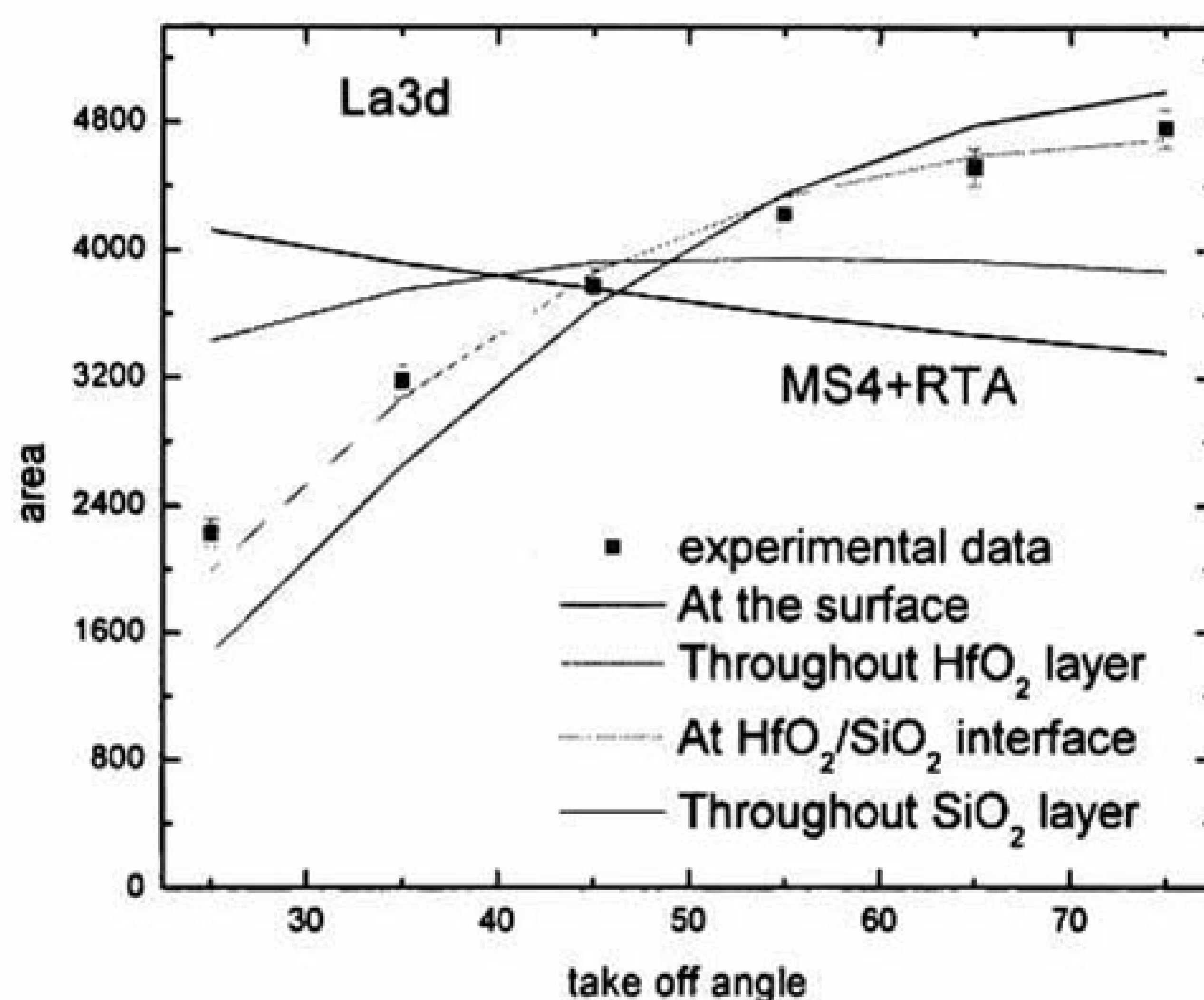

Figure 5.5 Lanthanum distribution for the RTA MS4 samples. All the lanthanum appeared located at the HfO_2/SiO_2 interface. The error from the ARXPS fits data is around 3% for each take off angle.

5.3.2 The La in the unannealed sample

The comparison between the distribution for the unannealed sample and the annealed sample is shown in Figure 5.6. There is a small but appreciable difference between both slopes suggesting that the La in the unannealed sample (black dots) had a distribution slightly shallower.

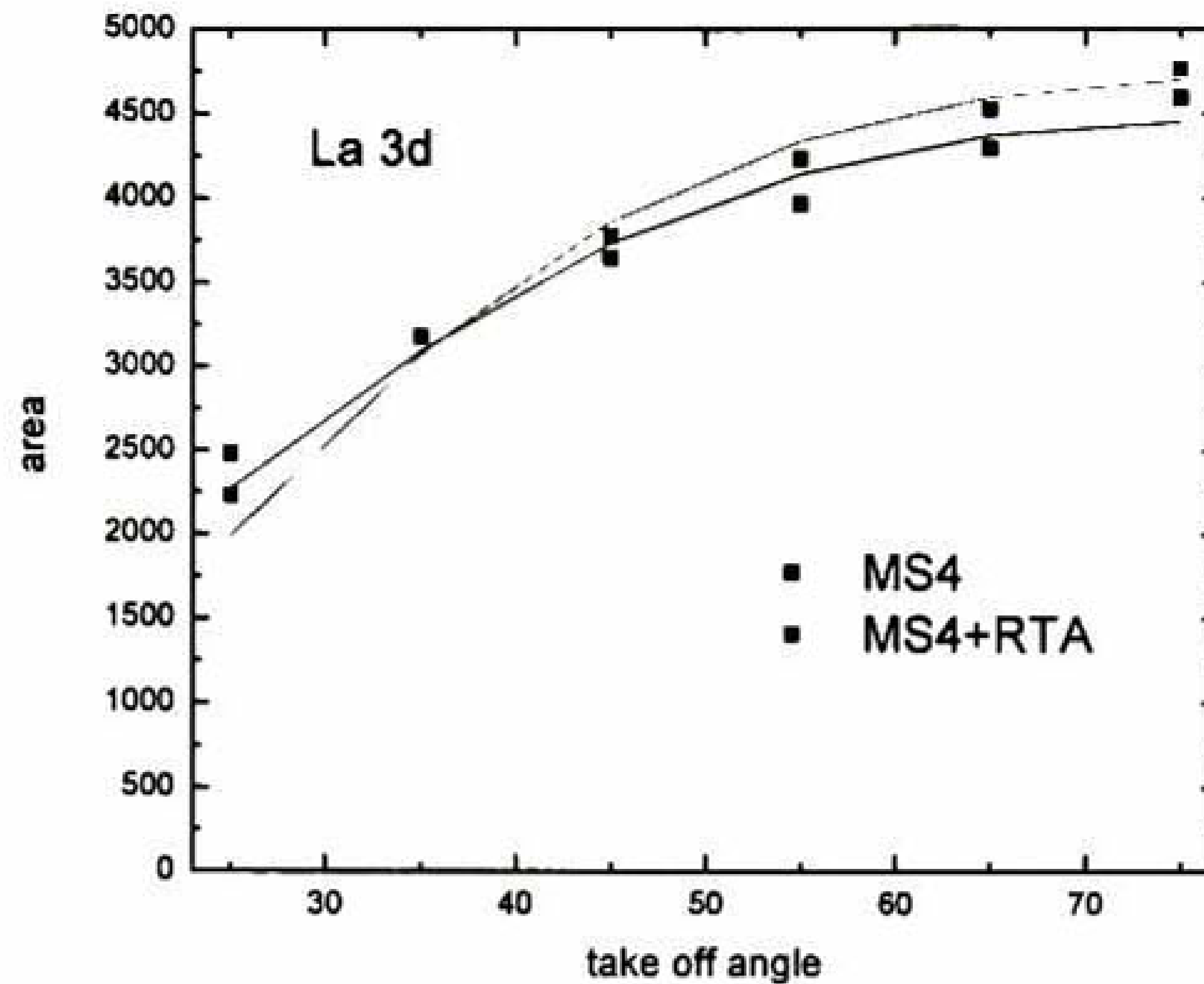

Figure 5.6 Comparison of Lanthanum distribution between the control sample and the annealed sample. There is a small difference in the slopes. Before RTA almost all the lanthanum was distributed at the HfO_2/SiO_2 interface. After annealing, the rest of La diffused to that interface.

Figure 5.7 depicts three slightly different scenarios for the La distribution in the unannealed sample. The red line is considering that all the La was at the interface. The coincidence with the experimental data could be improved by considering that a small amount (6%) of La remained on top of the HfO_2 layer (green line). However, considering that 25% of the La was distributed in the Hf layer and the rest at the interface resulted in a very similar curve (black line). The solution was not unique.

Most of the La had already diffused through the Hf layer to the HfO_2/SiO_2 interface when the samples were received. This was probably due to the thermal treatment that the samples underwent during the nitridation process at TI.

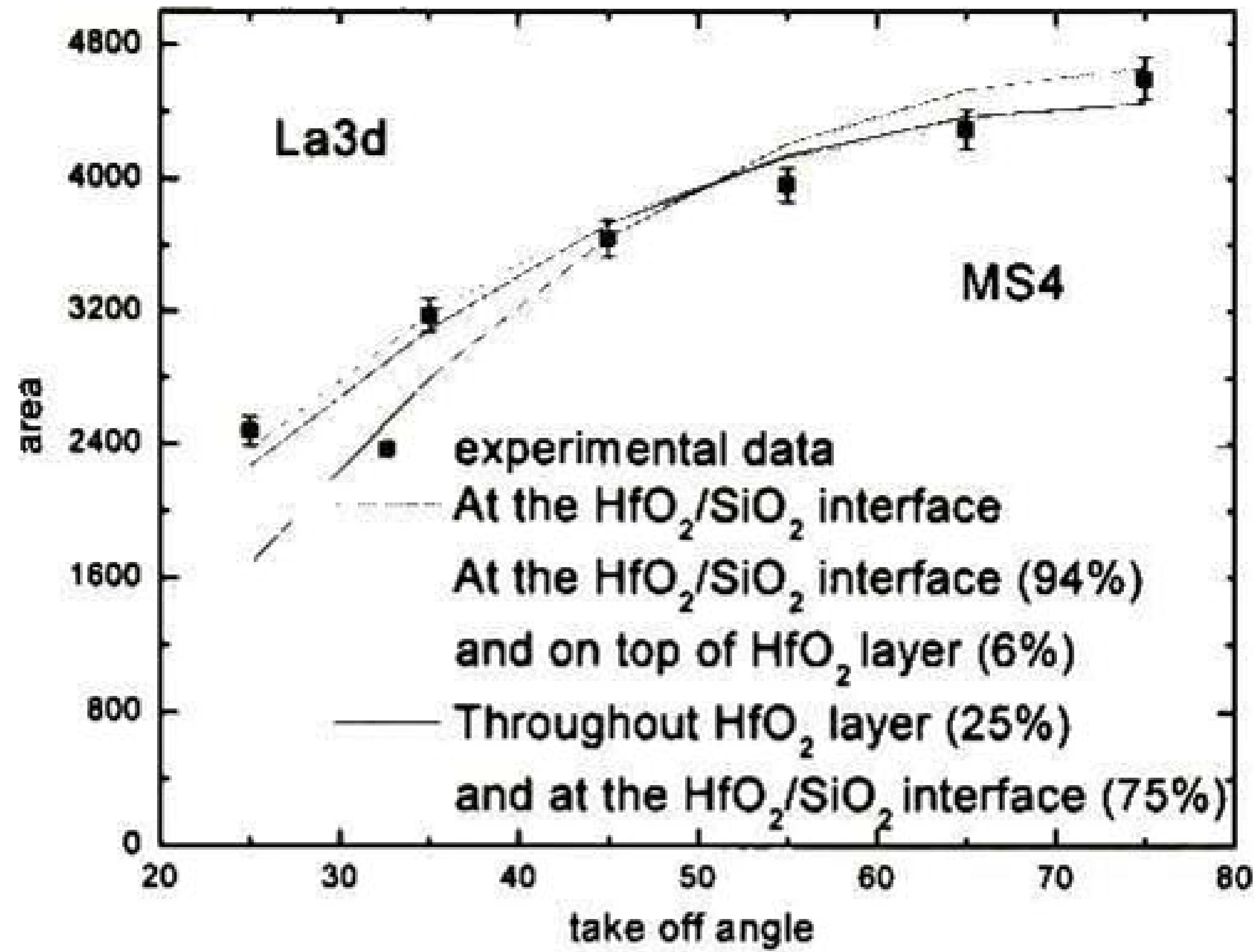

Figure 5.7 Lanthanum distribution for the MS4 as received sample. Lanthanum exhibited a deep distribution caused probably by the nitridation process. The most amount of it diffused until the HfO_2/SiO_2 interface and the rest could be located at the surface of the sample or distributed through the HfO_2 layer. The error in the ARXPS data fits was around 3% for each angle.

5.4 Calculated film structure from the quantitative ARXPS analysis

The Figure 5.8 shows the structure of the films in the MS4 sample before and after RTA. This structure is consistent with *all* the XPS data. It is also consistent with the FTIR data.

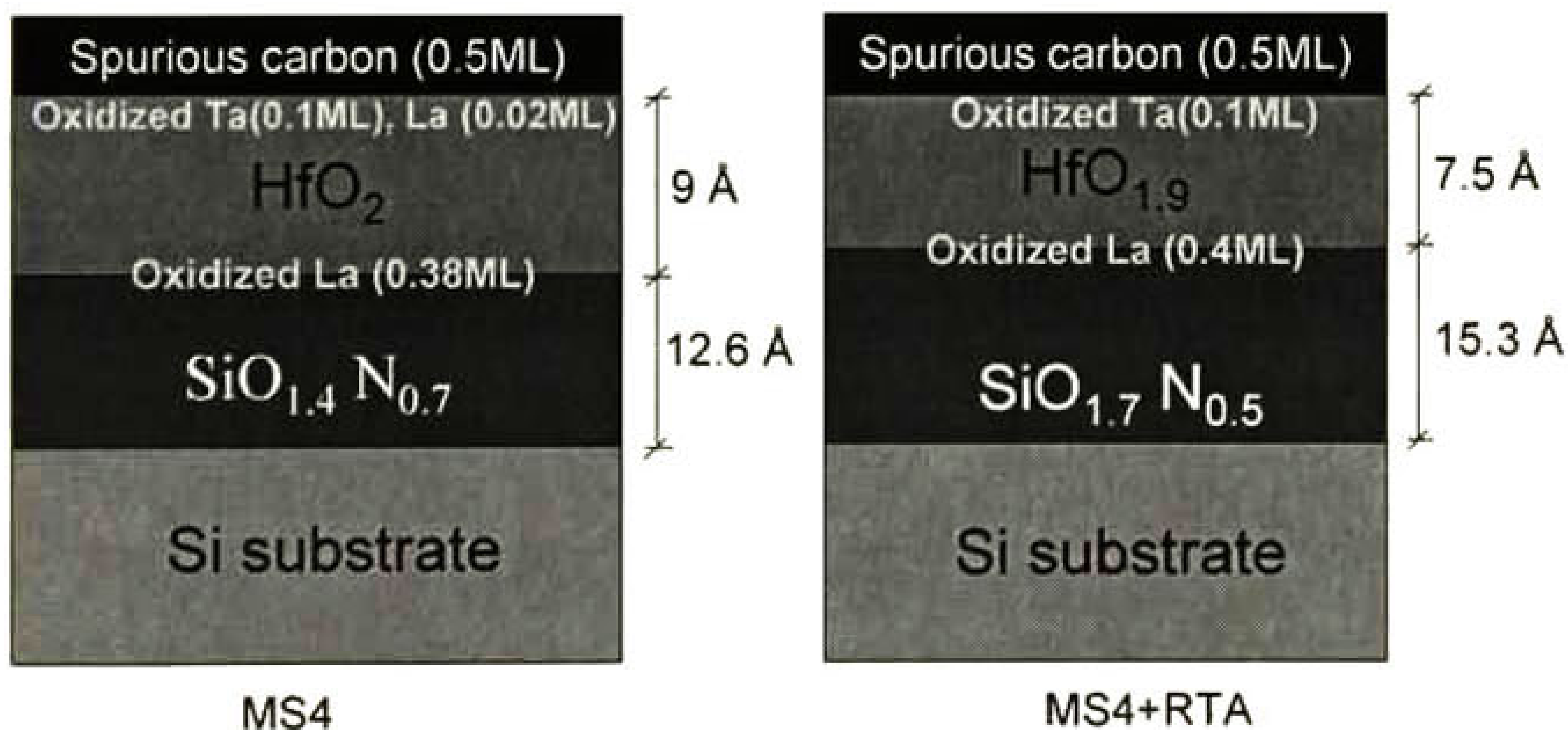

Figure 5.8 Stoichiometry and thickness of the layers in the films. It also shows the amount and distribution of the La and Ta. The growth of the SiO_2 layer, and the decrease of the HfO_2 layer, is consistent with the XPS and IR data. The stoichiometry of each layer was found from the data after correcting for the photoelectron cross section and the attenuation length effects.

The attenuation lengths of the photoelectron signal employed in the calculations were those for SiO_2 and HfO_2. The corresponding attenuation lengths for the compounds in the film (e.g., the attenuation lengths for the Si 2p, N 1s and O 1s signals in the $SiO_{1.4}N_{0.7}$ layer) were also calculated employing the NIST database.

References

1. Alberto Herrera-Gomez, "XPSGeometry: A program for depth profile analysis for ARXPS," 2006.
2. A. Thompson, et al. X-RAY DATA BOOKLET Center of X-ray Optics and Advanced Light Source. Lawrence Berkeley National Laboratory, second edition, January 2001.
3. J.J. Yeh, and I. Lindau. Atomic subshell photoionization cross sections and asymmetry parameters: $1 \leq Z \leq 103$. Atomic Data and Nuclear Data Tables, Vol. 32, pp. 1-155, (1985).
4. C.J. Powell, and A. Jablonski. Nist Electron Effective- Attenuation-Length Database, National Institute of Standards and Technology, Version 1.1, pp. 47, (2003).

Chapter 6. XPS on WSix films as metal gate

In the search for an appropriate metal gate for Hf-based high-*k* dielectrics, WSix is one of the candidates that could allow a gate self-alignment in the manufacturing process. The WSix is achieved by depositing a layer of W and a layer of Si on top of it. Then the two layers are annealed to form the WSix. The aim of this work is to study the chemical composition WSix through the film to figure it out whether there is unreacted Si or not. In this view, additional experiments was performed on WSix/HfO_2/Si samples from Texas Instruments (TI).employing Ar^+ ion sputtering XPS.

6.1 Samples

The growth processing of the samples as received from TI (diameter of the wafers was 300mm) is shown in the Figure 6.1. The sample was called 'MI20' and its structure is compounded by an amorphous silicon layer (thickness of 40nm) on top metallic tungsten layer (thickness of 10nm) on top of Hf based high-k layer(thickness of 2nm) on top of a silicon wafer as the initial grown structure. This sample was annealed to obtain WSi_x from the reaction between the W and Si layers. The residual Si that was not reacted, was stripped.

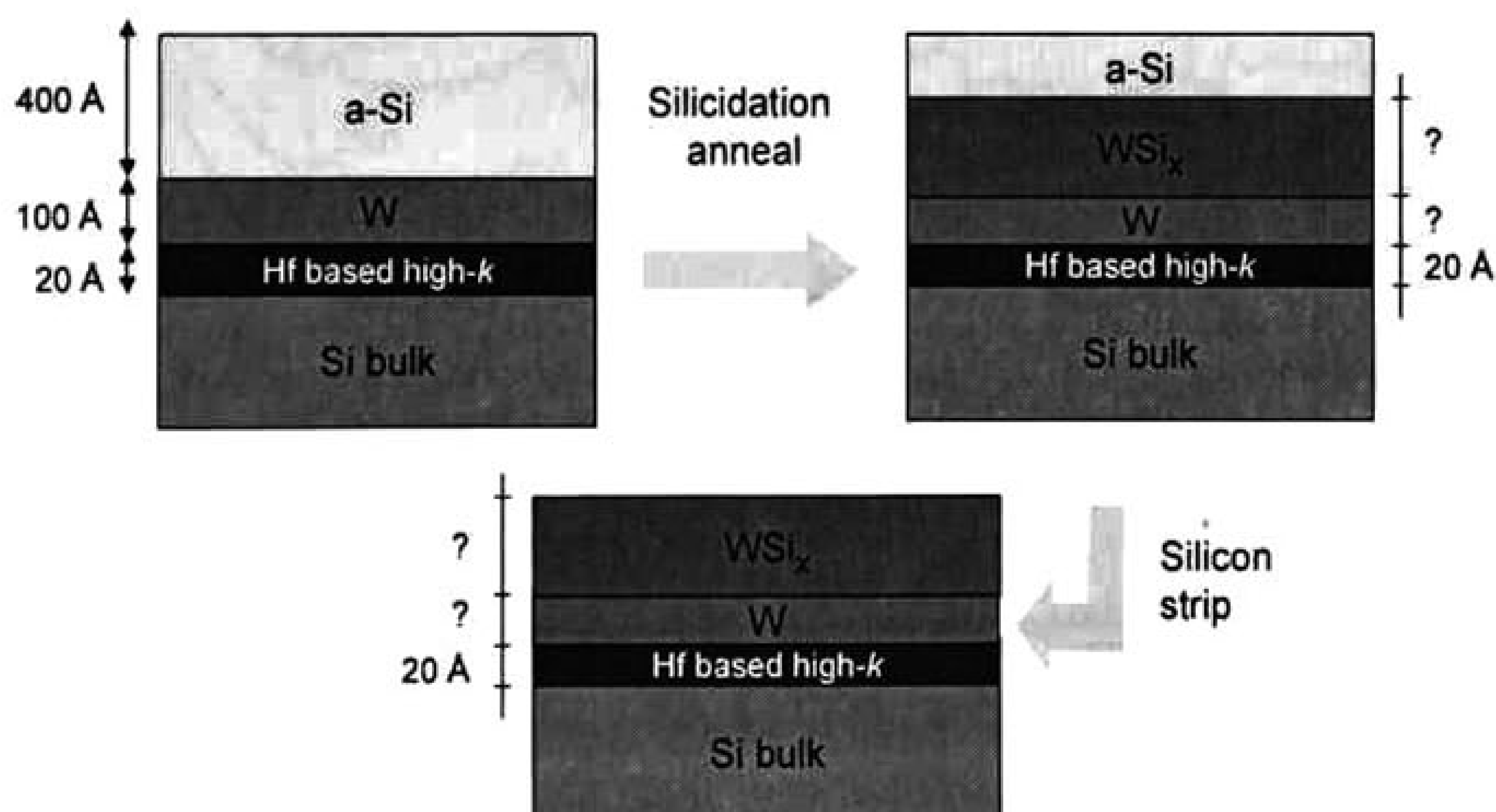

Figure 6.1 Growth processing of the samples as received from TI (MI20). The chemical reaction between Si and W atoms under annealing treatment origins a WSi_x layer.

To study the WSix, two set of samples were subject to different experiments. One group was chemically etched to remove most of the WSi_x layer and subsequently characterized by XPS. The other group was studied with XPS depth profiling using Ar^+ ion sputtering.

6.1.1 Samples chemically etched

Four MI20 samples (1.5cm x 1.5cm) were the target for chemical etching with KOH (15% vol) at 80°C for different etch times: 30 sec, 1 min, 2 min and 10 min. Immediately after the samples were introduced in the XPS chamber. The experiment for each one was done with pass energy of 50 keV (for the survey) and 15 keV (for each region). The resulting XPS spectra of the survey regions are shown in Figure 6.2 and the high resolution regions in Figure 6.3.

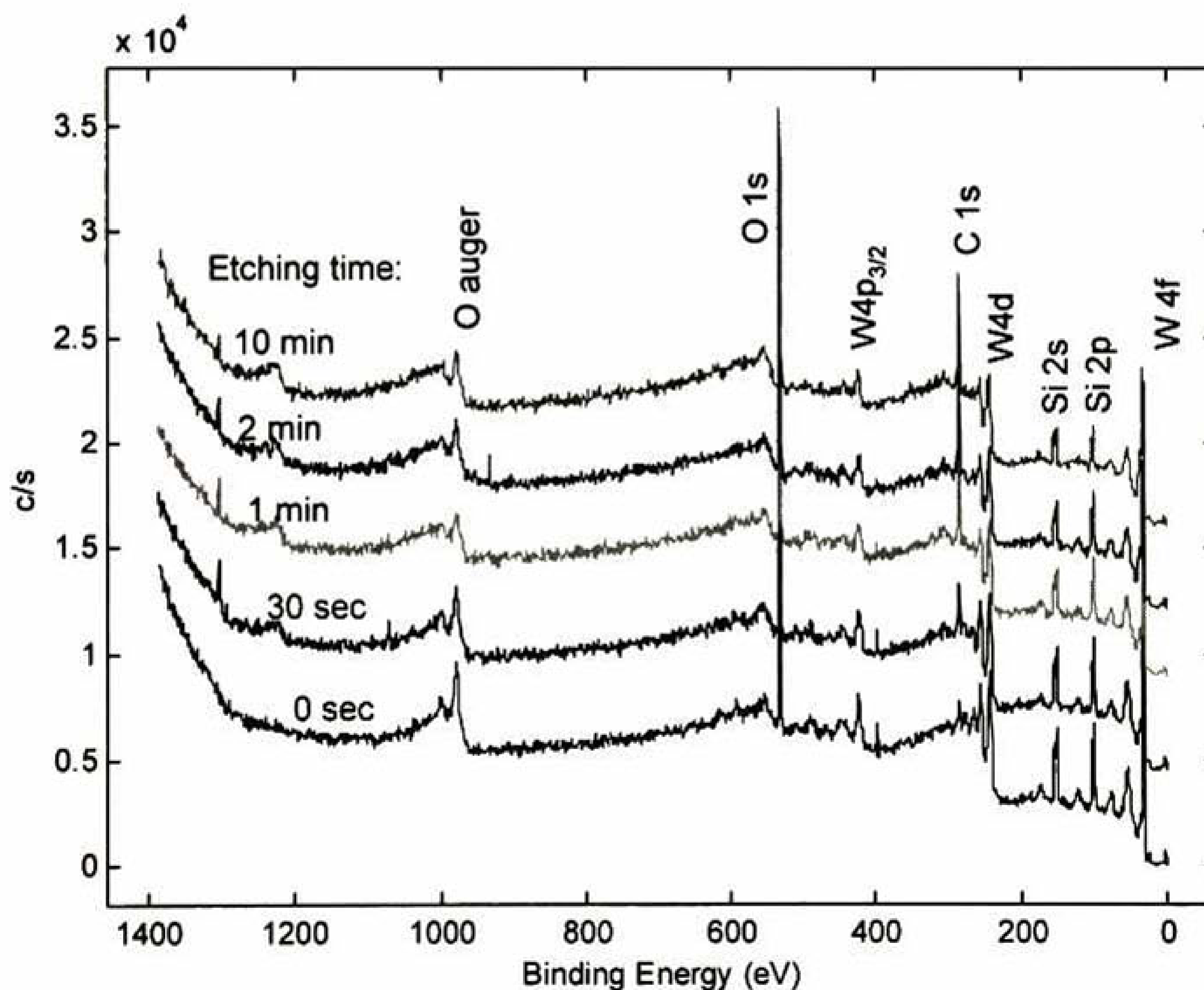

Figure 6.2 Survey (low resolution) of the detected signals from the MI20 sample at different etching times. The etching was performed with KOH at 80°C for all the samples.

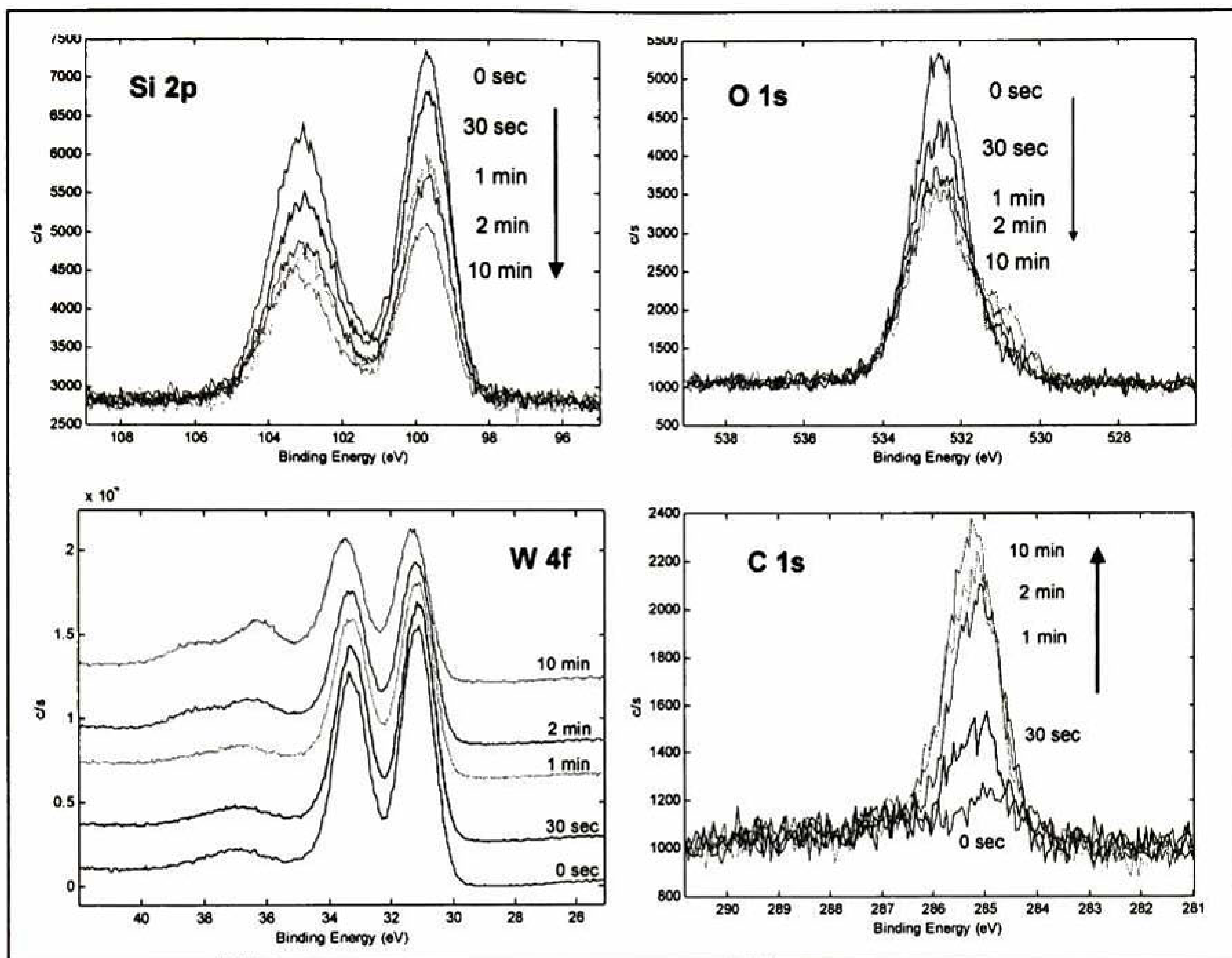

Figure 6.3 Regions taken at high resolution (pass energy = 15 eV) for the signals of interest detected from the MI20 sample for different etching times.

The XPS signals from W, Si and O decreased with the etching time while the C signal increased. This might be due to C contamination from the etching solution. Although 10min should have been enough to remove the WSi_x layer, no signal from Hf was detected. A possible explanation for these observations is that the etching rate of WSix in KOH was very small (up to 10 min). As it will be demonstrated in the next section the oxygen amounts found here is due to the oxidation from the KOH etching solution. It was not possible to find any useful information about the amount of tungsten silicide formation through the film.

6.1.2 Ar^+ sputtering depth profiling with XPS

A sample without etching was selected for Ar^+ sputtering depth profiling. The conditions for Ar^+ sputtering were: energy= 5 keV, current = 25 mA; sputtering area = 4 mm ×

4 mm, sputtering rate ≈ 3Å/min; sputtering times = 0sec to 16 min. Figure 6.4shows the spectra for W4f, Si 2p, Hf 4f and O 1s regions for several sputtering times.

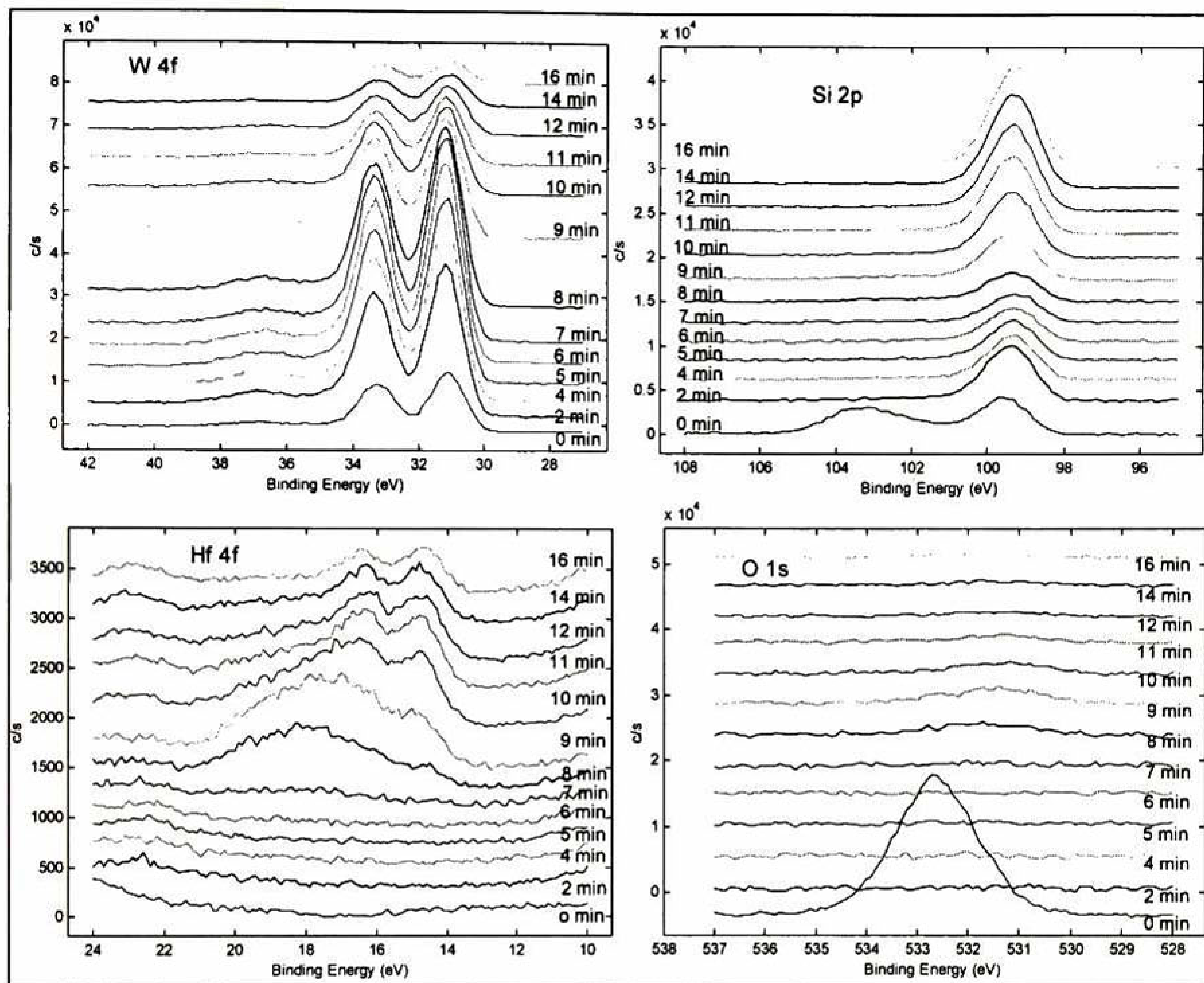

Figure 6.4 XPS regions of interest for the MI20 sample at different Ar^+ ion sputtering times. The sputtering area was of 4 × 4mm^2, the sputtering ratio≈ 3Å/min; the beam energy of 5keV with a current of 25 mA; and the range time sputtering from 0sec to 16 min.

From the Wf 4f region shown in Figure 6.4, W remains in a small amount in the sample after 16 minutes of sputtering. In the other hand, is expected that Ar^+ ion sputtering is more selective removing Si than W atoms. At the beginning, the presence of Si 2p is due to WSix. Si decreases continuously until approximately the first 8 minutes of sputtering. It is suggested that Si 2p from WSix is gone after 8 minutes of sputtering and after that the Si detected signal comes from the Si bulk (this signal start increasing). The presence of Hf 4f appears after 7 minutes and increases after that showing a binding energy shift (Hf 4f in HfO_2). At 9 minutes, the signal of Hf 4f is highest and after that, it

decreases. Oxygen is almost gone after the first time sputtering. Between 7 and 10 minutes, there is a small amount of it; however, at 16 minutes, there is not evidence of oxygen or it is below the XPS detection limit. The Figure 6.5 shows the intensity profile for O 1s, W 4f, Si 2p and Hf 4f. The plot indicates that the intensities of O 1s, Si 2p and Hf 4f were multiplied by a factor.

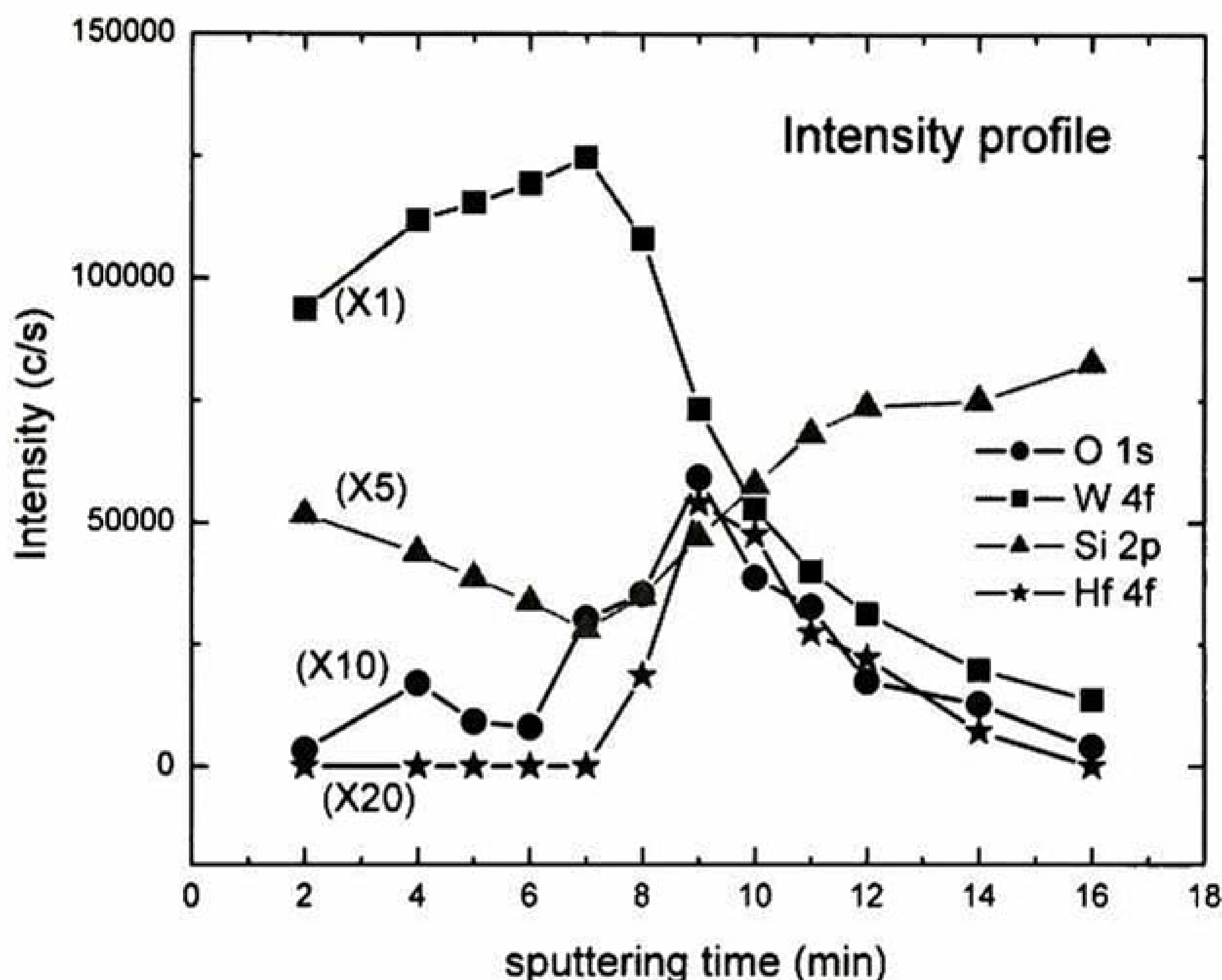

Figure 6.5 Ar^+ sputtering depth profile showing the most important species detected in the MI20 sample at different Ar^+ ion sputtering XPS times.

In addition to the difference on Ar^+ sputtering rate for different atoms, there are other side effects when using this technique as the breaking of bonds and knock-on effects. The breaking of bonds during the Ar^+ sputtering process make difficult to extract chemical information with XPS. Then the only useful information will be about the total atomic concentrations. On the other hand, the preferential sputtering rate and the knock-on effect will distort the atomic compositional depth profile. As a conclusion, Ar^+ sputtering XPS depth profile is not the best convenient technique for depth profiling in this particular work due to:

The relative size ratio of the beam bombarding (Ar ions) with the target species, that is, W and Hf are big and so, heavy atoms, while Si and O are very small and light. As a

consequence Ar^+ sputtering is more selective removing Si than W species in WSix and so, the sputtering ratio is not the same for both.

It was demonstrated Ar^+ ion sputtering is a destructive technique; metallic hafnium is the consecuence of bond breaking in hafnium oxide·(attributed to the difference binding energy observed in Hf 4f region of Figure 6.4).

Chapter 7. Conclusions

We have studied the effect of RTA annealing on $La_2O_3/HfO_2/SiO_2/Si(001)$ stacks in terms of the stoichiometry and layer structure using ARXPS and FTIR. In addition we studied the compositional depth profiling in thick WSix films using Ar^+ sputtering XPS. A summary of the conclusions in this work is show below.

- The surface morphology of the samples with protrusions was rougher even between the protrusions. The ARXPS for the samples showed some problems and the data obtained at grazing angles had to be discarded.
- Annealing in vacuum had the effect of lowering the signal from carbon and disappearing a component of oxygen associated to hydroxides.
- The data obtained with a pass energy of 15eV had enough resolution to allow for a proper de-convolution and to discriminate chemical species close to each other. Even though the La 4d peak was very close to the Si 2p peak, it was possible to deconvolute the contribution from each specie.
- The La 3d photoelectron peak revealed a rich structure consisting of one oxidation state ad several satellite peaks..
- The O 1s photoelectron peak showed two chemical states that were identified as Hf-O-Hf and Si-O-Si bonds.
- The O 1s and Si 2p in silicon oxide peak increased together after RTA. This could be attributed to residual oxygen inside the RTA chamber.
- Only one chemical state for Hf 4f was found in the XPS data. This chemical component is attributed to Hafnium oxide. No HfSiO2 was formed,
- There no was evidence of presence of nitrogen in the HfO_2 layer before and after RTA. This might be the result of an annealing treatment after nitridation that has been previously shown that N migrates from the HfO_2 to the SiO2 layer (see A. Herrera-Gomez, *et al.*, to be submitted to Appl. Phys. Lett. (2007).

- The Tantalum was not removed completely by the chemical etching. A very small amount remained at the surface of the sample. No diffusion of Ta towards the interface was detected.
- The overall behavior of the area for all the peaks was similar before and after RTA, suggesting that the structure was stable. The changes in stoichiometry and thicknesses of the layer were small but measurable as it wass demonstrated in Chapter 5.
- As expected, the bulk Si 2p peak showed a larger slope than the Si 2p from silicon oxide. The physical model proposed for the angular dependence of the peak area consisted on a layer of hafnium oxide on top of a layer of silicon oxide on top of the Si(001)substrate,.
- The theoretical prediction of the angular dependence implied an independent knowledge of the geometrical parameters of the XPS tool and other parameters such as the photoelectron cross section and effective attenuation length of each layer. These parameters were obtained from the literature and from tables provided by NIST.
- The angular dependence of the cations (Si and Hf) constituting the film was employed to determine the thicknesses of the layers. The carbon had also to be considered since it constituted a layer at the surface. The thickness was forced to reproduce the density of the bulk silicon oxide and hafnium oxide. The constraints on the density were preferred for the improvement of the fit.
- The angular dependence behavior of oxygen attributed to SiO_2 showed a larger slope than that in HfO_2. The slope lines corresponding to nitrogen peak suggested that it was distributed deep in the film. The angular dependence of the peak area of anions was closely reproduced forcing the spatial distribution of each oxygen and nitrogen species to the corresponding layer. The consistency of the compound was preferred over the quality of the fit. However, the experimental data was nicely reproduced.

- The stoichiometry of each layer was not forced but found, and resulted in values very close to those expected.
- The large slope for the La 3d peak area indicated that it was distributed deep in the film and not at the surface, as it was originally grown. In contrast, the flat behavior for Ta 4f suggested that it remained at the surface. The quantitative analysis confirmed that those were the case. Only one of the scenarios of the angular dependence considered for La in the treated sample was consistent with the data. The conclusion is that the La is completely located at the SiO_2/HfO_2 interface before the RTA anneal.
- The comparison between the distribution for the unannealed and the annealed sample is a small but appreciable difference in both slopes suggesting that the La in the unannealed sample had a distribution slightly shallower.
- The La diffused through the Hf layer due probably to previous thermal treatments. Although the RTA induced further diffusion, most of the La had already migrated to the HfO_2/SiO_2 interface.
- For the unannealed sample, two solutions of the distribution of La were considered, both reproducing the experimental data closely. The first scenario considered that a small amount (6%) of La remained on top of the HfO_2 layer and the rest (94%) at the SiO_2/HfO_2 interface. The second scenario considered that 25% of the La was distributed in the Hf layer and the rest at the SiO_2/HfO_2 interface.
- The LO phonon mode FTIR feature for O-Si-O bonds appeared at 1220 cm-1 while in the literature it is reported at 1240 cm^{-1} for thicker films.
- The MS4 sample showed a larger O-Si-O and lower O-Hf-O FTIR signals after RTA, which was consistent with the ARXPS analysis.
- In the set of WSix films studied we found a poor depth resolution in the depth range of nanometers. This is due to a collection of effects where some of them can not be avoided.

- The most marked difficulty is the preferential sputtering rate of Si respect to W in addition to knock-on effects. These two phenomena distort the real depth profile of some elements respect to the others.
- One more disadvantage f this technique in depth profiling of nanometer thick films is the fact that the probing depth of XPS is few nanometers. This causes a broadening of the real depth profile.
- These two complications provoke a poor elemental depth profile which makes difficult to extract reliable information and have to be taken into account whenever this technique is employed.

Future Work

- The TaN/La_2O_3/Hf samples arrived at UTD already with thermal treatments. As shown in this thesis, most of the La was already at the HfO_2/SiO_2 interface. It would be of interest to cause the diffusion of La through the Hf layer in a controlled way, and to determine the activation energy of this transport.
- In addition, it would be interesting to study the effect of further annealing (more RTA time), and to find out whether the La could diffuse further into the stack.
- The correlation of the La position with the electrical properties of the MOS devices would be of great interest. As proven in this thesis, the position of the La and the structure of the whole stack could be determined with great accuracy. Since the structure could be characterized in detail, it would be possible to model the electronic transport in a more precise way, and to pinpoint the effect of the structure on the electrical performance.
- It is also of interest to reproduce the based high-k/Si gate stack processing to gain control over the details of the parameters of the preparation of the samples.

EL JURADO DESIGNADO POR LA UNIDAD QUERÉTARO DEL CENTRO DE INVESTIGACIÓN Y DE ESTUDIOS AVANZADOS DEL INSTITUTO POLITÉCNICO NACIONAL, APROBÓ LA TESIS DE MAESTRÍA LA C. MARIA ISABEL MEDINA MONTES TITULADA: “LA ESTABILIDAD TÉRMICA DE INTERFACES DE ALTA CONSTANTE DIELECTRICA PARA CIRCUITOS CMOS AVANZADOS” FIRMAN AL CALCE DE COMÚN ACUERDO LOS INTEGRANTES DE DICHO JURADO, EN LA CIUDAD DE QUERÉTARO, QRO., A VEINTISIETE DE NOVIEMBRE DEL DOS MIL SIETE.

DR. ALBERTO HERRERA GÓMEZ

DR. FRANCISCO SERVANDO AGUIRRE TOSTADO

DR. ROBERT M. WALLACE

DR. JOSÉ MARTÍN YÁÑEZ LIMÓN

DR. FRANCISCO JAVIER ESPINOZA BELTRÁN

CINVESTAV
BIBLIOTECA CENTRAL

SSIT000006242